POLITECNICO
MILANO 1863

SCUOLA DI INGEGNERIA INDUSTRIALE
E DELL'INFORMAZIONE

Study of low-energy excitations in the pyrochlore iridate $Tb_{2+x}Ir_{2-x}O_{7-y}$ ($x \sim 0.4$) probed by Resonant Inelastic X-Ray Scattering

Tesi di Laurea Magistrale in
Engineering Physics - Ingegneria Fisica

Author: **Anna Toschi**

Student ID: 943362
Advisor: Prof. Marco Moretti
Co-advisors: Dr. Christoph Sahle, Dr. Quentin Faure
Academic Year: 2020-2021

Abstract

A single crystal of $Tb_2Ir_2O_7$ is studied using the RIXS technique on ID20 at the European Synchrotron Radiation Facility (ESRF).
This crystal is a pyrochlore iridate of the family of iridium oxides. These oxides are characterized by strong spin-orbit coupling whose interplay with electronic correlations allows to explore exotic phases of matter. They have been predicted to display the so-called *Weyl semimetal* phase (WSM). The realization of this phase in pyrochlore iridates has two requirements: the time reversal symmetry breaking due to the so-called *All-In-All-Out* (AIAO) magnetic configuration and medium-low electronic correlations avoiding an insulating behaviour. While the AIAO structure has been found in many pyrochlore iridates, the strength of electronic correlations is still under debate.
A finite degree of *stuffing* is found in our sample: excess of the rare-earth ions which substitute iridium ions. The stoichiometry found in our $Tb_{2+x}Ir_{2-x}O_{7-y}$ sample is $x \sim 0.4$. The crystal becomes more metallic and the magnetic transition, attributed to the AIAO structure arising on the iridium sublattice, is observed at lower temperature.
The RIXS technique is employed to study the low-energy excitations of the system. The *dd* excitations allow to study the electronic structure of the crystal. The crystal is trigonally distorted as also found for other pyrochlore iridate single crystals. The trigonal crystal field and the SOC constant are estimated from an empirical model. The values found are: $\Delta = 0.516$ eV and $\lambda = 0.399$ eV.
At lower energies a complex profile appears in the spectrum. The elastic peak, a magnetic excitation and a broad feature, the nature of which is still unclear, are identified. The dispersion relation of the magnetic excitation along the high-symmetry crystallographic directions is obtained from the fit of the spectra. The magnetic excitations have been simulated using a linear spin wave model as implemented in the SpinW code. The simulated Hamiltonian contains terms describing the Heisenberg interaction proportional to J and the Dzyaloshinskii-Moriya interaction proportional to D. From the fit of the experimental data the magnetic interactions are estimated: $J = 18.09$ meV and $D = 6.6$ meV. The comparison of the experimental data with numerical simulations on SpinW shows some discrepancies. Thus, a more itinerant approach could be necessary to describe the physics

of the system as also implied from the resistivity value and from the comparison with RPA calculations. The realization of the Weyl semimetallic phase is compatible with the results obtained and further studies should be addressed.

Keywords: iridates, Weyl semimetal, pyrochlores, RIXS, synchrotron

Abstract in lingua italiana

Un singolo cristallo di $Tb_2Ir_2O_7$ è studiato tramite la tecnica RIXS a ID20 di ESRF (European Synchrotron Radiation Facility) a Grenoble (Francia).
Si tratta di un pirocloro iridato nella famiglia degli ossidi di iridio. Questi composti sono caratterizzati da un forte effetto di spin orbita che insieme alle correlazioni elettroniche permette di osservare fasi della materia inesplorate. Nel caso di questi materiali una fase attesa è la cosiddetta *Weyl semimetal phase* (WSM). Due requisiti necessari per la realizzazione di tale fase sono la rottura della simmetria per inversione temperale dovuta alla configurazione magnetica cosidetta *All-In-All-Out* (AIAO) e correlazioni elettroniche nel medio-basso regime, altrimenti un comportamento isolante sorgerebbe.
Il campione studiato presenta un finito grado di *stuffing*: ioni di terbio sostituiscono quelli di iridio e la reale stochiometria diventa $Tb_{2+x}Ir_{2-x}O_{7-y}$ con $x \sim 0.4$. La conseguenza di ciò è un comportanto più metallico del campione, come evidenziato da misure di resisitività. Inoltre, misure magnetiche evidenziano una transizione magnetica, che è stata attribuita all'insorgere della configurazione AIAO nel sub-cristallo di iridio, a temperature più basse rispetto a campioni stochiometrici.
Le eccitazioni a bassa energia sono state studiate tramite la tecnica RIXS. In particolare, le eccitazioni *dd* permettono di ottenere informazioni circa la struttura elettronica. Il cristallo è distorto trigonalmente, come è stato osservato per altri cristalli singoli di piroclori iridati. Un modello empirico dalla letteratura permette di stimare il campo cristallino trigonale e la costante di spin-orbita. I valori trovati sono: $\Delta = 0.516$ eV e $\lambda = 0.399$ eV.
A energie più basse il profilo di intensità nello spettro appare complesso. Esso contiene il picco elastico, un'eccitazione magnetica e un picco molto largo la cui origine fisica non è ancora chiara. La relazione di dispersione del magnone è stata ricostruita con i fit dei dati. Le eccitazioni magnetiche sono state simulate con un modello lineare di onde di spin come implementato nella libreria SpinW. L'Hamiltoniana simulata comprende un termine d'interazione di Heisenberg proporzionale a J e un termine che rappresenta l'interazione Dzyaloshinskii-Moriya proporzionale a D. Dal fit dei dati sperimentali le interazioni magnetiche sono state quantificate: J =18.09 meV e D = 6.6 meV. Il confronto tra i dati

sperimentali e le simulazioni con SpinW mostrano delle discrepanze. Di conseguenza, un modello più itinerante potrebbe essere più adatto a descrivere la fisica del sistema, come anche suggerito dal valore della resistività e dal confronto con calcoli RPA. La realizzazione della fase Weyl semimetallica è compatibile con i risultati ottenuti ma studi ulteriori sono necessari.

Parole chiave: iridati, Weyl semimetalli, piroclori, RIXS, sincrotrone

Contents

Introduction

Transition metal oxides (TMOs) show some of the most fascinating phenomena of condensed matter physics. For many years, research has focused on $3d$ TMOs since they were discovered to display intriguing phases such as high-temperature superconductivity, as in the case of cuprates [1]; metal-insulator transitions [2], giant magnetoresistance [3] or multiferroicity [4]. These phases are of extreme interest both for the understanding of fundametal physics and for potential applications. Such interesting behaviours have foundations in the strong correlations between the electrons, in other words the Coulomb repulsion.

Electronic correlations decrease when moving to heavier transition metal atoms due to the larger extension of the wavefunctions. For $5d$ TMOs electronic correlations become comparable to other energy scales. In particular, an interaction that is of fundamental relevance in those systems is the spin-orbit coupling (SOC), which instead for lighter atoms can be neglected. The consequence of the presence of SOC, together with the competition with the other energy scales, is the display of exotic topological phases of matter yet poorly understood such as the Weyl semi-metal phase. In addition to fundamental interest, the latter is extremely appealing for possible technological applications due to exceptional optoelectronic properties [5–7].

Within the family of $5d$ TMOs, a class of materials that are of great interest from this point of view are iridium oxides, also called *iridates*.

The present work is focused on the study of these compounds, in particular pyrochlore iridates with chemical formula $R_2Ir_2O_7$ (R = lanthanides). We have especially focused on $Tb_2Ir_2O_7$. First, we have characterized this compound by Electron Dispersive X-rays spectroscopy (EDX) and magnetometry measurements. Later on, we investigated the low-energy dynamics of the sample using Resonant Inelastic X-rays Scattering (RIXS). Those experiments have been carried out at the Néel Institute and beamline ID20 at the European Synchrotron Radiation Facility (ESRF), Grenoble (France).

In Chapter 1 the Hubbard model is discussed. The spin orbit coupling is introduced and the electronic correlations versus spin-orbit coupling phase diagram obtained from the extended Hubbard Hamiltonian is reported. The physics of iridium oxides is introduced with particular focus on SOC onto the electronic and magnetic properties of $5d$ TMOs. Finally, the latest research results on pyrochlore iridates is reported.
In Chapter 2 the experimental and numerical methods used in this thesis are described. Firstly, I briefly introduce the concept of synchrotron radiation. The RIXS technique and the setup of ID20 are then described. The macroscopic measurements used to characterize the sample are also shortly discussed. Finally, the chapter closes with an introduction of the SpinW library used to perform numerical simulations to model the dispersion of the magnetic excitations observed by RIXS.
Chapter 3 is dedicated to the experimental study of a single crystal of $Tb_2Ir_2O_7$. A numerical analysis using a spin wave model has also been carried out and is presented here. Finally, a discussion of the results obtained is reported, comparing them with what was found in previous studies.

1 | New phases in strong spin-orbit coupling systems

The electronic and magnetic properties of transition metal oxides (TMOs) are determined by the competition of different energy scales, such as the electronic correlations U, the electronic bandwidth W or the spin-orbit coupling (SOC) λ.
Fig. 1.1 shows the radial distribution of the d orbitals for different quantum numbers n = 3, 4, 5. They become more extended upon descending from $3d$ to $5d$ transition metals. As a consequence, the probability for an electron to hop from one site to the other increases and therefore the bandwidth W increases. Concomitantly, the electronic repulsion U decreases with the extension of the d-orbitals. The SOC constant is a function of the atomic number Z and thus increases going down in the periodic table.

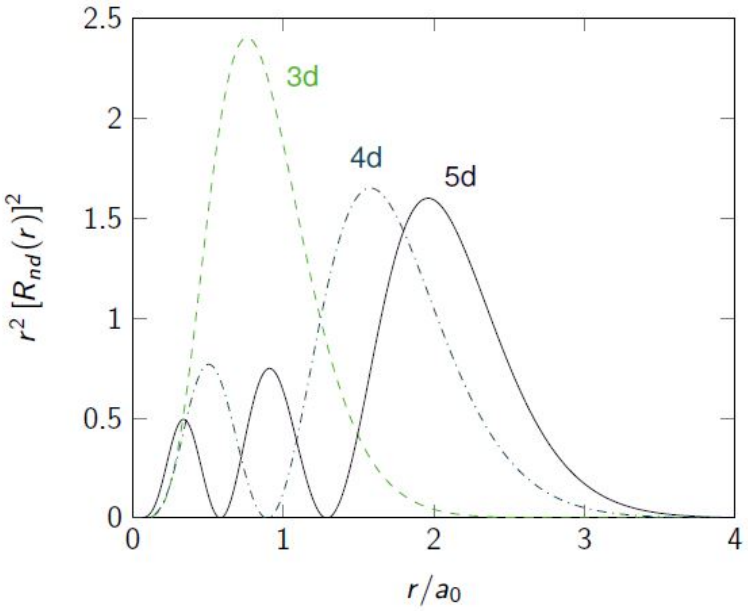

Figure 1.1: *Radial distribution of nd orbitals: they become more extended going from 3d to 5d orbitals. From [8].*

Fig. 1.2 shows the periodic table of elements with the trends of the Coulomb repulsion U,

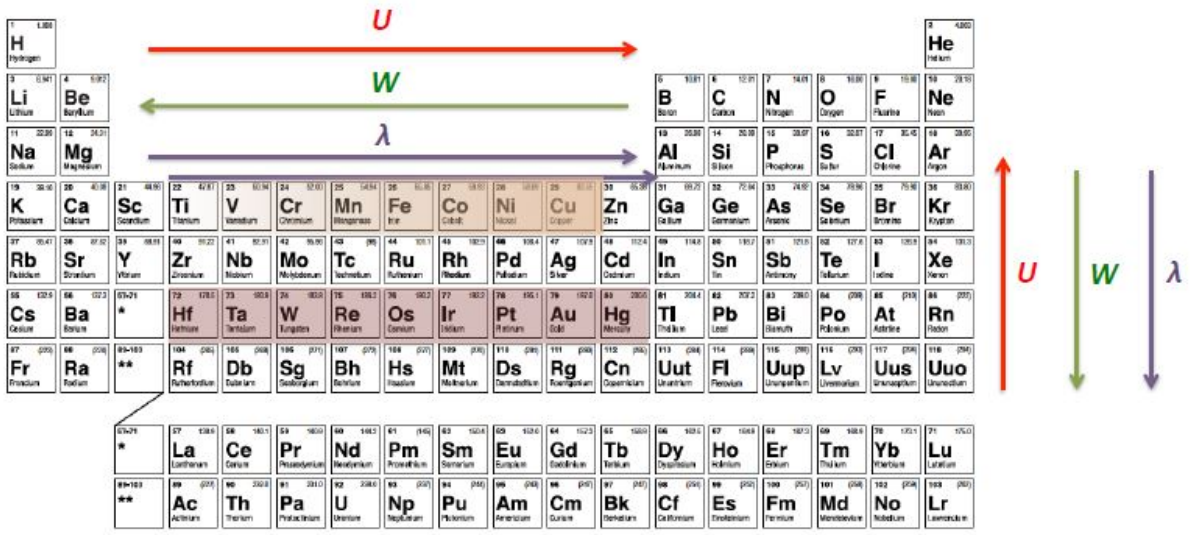

Figure 1.2: *Periodic table of elements. The colored boxes are 3d and 5d transition metals. The trend of the Coulomb repulsion (U), bandwidth (W) and spin orbit effect (λ) are shown. The Coulomb repulsion increases moving towards the right and to the top of the periodic table. The bandwidth has opposite behaviour. The SOC constant is a function of the atomic number (Z): it increases moving towards the right and towards the bottom of the periodic table.*

the electronic bandwidth W and the SOC constant λ, displayed by colored arrows.

In this chapter I will introduce the Hubbard model for the description of correlated electron systems. The spin-orbit coupling is then described and included in the Hamiltonian. The U vs λ phase diagram based on this extended Hamiltonian is shown. New phases of matter, in particular topological ones appears in the strong-spin orbit coupling regime. Iridium oxides, that are the main materials studied within this thesis, are found at the centre of this phase diagram. Therefore their electronic and magnetic properties will be introduced. Within the family of iridates, particular interest is on pyrochlore iridates which have been predicted to display the so-called *Weyl semimetal* phase. Their properties are discussed and the latest research results on these compounds are presented.

1.1. Generalities about strong spin-orbit coupling systems

1.1.1. Hubbard model

The description of the physics of correlated-electron systems is typically carried out in the Hubbard model framework, that is a paradigm in condensed matter. The Hubbard Hamiltonian is:

$$H = -t \sum_{<i,j>} \sum_{\sigma} (c^{\dagger}_{i\sigma} c_{j\sigma} + c_{i\sigma} c^{\dagger}_{j\sigma}) + U \sum_{i} n_{i\uparrow} n_{i\downarrow} \tag{1.1}$$

where t is the hopping integral, $c^{\dagger}_{i\sigma}$ and $c_{i\sigma}$ are the creation and annihilataion operators for electrons with spin σ on site i, U is the Coulomb repulsion, $n_{i\sigma}$ is the electron density with spin σ on site i. The Hamiltonian is composed of two terms. The first one is a tight-binding term. It contains the hopping integral t which takes into account the hopping of electrons from one site to another in the lattice. This hopping leads to the formation of a *doublon* (a site that is occupied by two electrons) and a hole with the consequent development of an energy band whose width W is proportional to t and which represents an energy saving in terms of kinetic energy. The second is instead representative of the on-site repulsion (electronic correlation): U is the energy cost of having two electrons on the same site due to Coulomb repulsion. The first term favours the delocalization of electrons, while the second one pushes towards their localization. Therefore, there is a competition between the two terms that results in a specific behaviour of the material.
Considering a system with one electron per each atom, resulting in a half-filled band at the Fermi level, its behaviour can be derived comparing two energy scales according to the Hubbard model: U and W ($\propto$ t). When $W \gg U$ the system is metallic since the Fermi level crosses the energy band as represented in Fig. 1.3a. When $U \gg W$ a gap opens and the system is in a so-called *Mott-insulating* state as shown in Fig. 1.3b. For $U \sim W$, there is a transition between a metallic and a Mott-insulating state.
This description can be applied to transition metal oxides (TMOs). In particular, the insulating behaviour is well explained for $3d$ TMOs since they are characterized by narrow bands and large values of the on-site Coulomb repulsion, i.e $U/W \gg 1$.
In this strong Coulomb repulsion regime, electrons are localized on their atomic sites and the Hubbard Hamiltonian can be reduced to the Heisenberg Hamiltonian:

$$H = \sum_{i,j} J_{i,j} \mathbf{S}_i \cdot \mathbf{S}_j \tag{1.2}$$

where $J_{i,j}$ is the exchange constant between spins on sites i and j. Generally, only the interaction between nearest neighbouring magnetic moments is considered, and the relative exchange constant will be referred to as J, which corresponds to $J = 4t^2/U$. In the convention used here, if J is positive the magnetic moments will align in an antiferromag-

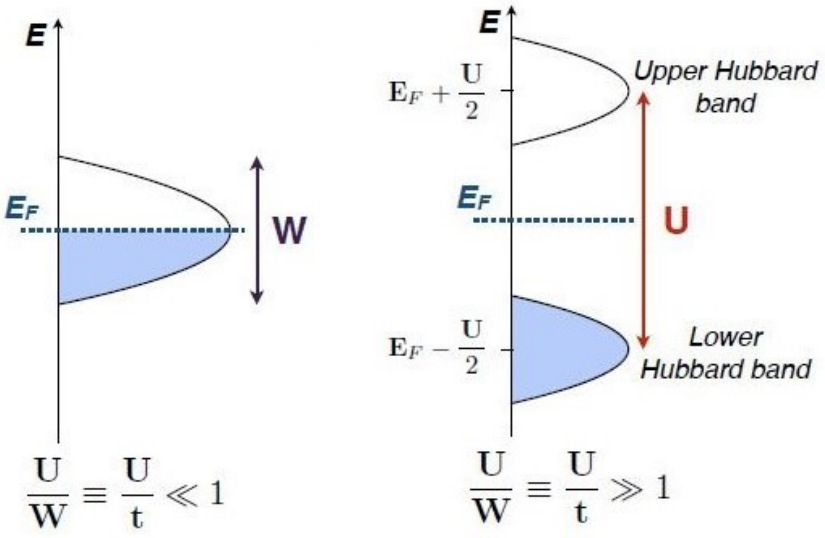

(a) (b)

Figure 1.3: *(a) Half filled band in the case of low correlations: the material has a metallic behaviour. (b) The strong correlation U splits the half filled band into a upper Hubbard band and a lower Hubbard band separated by an energy α U. From [9].*

netic configuration, while if it is negative in a ferromagnetic one.
The Heisenberg model is able to describe the low-energy physics of many systems in which electrons are strongly correlated, such as cuprates. On the contrary, $4d$ and $5d$ oxides are charaterized by a lower Coulomb repulsion and according to the Hubbard model they are expected to have a metallic behaviour. However, metal-insulating transitions (MIT) have been observed in many $5d$ compounds at low temperature [10]. The explanation of such unexpected behaviour resides in the spin-orbit coupling that has not been taken into account in eq.1.1.

1.1.2. Spin-orbit coupling

The spin-orbit effect is a relativistic interaction between the spin of an electron and its motion, in other words its orbital angular momentum.
In the reference frame of an electron, the nucleus with charge Ze rotates around it and therefore generates a magnetic field (see Fig. 1.8):

$$\mathbf{B} = -\frac{\mathbf{v} \times \mathbf{E}}{c^2} \tag{1.3}$$

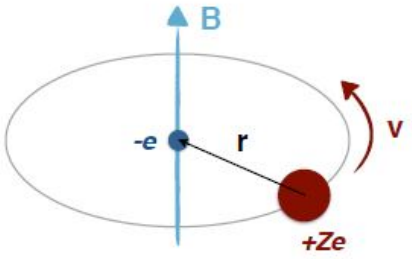

Figure 1.4: *Schematic representation of the motion of a nucleus of charge +Ze orbiting around an electron in the electron reference frame. It generates a magnetic field* $\boldsymbol{B}$*. From [9].*

where $\mathbf{v}$ is the velocity of the nucleus in the electron's reference frame and $\mathbf{E} = -\nabla V(r) = -\frac{dV(r)}{dr}\frac{1}{r}$ is the electric field generated by a positive charge which is related to the electrostatic potential V(r). The magnetic field's expression becomes:

$$\mathbf{B} = \frac{1}{c^2}\mathbf{r} \times \mathbf{v}\frac{1}{r}\frac{dV(r)}{dr} = \frac{1}{mc^2}\mathbf{L}\frac{1}{r}\frac{dV(r)}{dr} \tag{1.4}$$

where $\mathbf{L} = \mathbf{r} \times \mathbf{p} = m\mathbf{r} \times \mathbf{v}$ is the nucleus's angular momentum.
The magnetic field interacts with the electron magnetic moment $\boldsymbol{\mu} = -\frac{e}{m}\mathbf{S}$:

$$H_{\mathrm{SO}} = -\mu \cdot \mathbf{B} = \frac{e}{(mc)^2}\frac{1}{r}\frac{dV(r)}{dr}\mathbf{S} \cdot \mathbf{L} \tag{1.5}$$

Considering a hydrogen-like atom, the electrostatic potential is $V(r) = \frac{1}{4\pi\epsilon_0}\frac{Ze^2}{r}$ and the Hamiltonian becomes:

$$H_{\mathrm{SO}} = \frac{Ze^3}{8\pi\epsilon_0(mc)^2 r^3}\mathbf{S} \cdot \mathbf{L} \tag{1.6}$$

Considering an electron with quantum numbers n and l, in a hydrogen-like atom one can write:

$$< r^{-3} >_{n,l} = \frac{2Z^3}{{a_0}^3 n^3 l(l+1)(2l+1)} \tag{1.7}$$

where a_0 is the Bohr radius. Finally the expression of the spin-orbit Hamiltonian is found to be:

$$H_{\mathrm{SO}} = \lambda \mathbf{S} \cdot \mathbf{L} \tag{1.8}$$

with $\lambda = \frac{e^3}{4\pi\epsilon(mc)^2{a_0}^3}\frac{1}{l(l+1)(2l+1)}\frac{Z^4}{n^3}$. λ, the SOC constant, is representative of the SOC strenght and it is proportional to Z^4. Therefore, the spin-orbit effect is much stronger for heavier elements.

1.1.3. Beyond the Hubbard paradigm: new topological phases

Combining the Hubbard Hamiltonian and the spin-orbit coupling, the total energy of the system can be written as followed:

$$H = -t \sum_{<i,j>} \sum_{\sigma} (c^{\dagger}_{i\sigma} c_{j\sigma} + c_{i\sigma} c^{\dagger}_{j\sigma}) + U \sum_{i} n_{i\uparrow} n_{i\downarrow} + \lambda \sum_{i} \mathbf{S}_i \cdot \mathbf{L}_i \tag{1.9}$$

A schematic phase diagram proposed by Witczak-Krempa [11] is shown in Fig. 1.5, where the competition between the electronic correlation and the spin orbit coupling constant λ is taken into account in terms of U/t and λ/t.

When the SOC is weak (left part of the diagram in Fig. 1.5), as in the case of $3d$ TMOs,

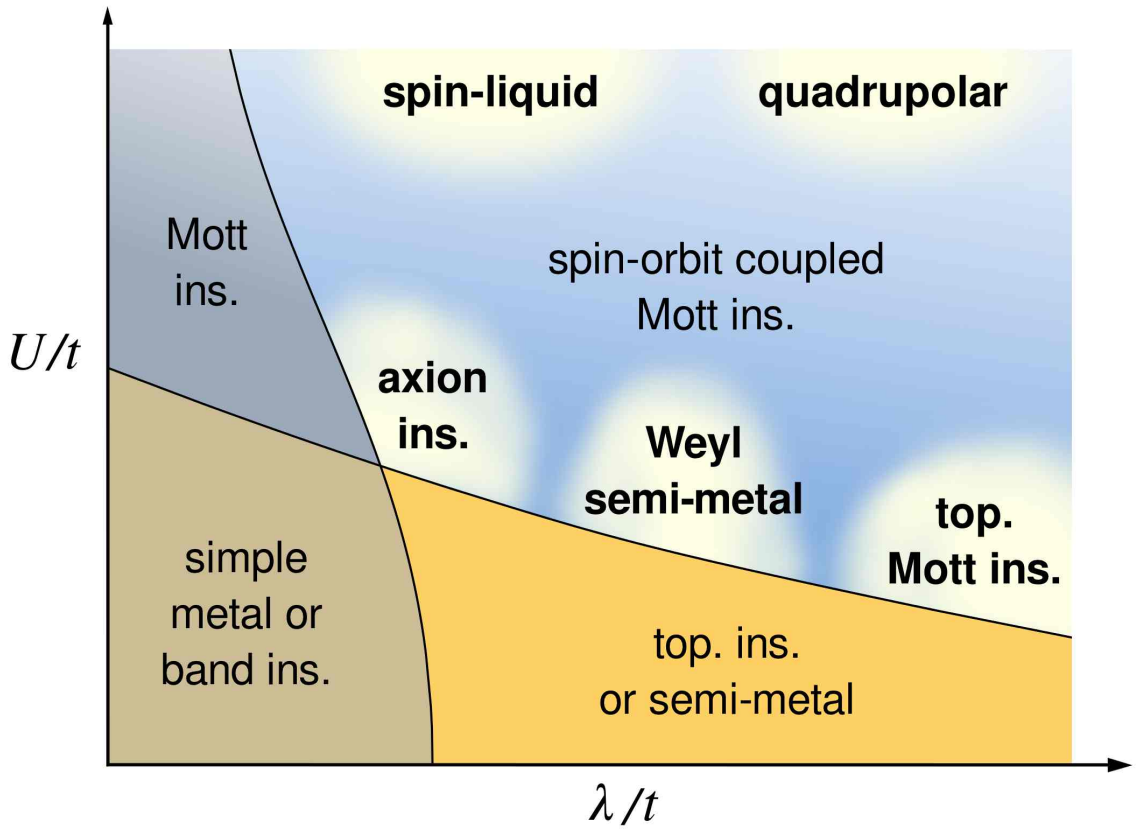

Figure 1.5: *U/t vs λ/t phase diagram established from eq. 1.9. On the left: Mott Hubbard model. On the right: new emergent phases. From [11].*

the Mott Hubbard model is recovered. When the SOC is strong (right part of the diagram) more exotic phases are observed.

It turns out that materials containing heavy elements are likely to present the phenomenon

of "band inversion" (see Fig. 1.6) [12]. If a gap is opened by spin orbit coupling, this band inversion results in a non-trivial topological band structure, as in the case of topological insulators (TI) and Weyl semimetals (WSM) [13–16]. A topological material is a system whose properties can not be changed without changing its fundamental nature.

Topological insulators are insulating in the bulk but they have gapless surface conduction

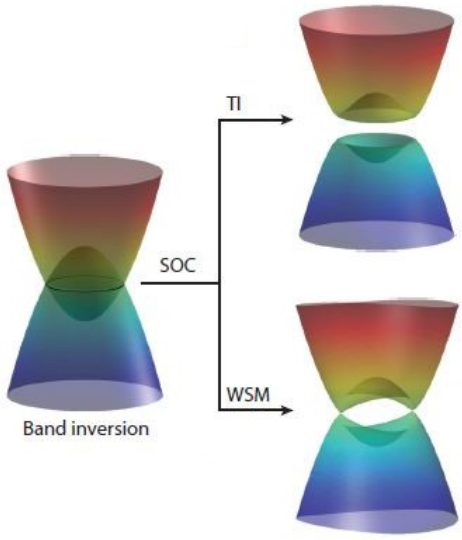

Figure 1.6: *Band topology in topological insulators and Weyl semimetal comes from the phenomenon of band inversion specific to heavy elements. The spin-orbit coupling opens a gap in the case of the topological insulator (TI) and gives rise to conductive surface states. In Weyl semimetals (WSM), the gap also opens, except at certain crossing points where the dispersion is linear, called Weyl points. From [17].*

states. These states are robust and insensitive to smooth perturbations of the Hamiltonian. This topological phase has been realized in some compounds such as HgTe [18, 19] and Bi_2Se_3 [20, 21].

Another topological phase is the Weyl semimetal phase (WSM). A Weyl semimetal has also gapped bulk bands apart from some points in which two non-degenerate bands cross linearly (see Fig .1.6). Those points are the so-called *Weyl points* (see Fig. 1.7a) and they are rigid against perturbations. Their quasiparticle excitations are the so called *Weyl fermions* and they are the three-dimensional analogous of the massless Dirac fermions in graphene. However, they are characterized by a definite chirality, either left-handed or right-handed, which is an indication of how the particle's spin is aligned with its momentum and they always come in pairs with opposite chirality. The two Weyl nodes with opposite chirality are connected through a surface state called *Fermi Arc*, as represented in Fig. 1.7a, which is an hallmark of the Weyl semimetal phase. These materials

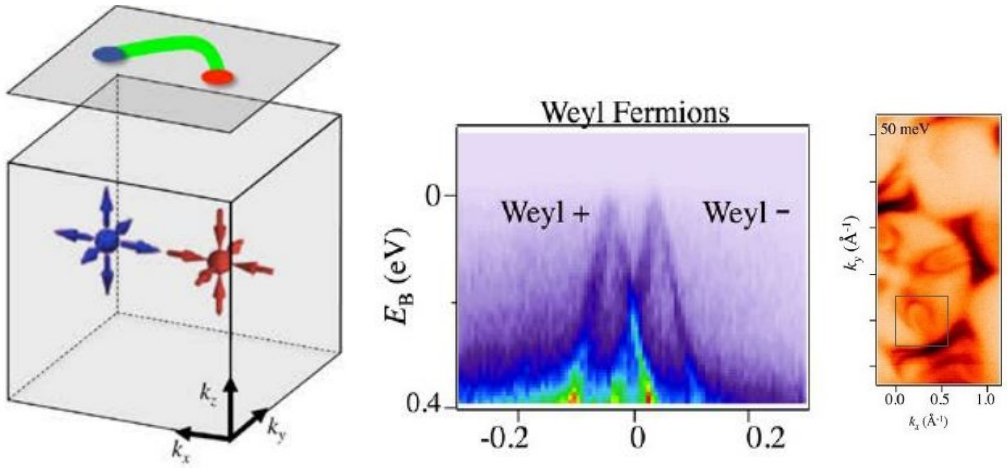

(a) (b) (c)

Figure 1.7: *(a) Electronic structure of Weyl semimentals: two Weyl points with opposite chirality are indicated in blue and red. The two Weyl nodes with opposite chirality are connected through a surface state called Fermi Arc. (b) Evidence of the Weyl cones in a TaAs crystal, obtained with ARPES measurements, from [22]. (c) Evidence of horseshoe-shaped Fermi arcs on TaAs crystal surface, obtained with ARPES measurements, from [22].*

are extremely interesting from the application point of view, since they are characterized by exceptional opto-electronic properties, such as extremely high mobility.
The Weyl semimetal phase can be obtained from the breaking of some symmetries, such as time reversal symmetry or inversion symmetry.
Historically, the first materials which were predicted to realize the WSM phase are pyrochlore iridates $R_2Ir_2O_7$ (with R a rare-earth element), within the family of iridium oxides. Their peculiar magnetic structure allows to break the time reversal symmetry while preserving inversion symmetry and therefore realizing a magnetic WSM. However, no real evidence of a WSM state has been observed in these compounds despite many experimental efforts.
In 2015 Su-Yang Xu et al. [22] reported the first observation of Weyl fermions in a TaAs crystal. However, unlike pyrochlore iridates, this system is not magnetic and is described with no correlations. The inversion symmetry breaking allows the observation of the Weyl semimetal state. Fig. 1.7b and Fig. 1.7c show respectively the evidence of the Weyl cones in TaAs crystal and Fermi arcs on TaAs crystal surface obtained with ARPES measurements [22].

The present work describes the study of pyrochlore iridates with the aim of understanding

whether the WSM state can be achieved in these crystals. In the next section I will discuss the physics of iridates, explaining in particular the realization of the $J_{\text{eff}} = 1/2$ state and its impact on the electronic and magnetic properties in iridate oxide systems.

1.2. Physics of iridium oxides

1.2.1. $J_{\text{eff}} = 1/2$ ground state in Iridates

Considering free iridium ions Ir^{4+} ($5d^5$), five electrons occupy five degenerate d orbitals (d_{xy}, d_{xz}, d_{yz}, $d_{x^2-y^2}$, d_{z^2}), whose angular distribution is represented in Fig. 1.8

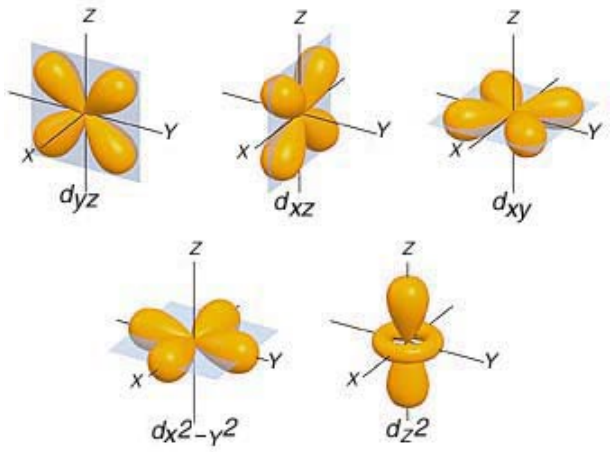

Figure 1.8: *Angular distribution of d-orbitals.*

The way the $5d$ electrons fill the d orbitals in the ground state can be found considering Hund's rules and it is defined through the assignment of the values of the angular momentum quantum numbers S (spin quantum number), L (orbital angular momentum quantum number) and J (total angular momentum quantum number):

- Maximize S: the maximization of the total spin S implies that electrons arrange with parallel spin in different orbitals reducing the Coulomb repulsion.
- Maximize L: among the states that maximize S the ground state is characterized by the maximum angular momentum L. This second rule also has the foundations in the minimization of the Coulomb repulsion.
- The total angular momentum is $\mathbf{J} = \mathbf{S} + \mathbf{L}$ with possible quantum numbers $J = L + S, L + S - 1, ...|L - S|$. If the shell is less than half full the ground state is characterized by $J = |L - S|$, if it is more than half full $J = L + S$. This third rule derives from the minimization of the spin-orbit energy.

However, ions in a real system are never isolated and thus it is necessary to consider their local environment. Each ion in a crystal feels an electric field due to the presence of the neighbouring ions. This electric field is called *crystal field* and it is strongly dependent on the symmetry of the local environment of the ions.
In many iridates, iridium ions have an octahedral environment whose vertices are occupied by oxygen ions. The presence of oxygen ions with their electrons lifts the degeneracy of the d orbitals. The latter can be classified in two groups: the t_{2g} orbitals with lobes pointing in between the axes (d_{xy}, d_{xz} and d_{yz}) and the e_g orbitals with lobes pointing along the axes (d_{z^2} and $d_{x^2-y^2}$). The energy of t_{2g} states is lowered in a octahedral environment and the one of e_g states is increased. Indeed the overlap between e_g (Fig. 1.9a) orbitals and p-orbitals of oxygen ions is larger than between t_{2g} and p-orbitals (Fig. 1.9b).

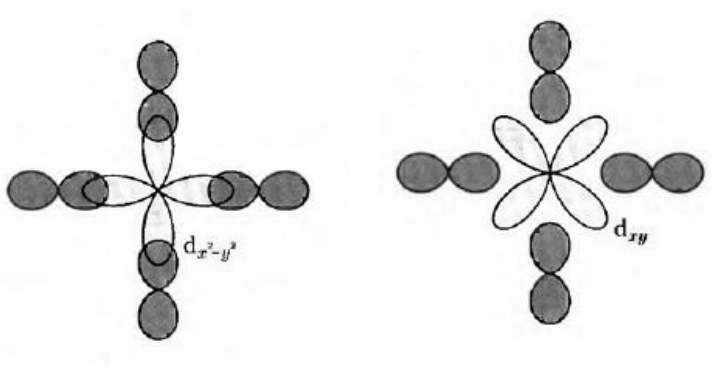

(a) (b)

Figure 1.9: *In an octahedral environment the oxygen ions are placed at the vertices of an octahedron whose center is the transition-metal ion. (a) e_g orbitals of the transition metal ion point along the p orbitals of the oxygen ions. (b) t_{2g} orbitals point in between the p-orbitals of the oxygen ions and are thus are subjected to a weaker Coulomb repulsion. From [23].*

This energy splitting due to the crystal field, shown in Fig. 1.10 as $10D_q$, is quite large in iridates ($\sim$ 2-3 eV). Therefore, the system lowers its energy by placing the five electrons in the t_{2g} states and leaving the e_g states empty. Thus the system is in a low spin configuration with $S = 1/2$.
One can calculate [9] $< t_{2g}|L_x|t_{2g} >$, $< t_{2g}|L_y|t_{2g} >$ and $< t_{2g}|L_z|t_{2g} >$ and find matrix elements of same magnitude and opposite sign to those of p states. Therefore, t_{2g} states can be considered as a triplet of states with effective orbital angular momentum $L_{eff} = -1$.
The strong SOC in iridium oxides compounds will then further split the degeneracy of the t_{2g} states in a $J_{\text{eff}} = 1/2$ and $J_{\text{eff}} = 3/2$ states, as represented in Fig. 1.11. Therefore,

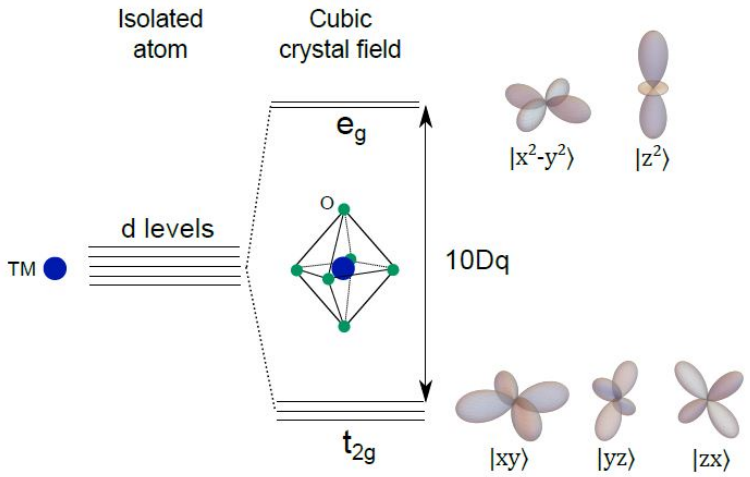

Figure 1.10: *Splitting of the d energy levels due to crystal field. The energy splitting is called $10D_q$. From [24].*

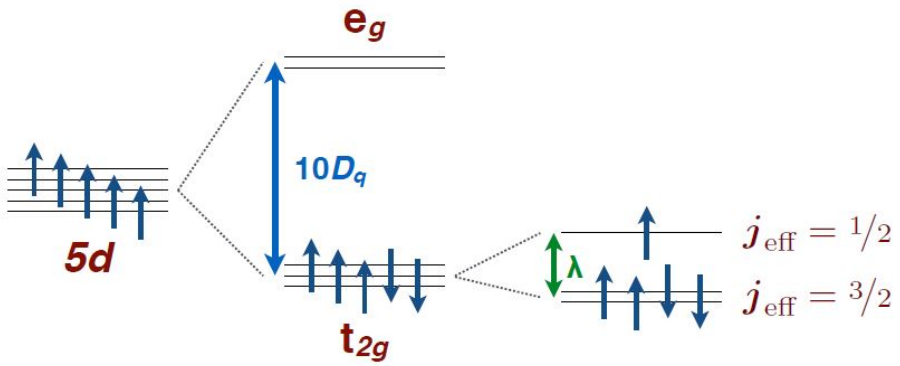

Figure 1.11: *Representation of the d energy levels for an isolated Ir^{4+} ion on the left, in the presence of an octahedral environment at the center and with SOC on the right. From [9].*

four electrons will fill the $J_{\text{eff}} = 3/2$ state and only one electron will place in the $J_{\text{eff}} = 1/2$ state, leaving a hole in the latter.
Let us now elaborate the effect of the SOC on the electronic properties in a periodic structure of atoms, in other words a crystal.

1.2.2. Effect of SOC on electronic structure

Energy levels are replaced by bands taking into account the whole crystal: in Fig. 1.12 (a) the t_{2g} band is shown. Fig. 1.12 (b) represents the splitting of the t_{2g} band due to Coulomb interaction according to the SOC-less Hubbard Hamiltonian. When only SOC is considered, the t_{2g} band is split into a fully-occupied $J_{\text{eff}} = 3/2$ band and an half-filled

$J_{\text{eff}} = 1/2$ band with lower bandwidth with respect to the original one (Fig. 1.12 (c)). As a consequence, when SOC is considered, a lower value of the Coulomb repulsion is needed in order to open a gap and make the material behave as a Mott insulator (see Fig. 1.12 (d)). Therefore, the introduction of SOC in the description is able to give an explanation of the insulating state of most of iridium oxide compounds. This effect was first observed and understood in Sr_2IrO_4 by Kim et al. [25].

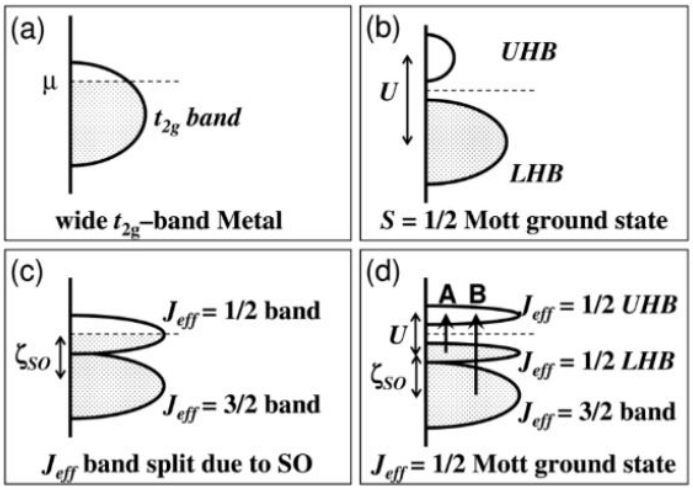

Figure 1.12: *Representation of the energy diagrams for $5d^5$ configuration (a) without Coulomb repulsion and SOC, (b) with large Coulomb repulsion and in absence of SOC, (c) with SOC and without Coulomb repulsion, (d) with SOC and with Coulomb repulsion. From [25].*

In addition to having a strong influence on the electronic properties, the SOC is also a source of magnetic anisotropy and strongly influences the magnetic properties of such systems.

1.2.3. Effect of SOC on magnetic properties

The spin orbit interaction strongly affects also the magnetic properties. The magnetic interactions of transition metal oxides are typically governed by the superexchange between the magnetic ions mediated by the 2p orbitals of the oxygen placed in between them. The anisotropy of these magnetic interaction derives from the SOC since it entangles the spin and the orbital degree of freedom. In other words, without SOC, the spin would not have any reason to align along a certain direction and the system would keep a SU(2) symmetry (isotropic interaction). Thus in the strong SOC regime the magnetic interactions are strongly dependent on the symmetry of the crystal lattice as well as the geometry of the bonds. The seminal work of Jackeli and Khaluillin [26] has established that two types of

magnetic interactions exist depending on the superexchange geometry:

- Heisenberg interaction for a corner sharing geometry, as represented in Fig. 1.13a. In this case the Ir-O-Ir angle is of 180°.
- Kitaev type interaction for a edge sharing geometry, with a Ir-O-Ir angle of 90° (see Fig. 1.13b).

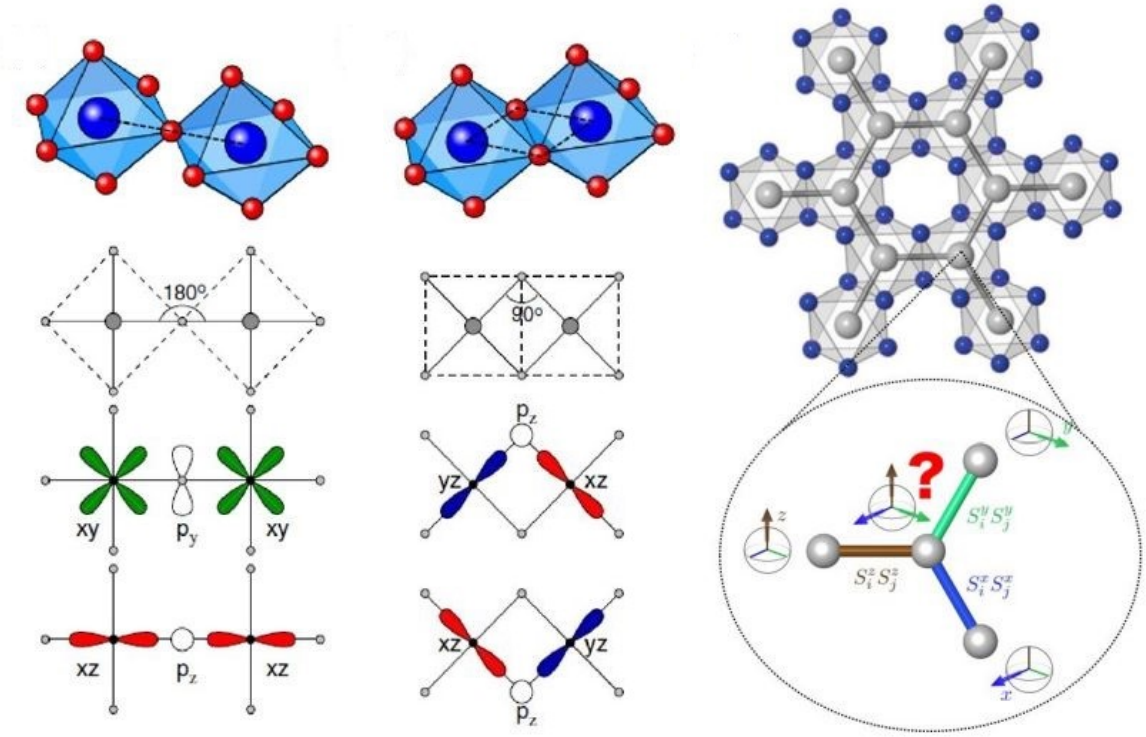

(a) (b) (c)

Figure 1.13: *(a) Corner sharing geometry: the Ir-O-Ir angle is of 180° and the interaction between the Ir magnetic moments is an isotropic Heisenberg interaction. (b) Edge sharing geometry: the angle Ir-O-Ir is of 90°. The Heisenberg interaction is suppressed due to the destructive intereference between the two superexchange paths (via the upper and lower oxygen). In this case, the interaction is of Kitaev type. (c) Honeycomb lattice with anisotropic interactions depending on the orientation of the bonds. The system is highly frustrated in terms of magnetic interactions on one site, i.e. that the spin at site i wants to align along the x, y, z directions at the same time. This geometry is the cornerstone of the experimental realization of the Kitaev physics and is realized e.g. in $Na2IrO_3$ or alpha-$RuCl_3$. From [26, 27].*

This latter interaction arises from the fact that the two superexchange paths, via the upper and lower oxygen ions, interfere destructively, thus canceling the isotropic term.

The interaction arising is anisotropic and it is dependent on the spatial orientation of the bond. For a given bond ij in the plane perpendicular to $\gamma = (x, y, z)$, the magnetic Hamiltonian can be written as:

$$H_{\mathrm{ij}}{}^{(\gamma)} = -K_\gamma S_{\mathrm{i}}{}^{(\gamma)} S_{\mathrm{j}}{}^{(\gamma)} \tag{1.10}$$

For a honeycomb lattice, the sum over the contributions of all different bonds of type eq.1.10 corresponds to the Kitaev model:

$$H = -\sum_{<ij>_\gamma} K_\gamma S_{\mathrm{i}}{}^{\gamma} S_{\mathrm{j}}{}^{\gamma} \tag{1.11}$$

This model describes honeycomb lattices of $1/2$-spins interacting with nearest-neighbouring spins through bond-dependent-easy-axis Ising interaction, as illustrated in Fig. 1.13c. This model is analytically solvable and its ground state is a quantum spin liquid [27]. A quantum spin liquid is an exotic state of matter in which spins do not order even at $T = 0K$ due to quantum fluctuations. Some signature of the Kitaev interactions have been found in some compounds having a quasi-2D honeycomb lattices such as alpha-$RuCl_3$, Li_2IrO_3 and Na_2IrO_3 [27–30]. However, the realization of ideal interactions of the Kitaev type is still subject of research. Indeed, Coulomb repulsions between 2D honeycomb layers induce distortions of the octahedron, hence bringing the TM-O-TM angle away from the ideal 90° case. This results in a small, yet not negligible, isotropic interaction that will compete with the Kitaev term and therefore leads the system away from a quantum spin liquid state. Also longer than nearest-neighbours range interactions may be relevant in some cases bringing the system away from the pure Kitaev model.

Another interesting interaction arising from the spin-orbit coupling, particularly relevant for this master thesis, is the so-called antisymmetric exchange interaction, also called *Dzyaloshinskii-Moriya* interaction (DMI). Moriya demonstrated [31] that, when considering the SOC ($\lambda \mathbf{L} \cdot \mathbf{S}$) and expanding in powers of λ, the magnetic Hamiltonian describing the interaction between two spins ($\mathbf{S}_i$ and $\mathbf{S}_j$) becomes:

$$H_{\mathrm{ij}} = J\mathbf{S}_i \cdot \mathbf{S}_j + \mathbf{D}_{ij} \cdot (\mathbf{S}_i \times \mathbf{S}_j) + \mathbf{S}_i \cdot \Gamma_{ij} \cdot \mathbf{S}_j + ... \tag{1.12}$$

The first term is the isotropic Heisenberg exchange with $J \propto \lambda^0$. The second term is the anisotropic Dzyaloshinskii-Moriya term and the modulus of $\mathbf{D}_{ij}$ is proportional to λ. The third term is another anisotropic exchange term with Γ_{ij} a symmetric tensor related to

λ^2. The Dzyaloshinskii-Moriya interaction is present under certain conditions: the bond between the two spins must not hold inversion symmetry.

The effect of this interaction is to cant the spins (see Fig. 1.14) and in the case of an

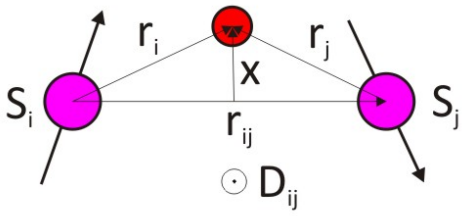

Figure 1.14: *Scheme of the Dzyaloshinskii-Moriya interaction between two spins. It introduces a ferromagnetic component in the interaction by canting the spins. From [23].*

antiferromagnet it introduces a small ferromagnetic contribution (weak ferromagnetism). This interaction is not present in highly symmetric crystals, but it is of relevant importance in some compounds, such as pyrochlore crystals [32]. In these compounds, antiferromagnetic interactions between nearest neighbours bring to frustration preventing long range magnetic order. If DMI is present, frustration is removed and long range order is established.

Now I will introduce the pyrochlore crystal structure, focusing in particular on pyrochlore iridates which are the main subject of this master thesis.

1.3. Pyrochlore iridates

In the class of iridium oxides there are different families of crystal structures all characterized by specific properties. Within them, pyrochlore iridates have attracted major interest. Indeed, the interplay of strong SOC and electronic correlations in these compounds is expected to realize novel phases of matter such as the magnetic WSM.

1.3.1. The crystal structure of pyrochlores

Pyrochlore crystals have stoichiometry $A_2B_2O_7$, where A is a trivalent rare-earth element and B a tetravalent transition metal. The crystal structure is represented in Fig. 1.15a. It is a face-centered-cubic (fcc) structure (see Fig. 1.15b for the Brillouin zone of the fcc sublattices) and the space group is $Fd\bar{3}m$ (No. 227). The transition metal and rare-earth ions form two interpenetrating pyrochlore, corner sharing tetrahedral lattices (see Fig. 1.15c), each with sixteen atoms per unit cell. The oxygen ions form an octahedral environment around transition metal ions.

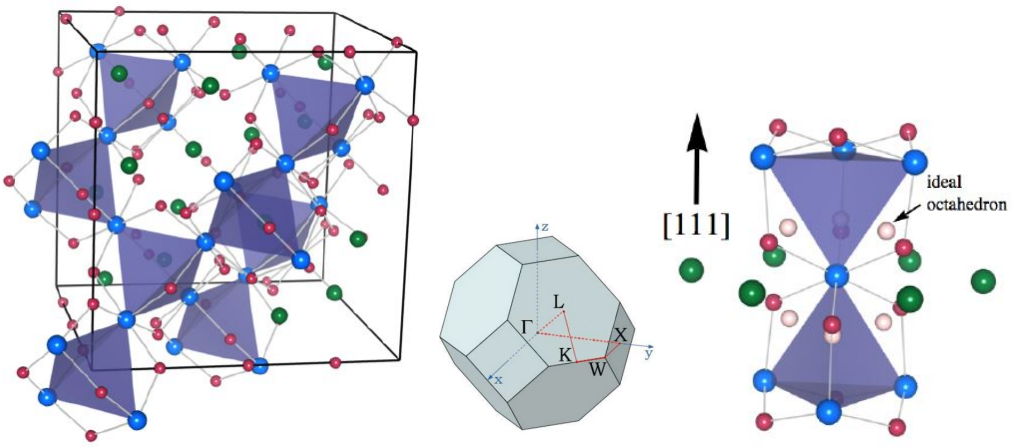

(a) (b) (c)

Figure 1.15: *(a) Schematic representation of the pyrochlore structure. A ions are represented in green, B ions in blue and oxygen ions in red. (b) Brillouin zone for a fcc lattice. (c) Corner sharing tetrahedral lattice formed by iridium and rare-earth atoms. The ideal octahedral environment formed by oxygen atoms around Ir ions is shown. From [11].*

Pyrochlore crystals can be subjected to frustration. A crystal is said to be frustrated when the different magnetic interactions cannot all be satisfied simultaneously. This can happen both because of competing interactions or because of the geometry of the crystal lattice.

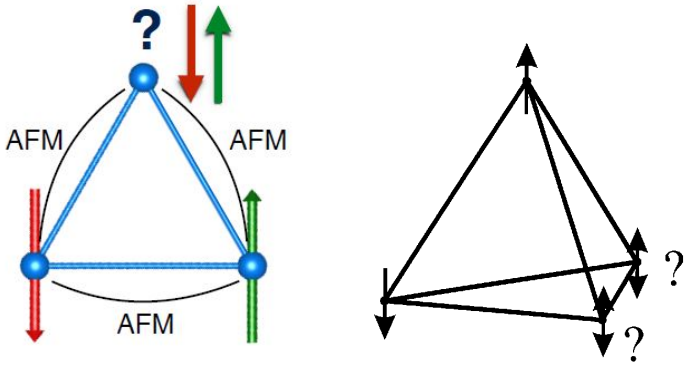

(a) (b)

Figure 1.16: *(a) Geometrical frustation in a triangular lattice. (b) Geometrical frustation in a pyrochlore lattice.*

A typical example to explain geometrical frustration consists of a triangular lattice with spins interacting antiferromagnetically. If a spin is placed on one corner, then the second spin can be placed antiparallel to the first, but with the third spin a problem arises. It is not possible to arrange the system in such a way that the third magnetic moment is

antiparallel to both the other two magnetic moments (see Fig. 1.16a). In three dimensions, an analogous example of geometric frustration is found in pyrochlore lattices with spins interacting antiferromagnetically as shown in Fig. 1.16b.

1.3.2. State of the art

Historically, pyrochlore crystals have been studied with non-magnetic transition metals, such as Ti, Sn, and Mo, to focus on the magnetism of rare earth ions. As a consequence of magnetic frustration, a wide variety of fascinating behaviors has been observed. Pyrochlore titanates $Ho_2Ti_2O_7$ and $Dy_2Ti_2O_7$ [33–36] and pyrochlore stannates $Ho_2Sn_2O_7$ and $Dy_2Sn_2O_7$ [37] were discovered to be spin ices. A spin-glass behaviour has been observed in $Y_2Mo_2O_7$ [38], while $Tb_2Ti_2O_7$ has been found to be a spin liquid [39].
Later on, people started to be interested in pyrochlore crystals in which both the rare-earth and transition metal sites posess magnetic moments. This is the case for some pyrochlore iridates.
Initially the magnetic structure formed by the iridium ions remained ambiguous. Theoretical works [40–42] predicted that the Ir sublattice orders in a so-called *All-In-All-Out* (AIAO) magnetic configuration: spins point either inside or outside the tetrahedra as represented in Fig. 1.17. This structure breaks the time reversal symmetry while preserving the inversion symmetry and it is stabilized by the Dzyaloshinskii Moriya interaction which removes frustration.

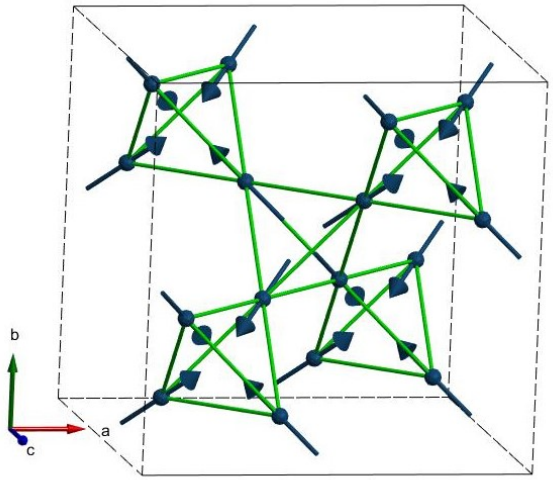

Figure 1.17: *All-In-All-Out (AIAO) magnetic structure of the iridium sublattice.*

The small magnetic moment of Ir^{4+} and the strong neutron absorption of iridium makes the direct experimental probing of the magnetic structure of the iridium sublattice through

usual neutron scattering arduous. Results of resonant X-ray scattering [43, 44] and muon spin relaxation [45, 46] on pyrochlore iridates with non-magnetic rare-earth ions (Eu, Y) were compatible with a AIAO configuration of the iridium spins. In particular, Sagayama et al. stated that the only magnetic structure compatible with the absence of structural distortion they found is the AIAO structure [43].
Confirmation of the AIAO structure has been supplied by neutron scattering experiments indirectly probing the magnetic structure of the rare-earth ions, which have a larger magnetic moment. Rare-earth ions feel the molecular field generated by the iridium magnetic structure and consequently order in a AIAO configuration. Tomiyasu et al [47] found a AIAO magnetic ordering of Nd ions in $Nd_2Ir_2O_7$, reflecting a AIAO configuration of the iridium ions. A similar result has been found in $Tb_2Ir_2O_7$ [48].
Later, Guo et al. [49] reported the first successful direct measurements of the Ir ions' magnetic structure by powder neutron diffraction on $Nd_2Ir_2O_7$ [49].
The magnetic structure remains unchanged when changing the rare-earth element, but the electronic structure varies. In particular, the properties of pyrochlore iridates are strongly affected by the dimensions of the rare-earth ion. The trend of the ionic radius along the periodic table is reported in Fig. 1.18. The ionic radius increases while going down and moving left through the periodic table.

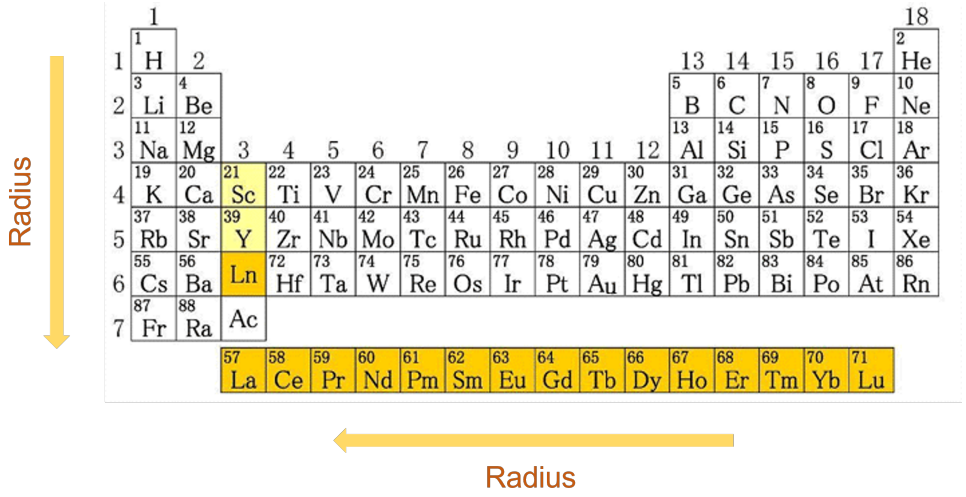

Figure 1.18: *Periodic table of elements with the trend of the ionic radius. It increases going down in the periods and moving to the left along the groups. The rare earths elements are represented in yellow boxes.*

Fig. 1.19a shows the phase diagram of pyrochlore iridates with varying temperature and ionic rare-earth radius calculated from transport and magnetism measurements. Three regions are distinguished: a magnetic insulating phase, a metallic phase, and a non-metallic phase.

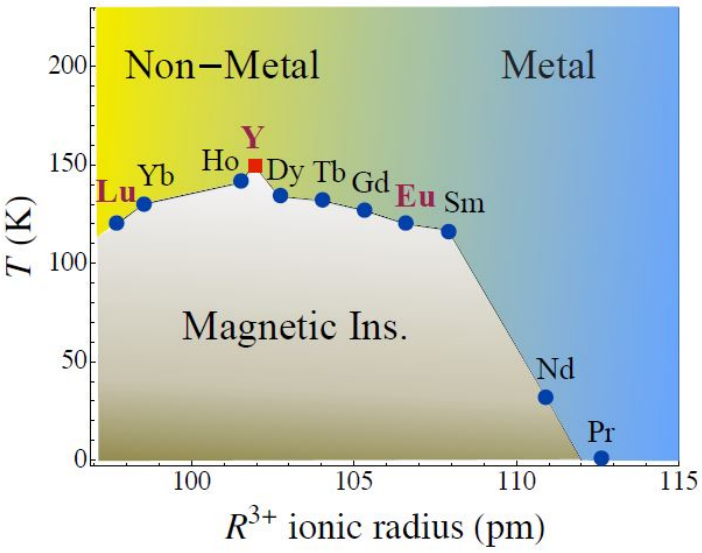

(a)

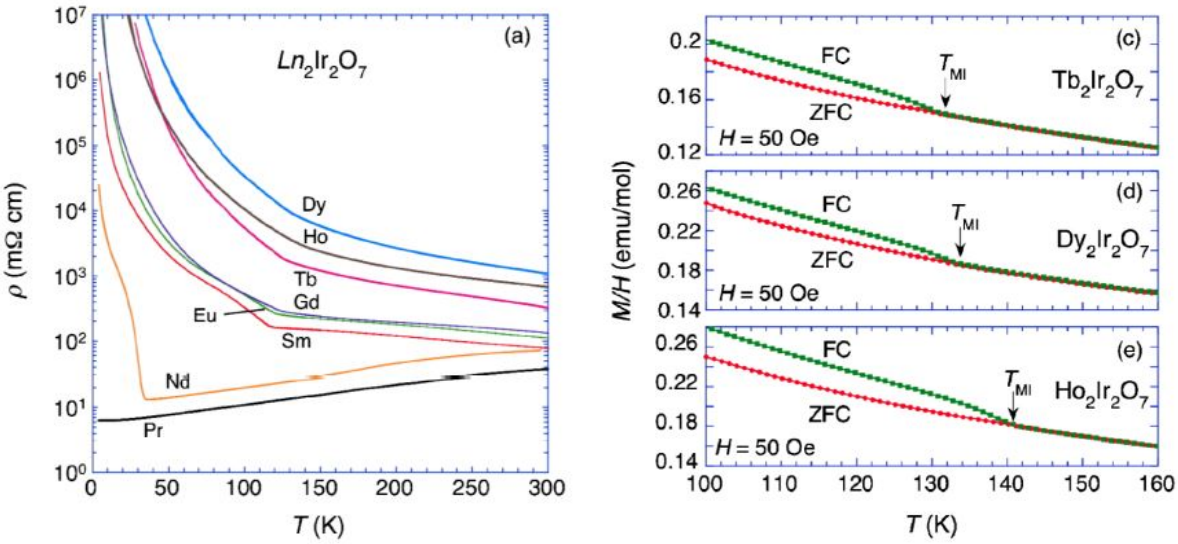

(b) (c)

Figure 1.19: *(a) Phase diagram for the pyrochlore iridates $R_2Ir_2O_7$. From [11]. (b) Resitivity measurements for polycrystalline pyrochlore iridates with different rare earths elements, from [37]. A metallic behaviour is depicted by a positive slope of the resistivity, while a negative slopes corresponds to an insulating behaviour. (c) FC-ZFC curves for $Tb_2Ir_2O_7$ on the top, $Dy_2Ir_2O_7$ at the center and $Ho_2Ir_2O_7$ at the bottom, from [37]. A magnetic transition is indicated by the bifurcation between the ZFC and FC curves.*

Resistivity measurements (see Fig. 1.19b) on powder samples show a divergence below a certain temperature for all pyrochlore iridates except for R = Pr, indicating metal-to-insulating transitions (MIT). Moreover, the resistivity is lower for larger rare earth

ionic radius (it increases from Pr to Dy). Thus, pyrochlore iridates with larger rare earth ionic radius have a more metallic behaviour. From Fig. 1.19b one can notice that the resistivity dependence on temperature changes from metallic ($d\rho/dT > 0$) to non-metallic ($d\rho/dT < 0$) for compounds with larger rare earth ions (in particular it is very clear for Nd). For the other compounds with smaller rare earth ionic radius the behaviour highlighted by the resistivity measurments is always non-metallic. In the case of $Pr_2Ir_2O_7$ the resistivity always has a positive slope down to T = 0 K, implying a metallic behaviour for all temperatures.

Magnetic measurements [37] (Fig. 1.19c) show a bifurcation between the zero-field cooled (ZFC) and the field-cooled (FC) susceptibility curves around 130 K for $Tb_2Ir_2O_7$, 135 K for $Dy_2Ir_2O_7$ and 140 K for $Ho_2Ir_2O_7$. It indicates a magnetic transition, which has been attributed to the arising of the AIAO magnetic structure at the iridium site.

A schematic phase diagram of pyrochlore iridates with varying electronic correlation and

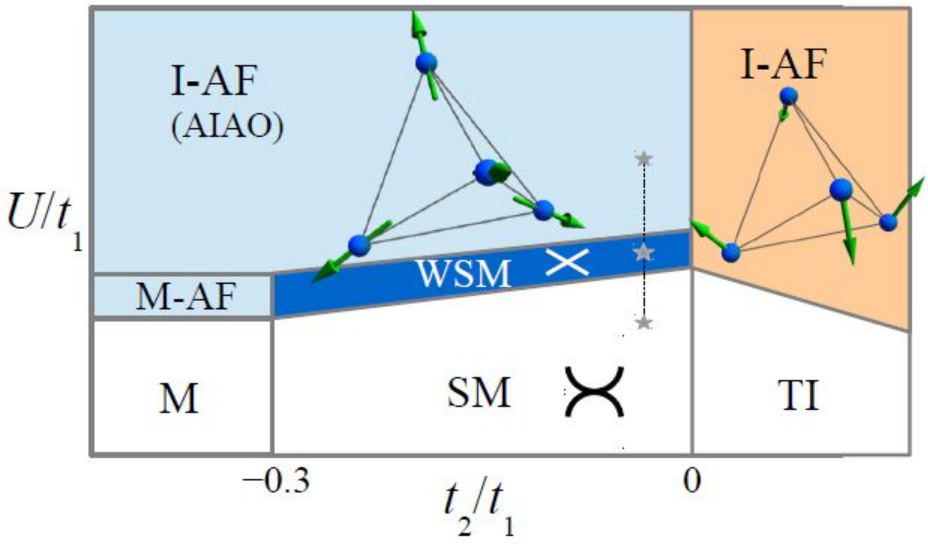

Figure 1.20: *Theoretical phase diagram of pyrochlore compounds calculated from the Hubbard model: U is the Coulomb repulsion and t_1 and t_2 hopping integrals. An insulating antiferromagnetic phase (I-AF) is predicted for strong correlations with a AIAO structure (light blue shaded region) or different magnetic structure (orange shaded region). For low correlation a metallic phase (M), a semimetallic phase (SM), and a topological insulating (TI) phase are predicted. In the intermediate regime a WSM phase or a metallic-antiferromagnetic phase (M-AF) are expected as ground state. From [40].*

hopping integrals is shown in Fig. 1.20. One can observe that for strong correlations the pyrochlore iridate crystal is in a Mott insulating and antiferromagnetic state (R = Lu, Yb), while for low correlations it behaves like a metal (R = Pr). However, in the interme-

diate correlation regime it is predicted that the ground state is the Weyl semimetal state (WSM).

Indeed, previous theoretical works on pyrochlore iridates advocated that two conditions should be met in order to realize a Weyl semimetal phase: the magnetic moments should organize in a AIAO structure (breaking the time reversal symmetry but preserving the cubic structure) and the correlation should be weak enough (otherwise the crystal would end up in a Mott insulating phase) [11, 40–42]. Intense research has been addressed to the study of these compounds in the past ten years. The first studies have been made employing inelastic neutron scattering [50, 51] on powder samples due to the difficulties to obtain single crystals [52].

More recently, experiments on single crystals of $Sm_2Ir_2O_7$ and $Eu_2Ir_2O_7$ [53, 54] by Resonant Inelastic X-Ray Scattering (RIXS) have been performed. Quantitative information about the interactions in the systems can be obtained through the comparison with theoretical calculations. Through the magnetic excitations, one can get an insight onto the electronic correlations. This is essential to understand where the compounds are placed in the phase diagram and whether they can present a Weyl semimetallic phase.

Fig. 1.21a represents the intensity map of RIXS spectra on $Eu_2Ir_2O_7$ [53]. Chun et al. [53] suggested that an intermediate correlation description whould be more appropiate to describe the evolution of the magnetic excitation spectrum with temperature rather than a local moment description.

Fig. 1.21b shows the dispersion relation of magnetic excitation in $Sm_2Ir_2O_7$ single crystal [54]. The numerical simulations have been performed within a local description taking into account the Heiseinberg exchange and the Dzyaloshinskii Moriya interaction between neighbouring magnetic moments. From the fit of the experimental data Donnerer et al. [54] estimated the strength of the magnetic interactions. This approach carries a crucial approximation: the electronic correlations are assumed to be strong.

In order to go further in the analysis of the data, one should employ more sophisticated methods based on the Random Phase Approximation (RPA) which is based on the Hubbard model. Fig. 1.22 reports the calculations of spin dynamics within RPA with different electronic correlations. For small values of the Coulomb repulsion the spin wave spectrum broadens throughout the Brillouin zone due to the interaction with a particle-hole continuum of excitations: the so-called *Stoner contiuum*. The attenuation of collective excitations due to the interaction with this continuum was first considered by Landau and is commonly referred to as *Landau damping*. As the correlations increase the continuum raises in energy and the spin wave modes are well defined. The Hubbard model in this case reduces to the Heisenberg model.

In the case of $Sm_2Ir_2O_7$ [54], while the magnetic spectra are well described by a spin wave

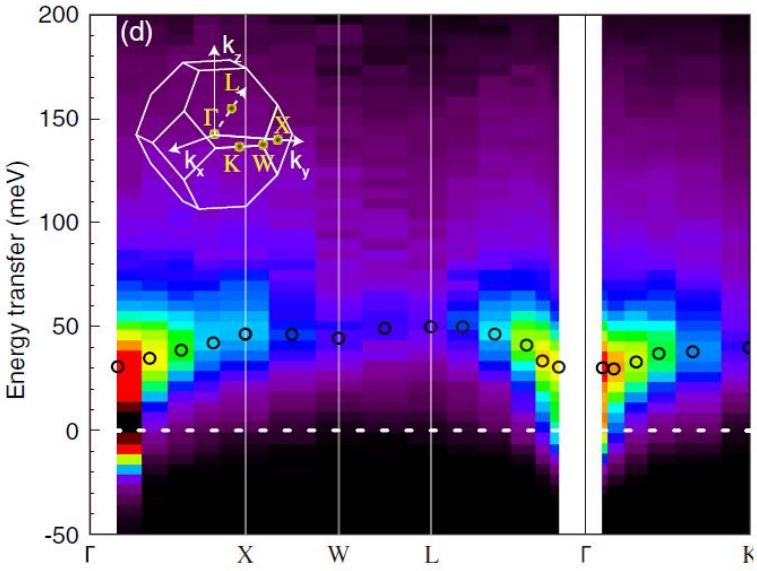

(a)

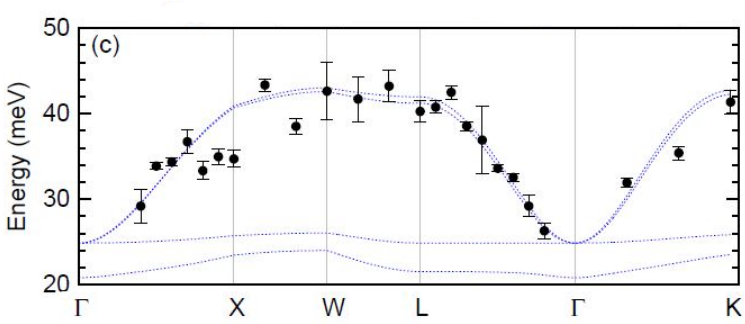

(b)

Figure 1.21: *(a) Intensity map of RIXS spectra on $Eu_2Ir_2O_7$ at $T = 7$ K from [53]. The circles represents the energy positions of magnons obtained from the fit of experimental data. (b) Experimental (black dots) and calculated (blue curves) dispersion relation of magnetic excitation in $Sm_2Ir_2O_7$. From [54].*

model, i.e. strong correlations, the width of the magnons seems to increase while moving from the Γ point thus pointing out "intermediate correlations".

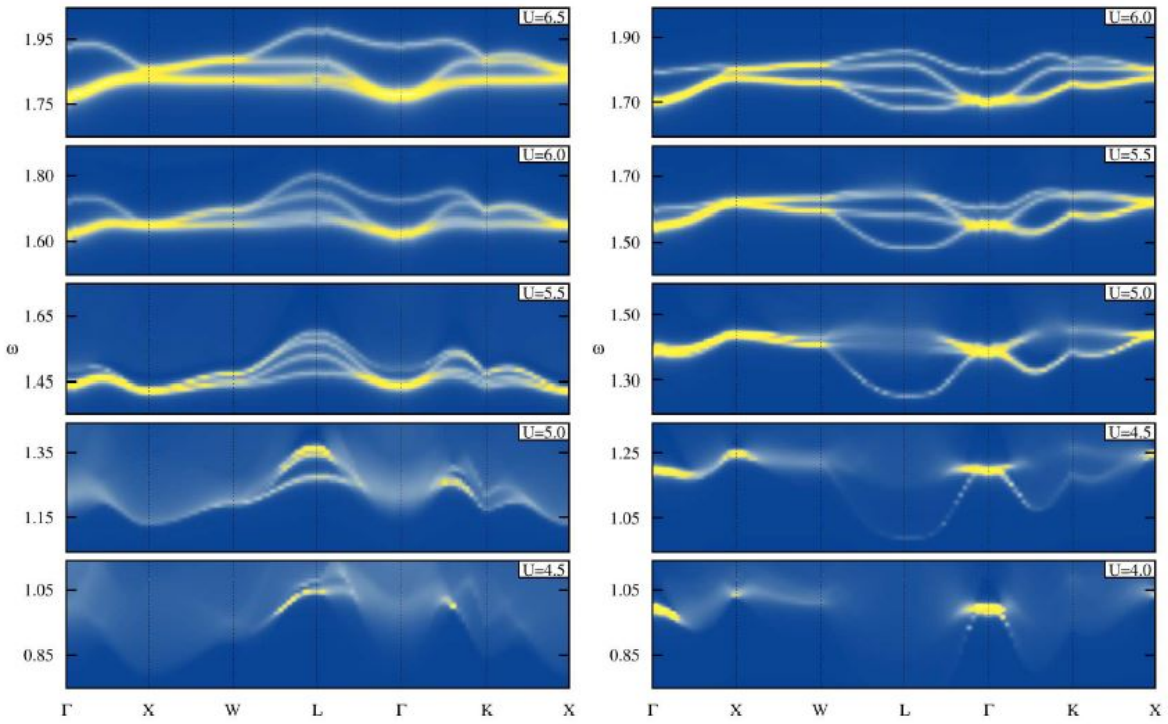

Figure 1.22: *Spin dynamics in a AIAO magnetic structure from RPA calculations with different electronic correlations U. ω is in units of t = 1 with t hopping integral. The images on the left and on the right represent the intensity map for two cuts in the phase diagram corresponding to different hopping integrals. From [55].*

2 | Experimental and numerical techniques

The study of the excitations of a material allows to investigate its dynamical properties. Many experimental techniques have been developed for this purpose, such as Inelastic Neutron Scattering (INS), Resonant Inelastic X-Rays Scattering (RIXS) or Raman Spectroscopy.
An incident probe (neutrons, photons) transfers energy to an excitation that is created in the material by inelastic scattering. The energy transfer, which corresponds to the energy of the created excitation, can be measured by measuring the energy of the outgoing neutron/photon. Thus, these experimental techniques allow to obtain the energy loss spectrum. Various elementary excitations of different nature and energy scales can be observed (see Fig. 2.1), for example:

- Phonons are collective excitations representing the quantization of modes of vibrations in a crystal.
- Magnons are excited magnetic states, representing the quantization of spin waves and their dispersion relation contains information about the magnitude of the magnetic interactions of the system.
- The so-called *dd* excitations correspond to intra-orbital t_{2g} or t_{2g} to e_g excitations. They represent an electron hopping from one orbital to another and are hence related to the electronic structure induced by the crystal field.
- Charge transfer excitations represent the motion of electrons between different ions in the crystal.

The present work is mainly focused on the study of magnetic excitations. For many years the leading techinque employed for the study of excitations, especially magnetic ones, has been Inelastic Neutron Scattering. However, some limitations emerged. First of all INS requires samples of relatively large volume ($\sim mm^3$). Moreover, some elements are strong neutron absorbers (in particular iridium), therefore making it difficult to study

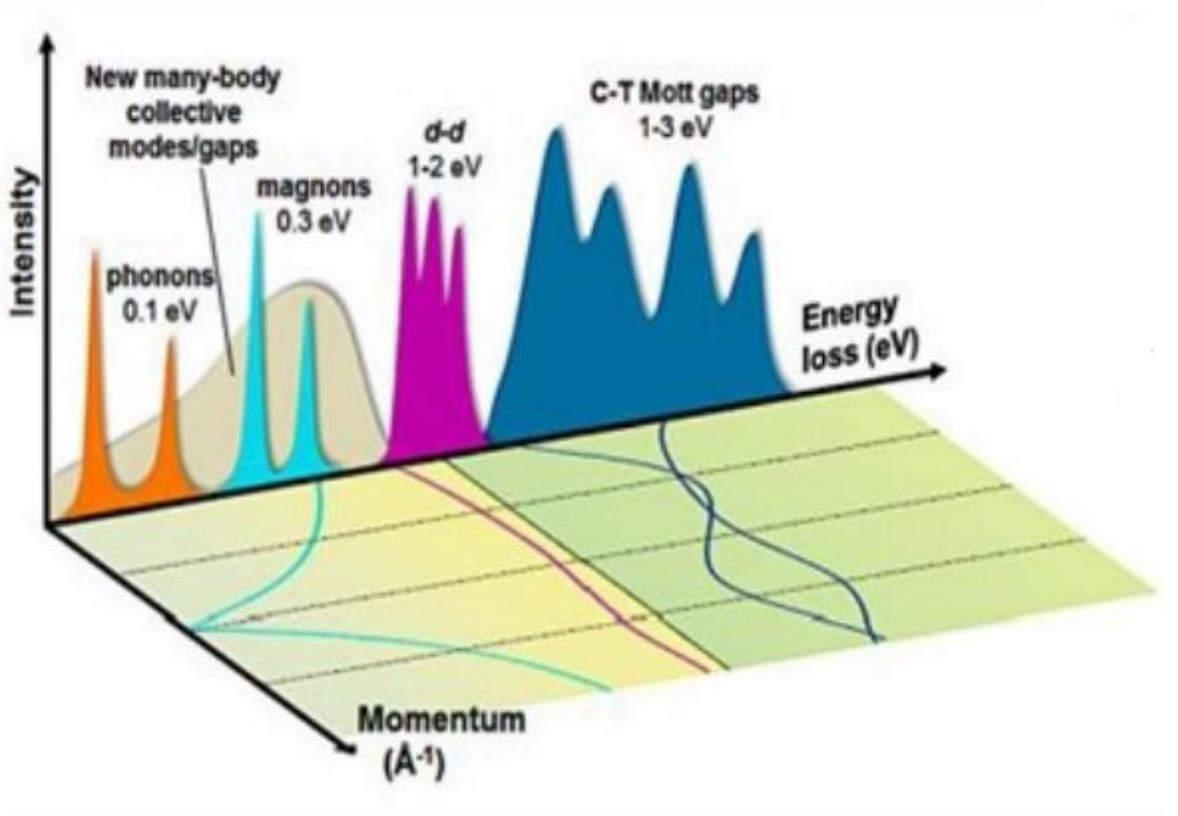

Figure 2.1: *Scheme of an energy loss spectrum: different features represent different types of excitations. The dispersions (relation between the energy and momentum) of the latter are also shown. From [56].*

them using neutron scattering experiments.
The availability of high brilliance synchrotron radiation, together with technological advances in some instrumentations such as monochromators, analyzers and spectrometers, laid the foundations for the possibility of new techniques of investigation of matter emplyoing X-rays.
Nowadays, inelastic X-ray scattering has become complementary to inelastic neutron scattering, especially when the size of the sample is not suitable for neutron scattering experiments. In particular, a large enhancement of scattering cross section was demonstrated when the energy of incoming photons is tuned to an absorption edge of an element. Such a technique is therefore called Resonant Inelastic X-Ray Scattering (RIXS).

In this chapter I will first introduce some generalities about synchrotron radiation, which is fundamental for the employment of RIXS to probe magnetic excitations. Then the RIXS technique is described and subsequently the setup of ID20, a RIXS dedicated beamline of the European Synchrotron Radiation Facility (ESRF) where I carried out my thesis

project, is outlined. The macroscopic techniques used for the characterization of samples are also briefly explained. Finally, I will discuss the SpinW software used to model the experimental dispersion spectra of the magnetic excitations.

2.1. Resonant Inelastic X-Rays Scattering (RIXS)

2.1.1. Generalities on synchrotron radiation

X-rays are electromagnetic waves in the energy range $\sim$ 100 eV - 120 keV [57]. They have been discovered by the German physicist Wilhelm Conrad Röntgen in 1895. From that moment they have been considered one of the main probes of the structure of matter, as their wavelength is comparable to inter-atomic distances (in the Å range). X-rays were mainly produced in X-ray tubes until the 1970s. The principal limitations in the use of X-rays resided actually in the source itself. Indeed, the brightness (flux emitted per unit surface and unit solid angle) of the radiation produced by X-rays tubes is quite low.
Synchrotron radiation was accidentely discovered in 1947 at General Electric in the United States [58], using a circular particle accelerator: a synchrotron. Indeed, electromagnetic waves are emitted when a charged particle is submitted to an acceleration. Around 1970 the first generation of synchrotron appeared: X-rays produced in accelerators for high-energy physics experiments were used in a parasitic mode. Around the 1980, second generation synchrotrons, dedicated to the use of X-rays produced by bending magnets, were built being the results obtained with the first ones very encouraging. In third gener-

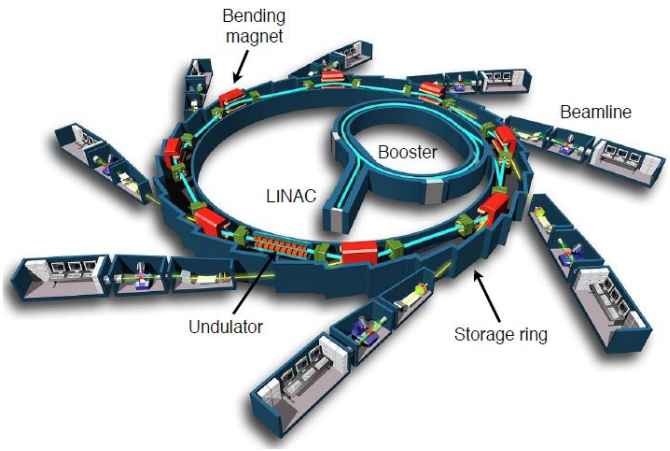

Figure 2.2: *Scheme of a third generation synchrotron. The main elements are: the electron gun, the LINAC, the Booster synchrotron, the storage ring (which contains undulators and bending magnets) and the beamlines. From [9].*

ation synchrotrons the brightness is increased by a factor $\sim 10^4$ due to the use of insertion devices, such as undulators and wigglers.
In Fig. 2.2 the approximate scheme of a third-generation synchrotron is shown. Electrons produced in an electron gun are accelerated in a linear accelerator (Linac). Electrons from the Linac enter the Booster synchrotron where they are accelerated to a given energy, through radiofrequency (RF) cavities, before being injected into the storage ring, schematically represented in Fig. 2.3. The latter is a tube where the electrons pass through several magnets and are accelerated producing radiation. The storage ring includes straight and

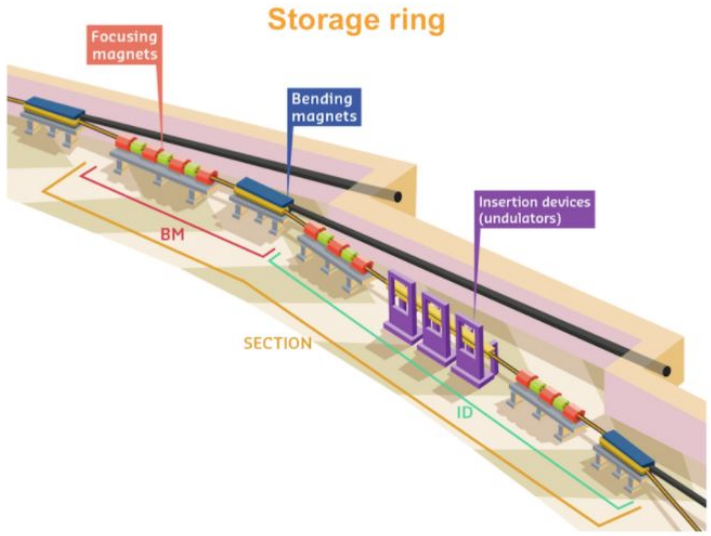

Figure 2.3: *Scheme of the storage ring. It is made by curved and straight sections hosting focusing magnets and insertion devices respectively [59].*

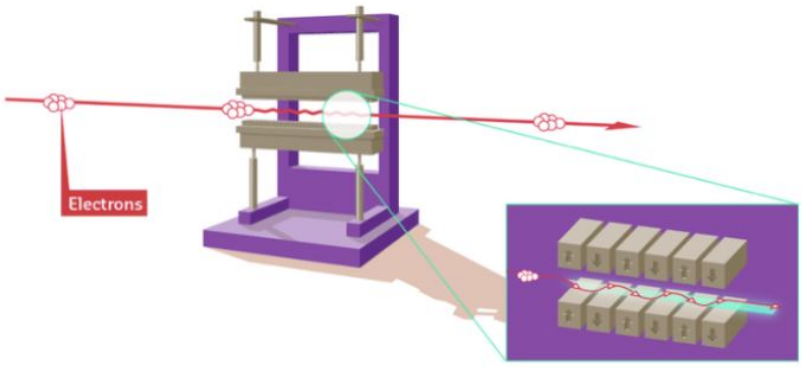

Figure 2.4: *Scheme of an undulator device. The electrons are forced to follow an undulating path and they emit X-rays [59].*

curved sections in alternating order. The straight sections host focusing magnets ensur-

ing electrons to remain close to the ideal orbital path and insertion devices (undulators or wigglers) producing intense X-rays beams. Undulators are magnetic structures which force electrons to follow an undulating trajectory, as shown in Fig. 2.4. Radiation is emitted due to the bending of the electrons trajectory. Light emitted at each bend interferes, generating a highly-brilliant X-ray beam with a narrow energy spectrum.
Wigglers are insertion devices similar to undulators but with stronger magnetic fields producing a wider oscillation of the electrons leading to a wider spectrum of the emitted radiation with respect to undulators.
Two bending magnets in the curved section bend the electrons into their racetrack orbit and cause the emissions of X-rays. The radiation produced in this case is less brilliant than in the case of insertion devices.
These beams of light emitted by the electrons passing throught bending magnets or insertion devices are directed towards the beamlines (BM or ID respectively).
The European Synchrotron Radiation Facility (ESRF) in Grenoble (France), which started to be built in the late 1980s, has been a third generation synchrotron until 2020 when, after a facility upgrade, became ESRF-EBS (ESRF-Extremely Brilliant Source), the first fourth generation synchrotron. The new storage ring is based on a hybrid multi-bend achromat (HMBA) and produces extremely brilliant X-rays by reducing the electron emittance [60, 61] towards the diffraction limit (diffraction limited storage rings [62]).

ID20 is a dedicated beamline for inelastic X-ray scattering in the hard-X-rays regime using undulators. Before describing the experimental setup of the beamline, I will first introduce the RIXS process.

2.1.2. RIXS process

RIXS is a photon-in-photon-out two-step process [63]. In Fig. 2.5 a schematic representation of the process is shown. A photon with energy $\hbar\omega_i$ and momentum $\hbar\vec{k_i}$ impinges on the sample in the ground state (initial state) and it is absorbed. As a consequence, a core electron is excited into the valence band: the system is left with a very unstable intermediate excited state with a deep core hole. Therefore, it decays very rapidly (~ 1 fs): an electron from one valence state decays into the core level emitting a photon (final state). The energy and momentum of the emitted photon are $\hbar\omega_f$ and $\hbar\vec{k_f}$ respectively. The energy of the two photons (incident and outgoing) may be equal, and in this case we talk about Resonant Elastic X-ray scattering (REXS), or different in the case of Resonant Inelastic X-ray scattering (RIXS). In the latter case, the system is left with an excitation, whose energy is the difference of the energies of the two photons and the momentum

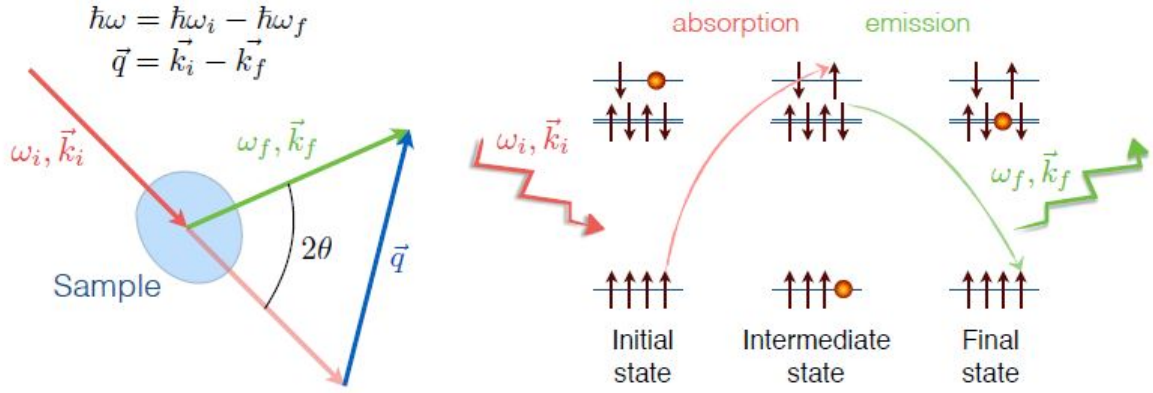

Figure 2.5: *Schematic representation of the RIXS process. A photon with energy $\hbar\omega_i$ and momentum $\hbar\boldsymbol{k}_i$ impinges on the sample and it is absorbed. A core-electron is excited in the valence band and leaves a deep core hole. The system left in an excited state relaxes very rapidly: another electron fills the hole and a photon with energy $\hbar\omega_f$ and momentum $\hbar\boldsymbol{k}_f$ is emitted. An excitation is left in the system with energy $\hbar\omega = \hbar\omega_i - \hbar\omega_f$ and momentum $\hbar\boldsymbol{q} = \hbar\boldsymbol{k}_i - \hbar\boldsymbol{k}_f$. 2θ is the scattering angle. From [9].*

transfer the difference between the momenta.
The energy conservation and momentum conservation rules for the whole system must be obeyed:

$$\hbar\omega = \hbar\omega_i - \hbar\omega_f \tag{2.1}$$

$$\hbar\vec{q} = \hbar\vec{k_i} - \hbar\vec{k_f} \tag{2.2}$$

The energy $\hbar\omega$ and momentum $\hbar\vec{q}$ are the energy and momentum transfer of the excitation. The energy of the incoming photon is fixed to an absorption edge of the sample (resonant mode) and the transferred momentum $\hbar\vec{q}$ is fixed by the scattering geometry, fixing the scattering angle 2θ (see Fig. 2.5). By measuring the energy $\hbar\omega_f$, the energy of the excitation $\hbar\omega$ is obtained.
Let us now have a closer look at the RIXS cross section.

2.1.3. RIXS cross section

In order to find the RIXS cross section, the starting point is writing down the Hamiltonian of the system, representing the radiation and the sample, in particular its electrons. It is therefore composed of three terms: a first term only related to the electrons, a second term referred just to the photons and a third one describing their interaction. This complete Hamiltonian can be considered as a sum of an unperturbed Hamiltonian (made by the

two terms related individually to the radiation and to the sample) and a perturbation term H' corresponding to the interaction.
The probability of the transition W_{if} from the initial ground state $|i>$ of energy E_i (on the left in Fig. 2.5) to the final state $|f>$ of energy E_f (on the right in Fig. 2.5), when treating the electron-photon interaction as a small perturbation within perturbation theory up to second Fermi's Golden rule, takes the form:

$$W_{if} = \frac{2\pi}{\hbar}\left| < f|H'|i > + \sum_n \frac{< f|H'|n >< n|H'|i >}{E_i - E_n}\right|^2 \delta(E_i - E_f) \tag{2.3}$$

where $|n>$ is the intermediate state of energy E_n (at the centre in Fig. 2.5).
Close to resonance, the second term dominates and the first term can be neglected.
The measured quantity, however, is the double-differential scattering cross-section. According to the Fermi's Golden rule (the reader can refer to [64] for the full calculation) it is given by:

$$\frac{d\sigma^2}{d\Omega d\hbar\omega_f} = \frac{\pi e^4}{2\epsilon_0{}^2 c^4}\omega_i\omega_f^3 \sum_f \left| \sum_n \frac{< f|D^\dagger|n >< n|D|g >}{E_g + \hbar\omega_i - E_n + i\Gamma_n}\right|^2 \times \delta(E_f - E_g + \hbar(\omega_f - \omega_i)) \tag{2.4}$$

where $d\Omega$ is the solid angle in which the radiation is scattered and $d\hbar\omega_f$ is the energy resolution and therefore $\frac{d\sigma^2}{d\Omega d\hbar\omega_f}$ is the ratio of photons with energy in the range $\hbar\omega_f - \hbar\omega_f + d\hbar\omega_f$, in the solid angle in the range $\Omega - \Omega + d\Omega$. D is the dipole operator $\boldsymbol{D} = \sum_{i=1}^{N} \boldsymbol{\epsilon} \cdot \mathbf{r_i}$, with ϵ the polarization vector of the incident photon.

Two important features must be highlighted:

- RIXS is a two-step process: upon absorption of a photon, the system is excited to an intermediate state before decaying into the final state through the emission of a photon. Therefore, it allows some transitions, that, if direct, would be dipole forbidden (as in the case of *dd* excitations, that would require transitions within the same shell).
- When $\hbar\omega_i = E_g - E_n$, the scattering cross section increases, since the denominator of summation over n drops (it does not go to zero since there's the imaginary term $i\Gamma_n$). Therefore, the scattering cross section is enhanced by the resonance condition making this technique competitive to neutron scattering, but yet "photon hungry" requiring high-brilliance X-ray sources.

.

2.1.4. RIXS features and limitations

RIXS is characterized by some important features, making it the most suitable technique to be employed in specific cases:

- In the hard X-rays regime the energy and momentum dependece of the excitations can be probed over the entire Brillouin zone. Indeed, the momentum transfer in the RIXS process is:
$$|\mathbf{q}| = \frac{4\pi}{\lambda}\sin(\theta) \tag{2.5}$$
where 2θ is the scattering angle and λ the radiation's wavelength ($\lambda \sim 1$ Å).
- Small sample volumes: X-rays interact with matter much stronger than neutrons. Typical penetration depths for neutrons are in the order of cm, while for hard X-rays with energy of ~ 10 keV the penetration depth is of the order of $\sim 50\mu m$. Therefore, samples analyzed with RIXS can be with small volume with respect to those studied through INS. This can be very useful when only small crystals of the material under investigation can be produced, for instance iridates, that are generally obtained through flux methods.
- Bulk sensitivity: even though the penetration depth of X-rays is smaller than that of neutrons, it still allows bulk sensitivity.
- Chemical and orbital sensitivity: RIXS is a resonant technique. Thus, the energy of the incoming photon is tuned to the resonance edge of a specific element and the properties related to this only specific element can be studied. The energy chosen is not only element specific but it is also orbital specific, i.e. that we can tune the incident energy to different edges (K, L_2, L_3...). Besides, the binding energy is dependent on the valency of the ions. Accordingly, ions of the same element with different valencies can be distinguished (if allowed by energy resolution).
- Polarization sensitivity: one could have information about the transfer of angular momentum and therefore have information about the nature of the created excitations by detecting a change in the polarization between the incoming and outgoing photons. However, a polarimeter is not yet available for hard-X-rays RIXS.

However, RIXS has also some limitations, that were the main reasons for the late develpoment and employment of this technique compared to neutron scattering:

- Energy resolution: the energy resolution of a RIXS experiment is not as good as for a INS experiment, for which fractions of meV can be achieved, allowing to probe and separate very low-energy excitations. For a long time the energy resolution of

a RIXS experiment has been around 1 eV. In the last years a resolution of 25 meV has been reached at the iridium L_3 edge, meaning an incoming photon with energy of 11.215 keV and thus a resolving power of $\sim 4 \times 10^5$ [65, 66]. The quest for a better resolution is still ongoing and very recently quartz analyzers allow an energy resolution of 10 meV resolution [67].

- Efficiency: synchrotron radiation must be employed to carry out experiments in an acceptable amount of time since the cross-section of the process is very low (as discussed in section 2.1.3)

2.1.5. RIXS experimental set-up at ID20

I carried out my thesis project at the ID20 beamline at ESRF. ID20 is committed to the study of the electronic structure of matter, in particular by probing the electronic and magnetic excitations through X-ray inelastic scattering and emission spectroscopy techniques [66]. It is provided by two experimental hutches, one principally dedicated to X-ray Raman Spectroscopy (EH1) and one to RIXS (EH2).
A schematic representation of the optics hutch and RIXS end station in ID20 is reported in Fig. 2.6. The X-ray beam is produced by three undulators in the energy range of hard X-rays (between 4 and 20 keV) and it goes through a sofisticated optical setup before hitting the sample. The first optical element is a collimating mirror, which collimates the beam

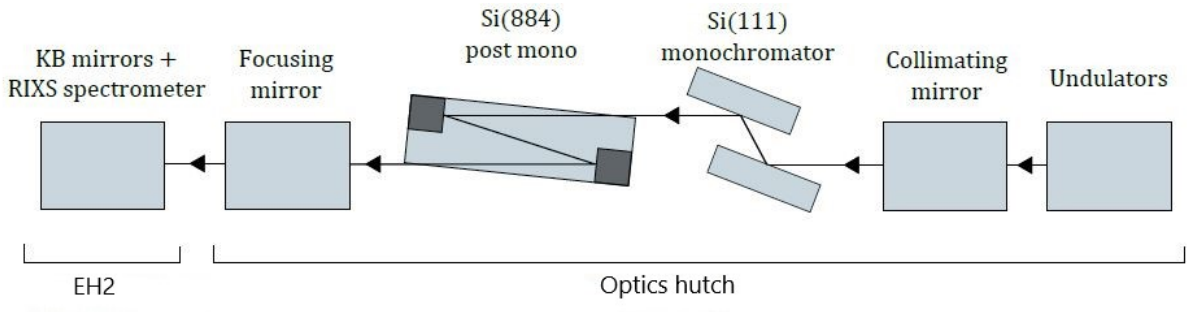

Figure 2.6: *Schematic representation of the setup of the optics hutch and RIXS end station of ID20 at ESRF. X-rays are produced by three undulators and sent to the first collimator. Then the beam passes through a monochromator and a post-monochromator. Finally, two focusing mirrors are present, one in the optics hutch and another (KB mirror) in the experimental hutch (EH2). From [24].*

in the vertical direction in order to match the angular acceptance of the monochromator. The latter is a double-crystal monochromator (DCM) made of two silicon crystals Si(111) exploiting Bragg's law. Post-monochromators are used to reach the desired resolution,

which is typically not achieved using a single monochromator. Finally, two focusing elements are employed: a toroidal mirror in the optics hutch and focusing Kirkpatrick-Baez (KB) mirrors in the experimental hutch (EH2), which allow to reach a spot size on the sample plane of roughly $10 \times 10\ \mu m^2$. All the optical components are kept in ultra-high vacuum ($\sim 10^{-8}$ mbar).
The result is a focused monochromatic beam polarized in the horizontal plane after all the optical component with an energy bandwidth of ~ 14.7 meV.
In a typical RIXS experiment the dispersion of excitations are investigated. Thus the sample is mounted on a goniometer (see Fig. 2.7) which allows the motion of the sample both in terms of rotations (x, y, z) and translations (ω, χ, ϕ).

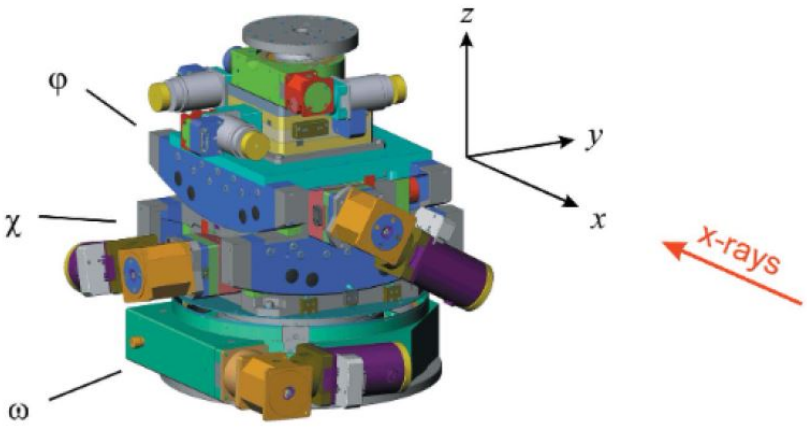

Figure 2.7: *Scheme of the sample tower. χ is the angle of rotation around the x axis, ϕ around the y axis and ω around the z axis [66].*

Using elastic scattering from different non-collinear lattice planes the orientation of the sample's reciprocal space with respect to the laboratory frame of EH2 (x, y, z, χ, ϕ, ω) is determined prior to the RIXS experiments. This information is contained in the so called orientation matrix, or UB matrix [68]. The U matrix tells how the sample is mounted in the laboratory coordinate system. The B matrix links the reciprocal space of the sample to its real space, mapping every point of the reciprocal space into a coordinate system rooted in the crystal. When the two matrices are known, one can calculate the angles of the sample and of the spectrometer arm for every momentum transfer.
A cryostat is used to perform experiments at low temperature (a minimum temperature of ~ 4 K can be reached) using liquid helium [69].
The measure of the energy and the momentum of photons scattered by the sample is of fundamental importance in a RIXS experiment. A spectrometer is employed for this purpose. Fig. 2.8 is a schematic representation of the spectrometer employed at ID20.

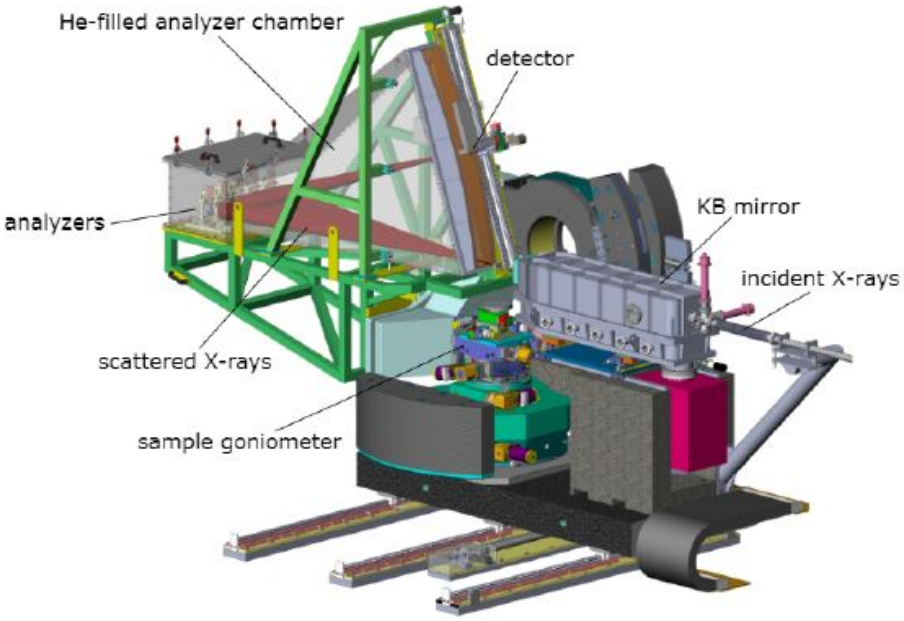

Figure 2.8: *Schematic representation of the RIXS spectrometer employed at ID20. The sample is mounted on a tower, while the scattering arm contains crystal analyzers hosted in a He-filled chamber and a 2D-detector. From [66].*

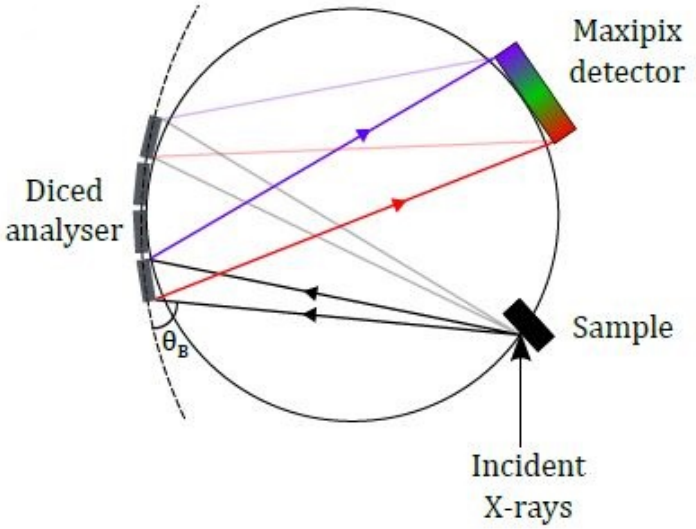

Figure 2.9: *Rowland geometry representation. The sample, the diced analyzer and the detector lie on the same circumference. The analyzers are diced and they have a curvature of the same radius of the Rowland circumference. θ_B is the Bragg angle. From [24].*

It is made up by five crystal analyzers, hosted in He-filled chamber to reduce detrimental effects due to the presence of air, and a 2D detector. It operates in a Rowland geometry:

the sample, the detector and each analyzer lie on the same circumference (of diameter R = 2 m in the specific case of ID20 spectrometer) as shown in Fig. 2.9. The analyzers are Si(844) crystals which obey Bragg's law. The crystals are bent to a curvature radius equal to the Rowland circle diameter so that X-rays are focused on the detector. In this way the same component (the crystal analyzer) acts as energy analyzer and as focusing element. Diced crystal analyzers are used instead of bent crystals in order to avoid strain which would deteriorate the energy resolution (typically a matrix of the order of 10^4 small cubes are used). The analyzer Bragg angle changes for different points on the dices, which are flat and therefore dispersive, resulting in an energy dispersion on the detector surface. The detector at ID20 is a 2D position-sensitive detector [70]. Therefore, this energy dispersion can be compensated for. Different Bragg angles must be swept in order to obtain a complete energy loss spectrum. This is done by moving the relative orientation of the detector and the analyser, while the sample is conveniently kept fixed.
The spectrometer is not able to determine infinitesimally small differences in energy. This is the concept of resolution. Different elements concur to worsen the energy resolution (details in [66]). An important limiting factor is the finite size of the pixels of the detector (typically $\sim 55\mu m \times 55\mu m$) since it is not possible to distinguish different energies of photons arriving at same pixel. Another contribution comes from the crystal analyzer, which is characterized by an intrinsic energy resolution and the so called Johann aberration. Finally, the finite source size of the beam must be considered. Considering all the contributions the overall energy resolution of the beamline and of the spectrometer is around 25 meV at the L_3 iridium edge (11.215 keV).

2.2. Experimental techniques to characterize the sample

Experiments to characterize the sample are often performed prior to a RIXS experiment, for instance in order to know about the sample's stoichiometry, the sample's orientation, or possible phase transitions through macroscopic measurements. In this context, we performed Energy-dispersive-X-Ray spectroscopy (EDX), magnetometry and resistivity measurements. Those techniques are briefly exposed below.

2.2.1. Energy-dispersive-X-Ray spectroscopy (EDX)

Energy-dispersive-X-Ray spectroscopy (EDX) is a technique to characterize the chemical composition of samples. It consists of sending an electron beam to the sample in order

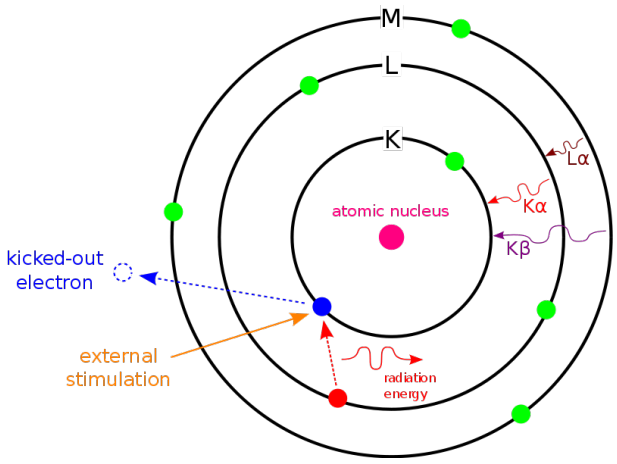

Figure 2.10: *Schematic representation of EDX process. An electron is sent to the sample and it ejects a core-electron. Another electron from a higher-energy level fills the hole and a photon is emitted. Its energy is equal to the difference in energy between the two levels. From [71].*

to excite a core-electron. The latter is ejected and the system is left in an excited state. Another electron from a higher-energy level fills the hole in the inner shell emitting a photon with energy equal to the difference between the energies of the two states. The process is schematically reported in Fig. 2.10. The emission spectrum obtained through an energy-dispersive detector is characterized by many peaks at different energies and intensities. The energy of the emitted photon (and the corresponding peak in the spectrum) is characteristic of a specific element. A qualitative analysis is done by comparing the energy of the peaks in the spectrum with known energy values characteristic of the different elements. Thus, it allows to determine which elements are present in the sample. A quantitative analysis can be done considering the intensities of the X-ray peaks in the spectrum, which are proportional to the elements abundance, thus the chemical composition can be estimated.

2.2.2. Resistivity measurements

Resistivity measurements are macroscopic measurements typically performed to characterize samples, in particular to determine electrical properties. The technique that is commonly used is the four-point probe technique. It involves four equally-spaced and co-linear probes, which are in contact with the material under study, as represented in Fig. 2.11. A DC current is sent between the outer two probes and a voltage drop is measured between the inner ones. The resistivity is then obtained from the voltage drop

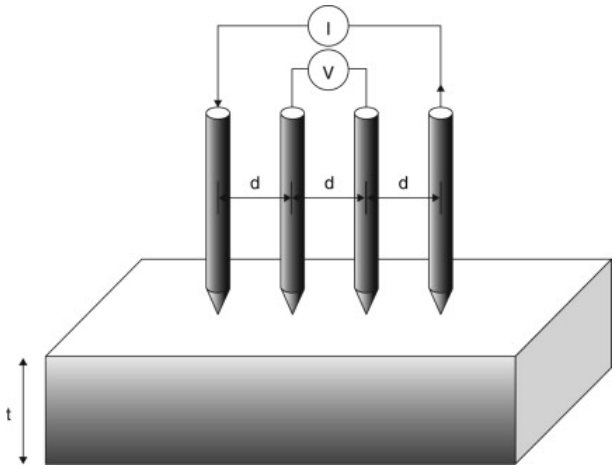

Figure 2.11: *Four probe method for the resistivity measurement of a sample. Four equally-spaced and co-linear probes are in contact with the sample. A current is sent between the outer probes and a voltage is measured between the inner ones. From geometric factors, the measurements of the voltage drop and the current sent, one can measure the resistivity. From [72].*

measurements, the current injected and geometric factors:

$$\rho = 2\pi d \frac{V}{I} \tag{2.6}$$

where d is the distance between the contact points, V the measured voltage drop and I the electrical current forced.

2.2.3. SQUID magnetometer

The SQUID (Superconducting Quantum Interference Devices) magnetometer is an instrument to investigate the magnetic properties of materials in a precise way [73].
SQUID magnetometers are based on the Josephson effect. It consists in the flow of a current between two superconducting layers separated by a weak link (either just non-superconducting or insulating). A voltage drop sets in when the flowing current is higher than a certain critical value I_C, as can be observed from the characteristic current-voltage drop curve reported in Fig. 2.12a. This device is called Josephson junction.
A SQUID is a a ring made by superconducting material and two Josephson junctions in parallel as shown in Fig. 2.12b. If a current higher than the critical one is set in the ring, the presence of an external magnetic flied will induce a change in the voltage drop across the junction. More precisely, the voltage drop will change as a periodic function of the magnetic flux across the ring, with a period of a quantum flux

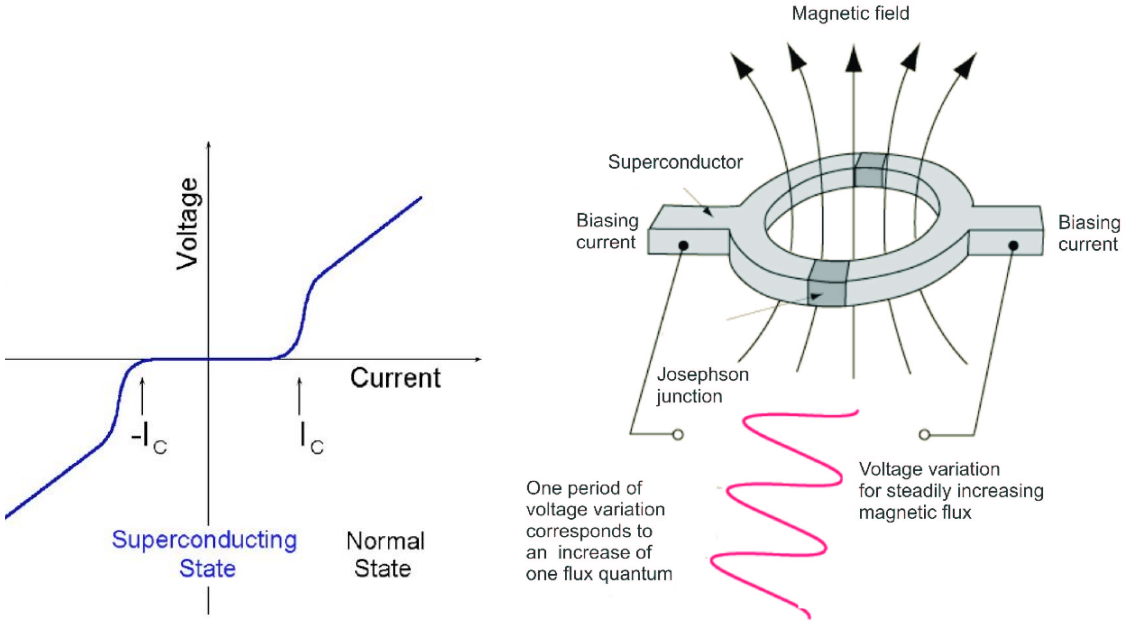

(a) (b)

Figure 2.12: *(a) Characteristic current-voltage drop curve for a Josephson junction. The voltage drop across the junction is zero when the current is smaller than a critical value I_C. Above this current, a voltage drop sets in. From [74]. (b) Schematic representation of a SQUID ring. It is made by two Josephson junctions in parallel and a superconductive material. The voltage drop across the junction is a periodic function of the magnetic flux inside the ring (if the current flowing is higher than the critical current). From [75].*

$\phi_0 = h/2e = 2.067833848... \times 10^{15} Wb$. This allows to measure magnetic fluxes and therefore magnetic properties of compounds in an extremely precise way.
Typical measurements performed with SQUID magnetometers allow to obtain the magnetization's dependence on the magnetic field (eventually one could observe an hysteresis loop) and also the magnetization's dependence on temperature. In the latter case the ZFC-FC procedure is followed: the temperature dependence of the magnetization is probed without (ZFC) and with (FC) applied magnetic field. The two curves are superimposed and bifurcations between the two generally indicate magnetic phase transitions. This technique allows to probe magnetic phase transitions in a quite accurate and precise way.

2.3. Modelization of magnetic excitations

The experimental data of magnetic excitations can be compared with numerical calculations in order to quantify the magnetic interactions in the system under study. To do so, we have used the SpinW software [76]. Before entering into the details of this program, I will briefly introduce the concept of spin waves.

2.3.1. Spin waves in a linear chain of atoms

An analitical expression of the spin wave dispersion relation can be obtained for a 1D linear chain of magnetic moments interacting only through the Heseinberg exchange (both ferromagnetically and antiferromagnetically).
At zero temperature the ground state of the Heisenberg Hamiltonian is represented by all spins aligned either parallel or antiparallel. The order is disrupted by the flipping of some spins at temperature different from zero. Single magnetic moments cannot oscillate independently from those of their neighbours since they interact with each other. The simplest form of motion of magnetic moments is a wave: this spin flip is distributed along the whole solid, as represented in Fig. 2.13a for a ferromagnetic chain of magnetic moments. For a ferromagnetic chain of spins ($S = S_z$, $S_x = S_y = 0$) the expression of the

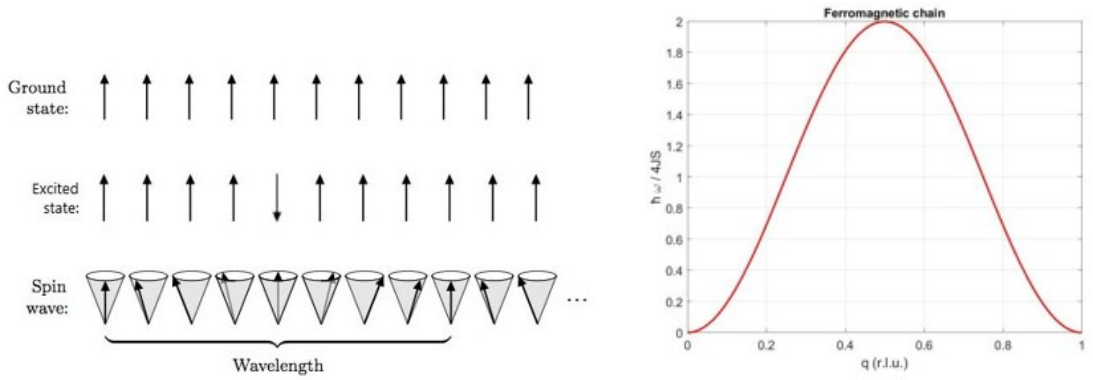

(a) (b)

Figure 2.13: *(a) Schematic representation of spin waves propagating in a 1D ferromagnetic chain of magnetic moments. (b) Spin wave dispersion relation for a ferromagnetic linear chain of magnetic moments.*

dispersion relation is:

$$\hbar\omega = 4JS[1 - cos(qa)] \tag{2.7}$$

with J the Heisenberg exchange and a the lattice constant. It is shown in Fig. 2.13b.
For spin waves propagating in an antiferromagnetic chain (see Fig. 2.14a) the dispersion

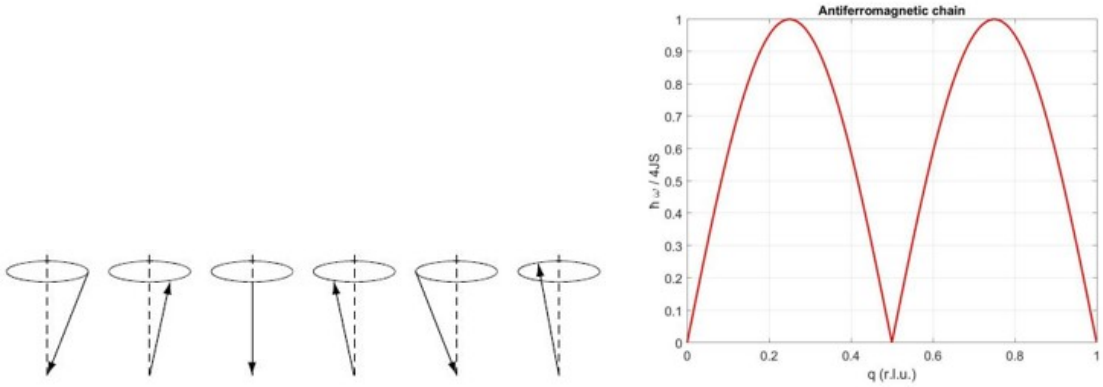

(a) (b)

Figure 2.14: *(a) Spin wave propagation in a linear antiferromagnetic chain of magnetic moments. (b) Spin wave dispersion relation for a linear antiferromagnetic chain of spins.*

relation has the expression:

$$\hbar\omega = 4|J|S|sin(qa)| \tag{2.8}$$

and it is shown in Fig. 2.14b.
In order to model the magnetic spectra of our experiment, we employed the SpinW software that is based on a linear spin wave description.

2.3.2. Numerical simulations with SpinW

Numerical simulations are often necessary in the case of more complex interactions and 3D crystal structure. SpinW is a Matlab library dedicated to the numerical simulation of magnetic excitations for a given Hamiltonian using linear spin wave theory.
It is based on a localized-magnetic-moments description. The Hamiltonian that can be defined with SpinW takes into account the Heisenberg exchange, the Dzyaloshinskii-Morya interaction, an anisotropic interaction and a Zeeman term in the case of presence of an external magnetic field:

$$H = \sum_{i,j} \mathbf{S}_i{}^T \cdot J_{ij} \cdot \mathbf{S}_j + \sum_{i,j} \mathbf{D}_{i,j} \cdot (\mathbf{S}_i \times \mathbf{S}_j) + \sum_{i,j} \mathbf{S}_i{}^T \cdot \Gamma_{ij} \cdot \mathbf{S}_j + \mathbf{B} \cdot \sum_i g_i \mathbf{S}_i \tag{2.9}$$

where S_i are spin operators, J_{ij} exchange tensors, $\Gamma_{i,j}$ anisotropic tensors, $\mathbf{D}_{i,j}$ the Dzyaloshinskii-Morya vector, $\mathbf{B}$ an external field and g_i the g-tensor.
The calculated magnon dispersion relation of the crystal of interested can be obtained

and compared with the experimental one. Consequently, one can quantify the magnetic interactions.

It is important to highlight a basic approximation that is done when comparing the SpinW simulations with RIXS experimental data. The scattering cross section calculated is the one corresponding to the dynamical structure factor $S(\mathbf{q},\omega)$ which contains information about the dynamics of the system. For neutrons $S(\mathbf{q},\omega)$ is proportional to the imaginary part of the dynamic magnetic susceptibility $\chi(\mathbf{q},\omega)$ which describes the response of the system to small magnetic fields $H(\mathbf{q},\omega)$. This is not valid for X-rays at resonance, for which a more complex expression of the dynamic structure factor should be considered. Nevertheless, we will use this model as a first approach to model our data.

3 | Study of $Tb_{2+x}Ir_{2-x}O_{7-y}$ by RIXS

The present work is focused on the study of $Tb_2Ir_2O_7$. Terbium is placed at the center of the phase diagram in Fig. 1.19a in the region of transition between the metallic and non-metallic state. Thus, a Weyl semimetal phase could be realized.
We have first carried out experiments to characterize a single crystal of $Tb_2Ir_2O_7$ and then study the excitations of this system through the RIXS technique on ID20.

3.1. Sample growth

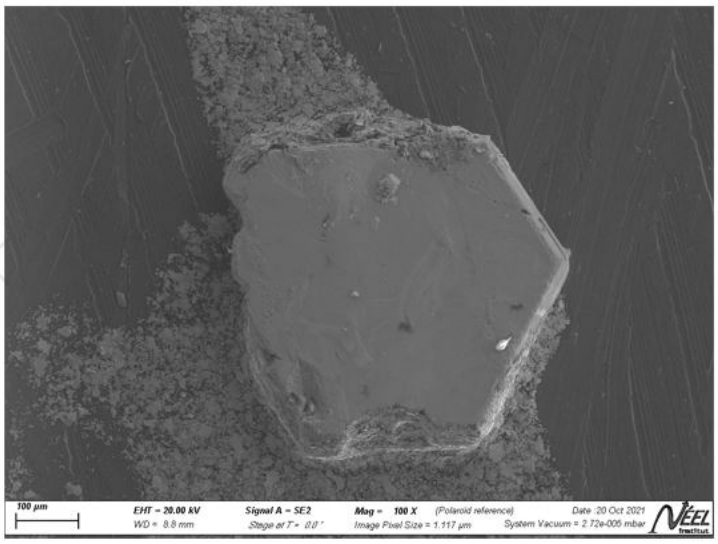

Figure 3.1: *Single crystal of $Tb_2Ir_2O_7$ seen in the plane perpendicular to the [111] direction. It was grown with the flux growth method by Dr. Dharmalingam Prabhakaran at the University of Oxford.*

Fig. 3.1 shows the single crystal of $Tb_2Ir_2O_7$ under study in the plane perpendicular to the [111] direction. The sample, with dimensions roughly of 300 μm $\times$ 300 μm $\times$ 100 μm, was grown by Dr. Dharmalingam Prabhakaran at the University of Oxford with the flux

growth method [9, 77].
This method does not allow to obtain large samples. Moreover, variations of the stoichiometry from the ideal one are common in the synthesis of single crystal pyrochlore oxides using this technique and they can have a great impact on the properties of the crystals. In particular, it is frequent to have a degree of so-called *stuffing*. Stuffing is the excess of the rare-earth ions which substitute iridium ions, since iridium is highly volatile. Therefore, the stoichiometry becomes $R_{2+x}Ir_{2-x}O_{7-y}$. Donnerer et al. [78] found a stuffing of $x \sim 0.18$ in $Tb_{2+x}Ir_{2-x}O_{7-y}$. On the contrary, powder samples typically retain the ideal composition.

Therefore, we study the sample composition with EDX measurements performed at the Néel Institute.

3.2. EDX measurements to study the chemical composition

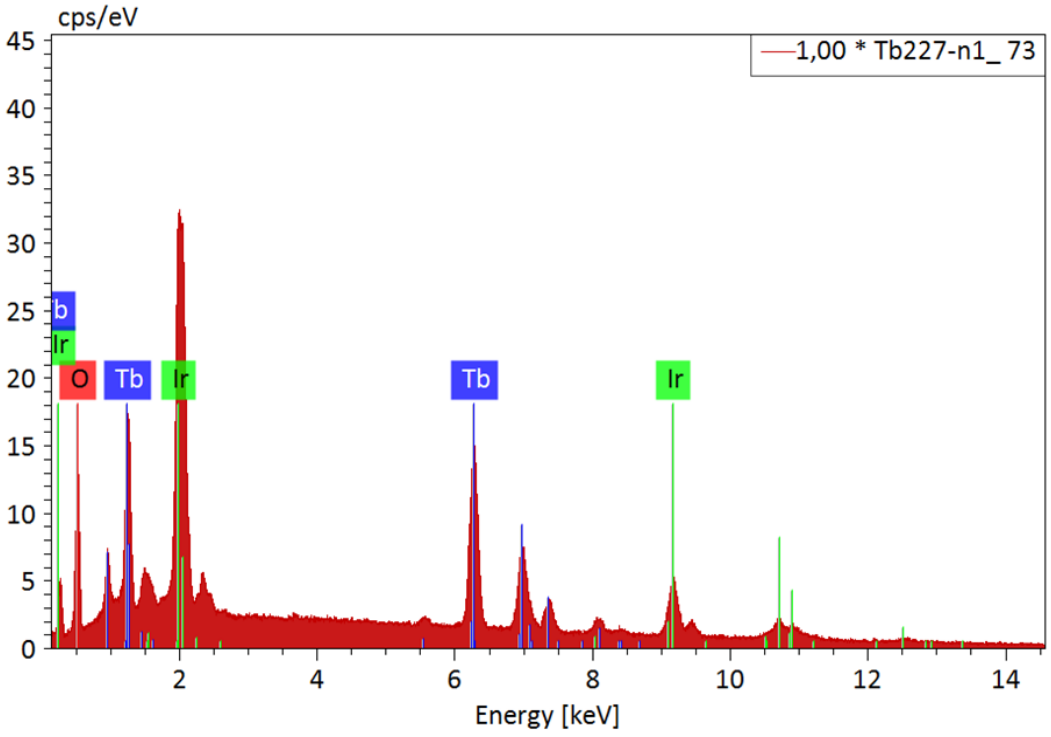

Figure 3.2: *EDX spectrum of $Tb_2Ir_2O_7$ single crystal (counts per seconds per electron volts, cps/eV, on the y-axis). We have performed the measurements at Néel Institute, Grenoble (France).*

Fig. 3.2 shows the EDX spectrum of the sample. Characteristic peaks of different elements

Element	At. No.	Line s.	Mass [%]	Mass Norm. [%]	Atom [%]	Abs. err. [%] (1 sigma)	Rel. err. [%] (1 sigma)
Oxygen	8	K-Serie	10.40	15.29	66.01	1.34	12.87
Terbium	65	L-Serie	32.01	47.06	20.46	0.88	2.74
Iridium	77	L-Serie	25.61	37.65	13.53	0.76	2.95

Figure 3.3: *Table from EDX measurements. The mass, normalized mass and atomic concentrations of oxygen, terbium and iridium in the sample of $Tb_{2+x}Ir_{2-x}O_{7-y}$ are reported together with the absolute and relative errors of the atomic concentrations.*

are identified by a software and from their intensities the stoichiometry of the sample is estimated. The table in Fig. 3.3 shows the estimated concentration (in terms of mass and atomic concentrations) of the elements in the sample and the absolute and relative errors. An excess of terbium and a lack of iridium are found indicating a finite degree of stuffing. The stoichiometry of the sample is $Tb_{2+x}Ir_{2-x}O_{7-y}$ with x $\sim$ 0.4. The oxygen concentration is difficult to be quantified with the EDX technique, which is not suitable to detect light elements.

Different studies have been addressed to understand the effects of substitution of iridium with other ions in pyrochlore iridates, in particular in terms of the interplay between the spin-orbit coupling and the electronic correlations [79, 80]. Kumar et al. [80] studied the evolution of structure, magnetic and electronic properties in polycrystalline $Y_2Ir_{2-x}Ru_{2+x}O_7$ in which Ru substitute Ir ions. They found that the compound remains insulating at all temperatures for samples with different substitution values (up to x = 0.4) but the resistivity decreases with the Ru substitution, as shown in Fig. 3.4.

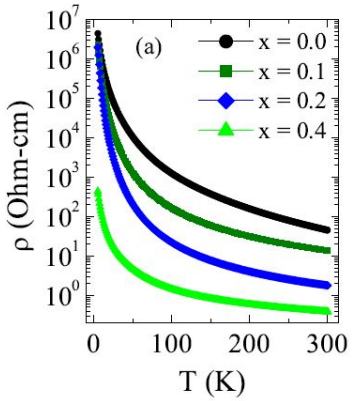

Figure 3.4: *Temperature dependence of the resistivity in $Y_2Ir_{2-x}Ru_{2+x}O_7$ for different values of x = 0.0, 0.1, 0.2, 0.4. From [80].*

In single crystal pyrochlore iridates the substitution of iridium with rare-earth ions, i.e

stuffing, comes naturally from the growth process and it has been considered initially as an experimental nuisance. Donnerer et al. [78] show that, as a consequence of the stuffing in $Tb_{2+x}Ir_{2-x}O_{7-y}$ with $x \sim 0.18$, the magnetic transition temperature lowers from the ideal 130 K to roughly 70 K and the resistivity measurements show that the sample is much more metallic than ideally stoichiometric ones (about 2-3 orders of magnitude). Moreover, they also show that the AIAO magnetic structure is robust against stuffing. This is of crucial importance since stuffing could lead towards the realization of the Weyl semimetallic phase in pyrochlores: it preserves the AIAO magnetic structure and lowers electronic correlations.

Therefore, we study the sample resistivity and magnetic properties to analyze the effects of stuffing.

3.3. Resistivity and magnetometry measurements of $Tb_{2+x}Ir_{2-x}O_{7-y}$

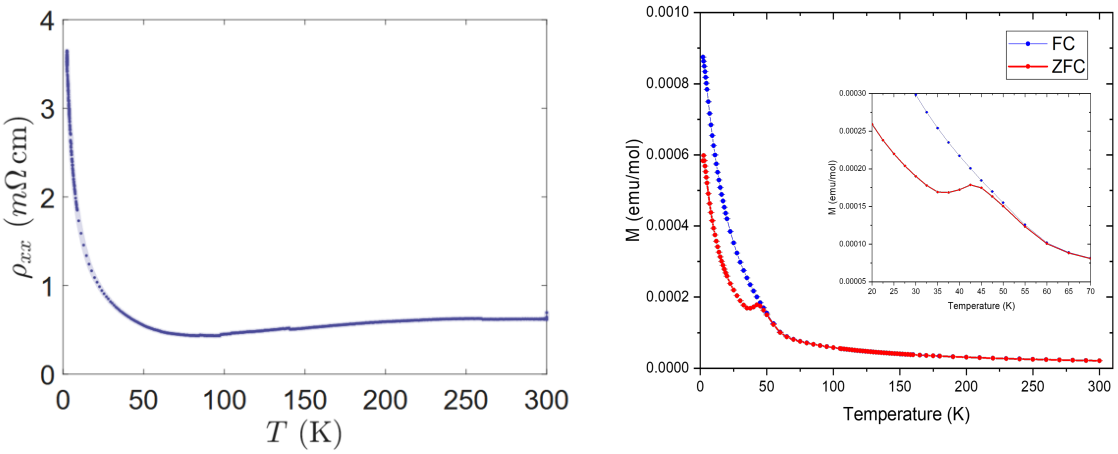

(a) (b)

Figure 3.5: *(a) Resistivity measurements as a function of temperature. The measurement has been realized with the four probe method by Jian-Rui SOH at the École Polytechnique Fédérale de Lausanne (EPFL) (b) Field cooled (FC), with magnetic field of 100 Oe and zero field cooled (ZFC) magnetization measurements as a function of temperature. We have realized it with a SQUID magnetometer at Néel institute, Grenoble (France).*

Fig. 3.5a shows the resistivity measurements of the sample as a function of temperature. One can observe that there is a transition from an insulating behaviour to a metallic state

(MIT) for a temperature of approximately T = 50 K. Moreover, the resistivity is much lower (by $\sim$ 3 orders of magnitude) than for polycrystalline samples (see Fig. 1.19b), in accordance to what was observed for previous stuffed $Tb_{2+x}Ir_{2-x}O_{7-y}$ [78].
Fig. 3.5b shows magnetic measurements realized with a SQUID magnetometer. The bifurcation between the ZFC and FC curves for $T \sim 50K$ indicates magnetic ordering. From previous works [78], it is assumed that it corresponds to a AIAO magnetic structure at the iridium site.

These results are compatible with the realization of the Weyl semimetal phase, since the AIAO configuration breaks time reversal symmetry and the sample is much more metallic than ideally stoichiometric pyrochlore iridates. Thus, once the sample has been characterized, we performed RIXS measurements to study its dynamics and have an insight into how stuffing changes the interplay between SOC and electronic correlations.

3.4. RIXS spectra of low energy excitations

We have performed RIXS experiments at the ESRF on ID20. The RIXS technique and experimental set-up at ID20 have been described in chapter 2.
The sample has been mounted on the holder with [1 1 1] as specular reflection and the [1

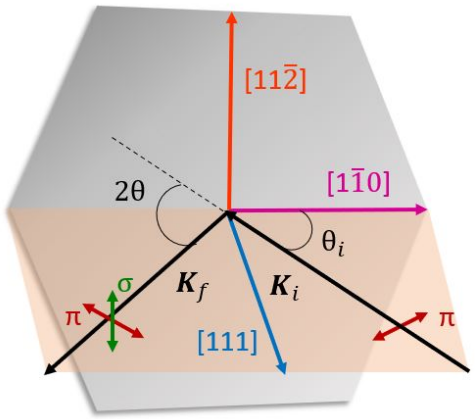

Figure 3.6: *RIXS scattering geometry for a single crystal pyrochlore iridate. The incident photon has a wave vector $\boldsymbol{k}_i$ and linear polarization parallel to the horizonatl scattering plane (π). The outgoing photon has wave vector $\boldsymbol{k}_f$ and can have π or σ polarization. The scattering angle 2θ is the angle between $\boldsymbol{k}_i$ and $\boldsymbol{k}_f$. The [1 1 1] direction is the specular reflection. The [1 $\bar{1}$ 0] and [1 1 $\bar{2}$] directions are in plane.*

$\bar{1}$ 0] and [1 1 $\bar{2}$] directions in plane (see Fig. 3.6). The polarization of the incident X-ray beam is linear and in the horizontal scattering plane. The scattering geometry employed

is the horizontal one [66].

Before measuring high-resolution RIXS spectra, we have acquired an intensity map showing the incident energy dependence of the RIXS features, reported in Fig. 3.7. It has been performed using a Si(311) channel cut post-monochromator, resulting in an overall energy resolution of $\sim$ 350 meV.
One can notice a feature around zero energy loss, another one below an energy transfer of 2 eV and a broad intensity feature around 4 eV.

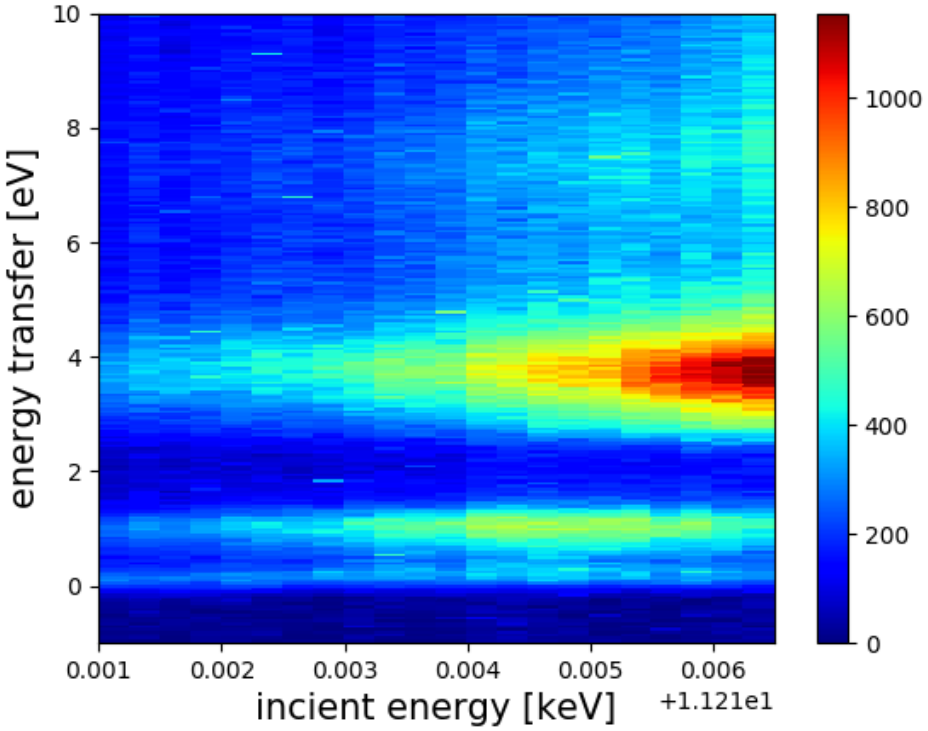

Figure 3.7: *Incident-photon-energy-dependence of the RIXS spectral features. From literature [81], the feature around zero energy loss is expected to contain the elastic contribution and the magnetic contribution, the feature below 2 eV energy loss is given by intra-t_{2g} transitions while the broad feature around 4 eV represents t_{2g} to e_g transitions.*

From literature [81], the feature around zero energy loss is expected to contain the elastic contribution and the magnetic contribution, the feature below 2 eV energy loss is given by intra-t_{2g} transitions while the broad feature around 4 eV represents t_{2g} to e_g transitions. The energy of the features remains fixed when changing the incident energy but their intensity changes. Two resonances are observed: the intra-t_{2g} peak resonates at 11.215 keV, corresponding to the onset of the iridium L_3 edge, while the t_{2g} to e_g peak resonates

at higher energy. Since the interest of the present work is on excitations within the t_{2g} manifold, in particular magnetic excitations, the incident energy has been set to 11.215 keV for the whole experiment.

For different momentum transfers an energy spectrum is acquired. The spectra were acquired in the Brillouin zone around $\mathbf{Q} = (7, 7, 7)$ in order to minimize the elastic contribution, indeed in this case the scattering angle 2θ is close to 90° and the elastic scattering cross section is minimized, due to the polarization dependence of the Thomson scattering cross section.

3.4.1. intra-t_{2g} *dd* excitations

Fig. 3.8 shows an energy scan up to 2 $\sim$ eV measured at $\mathbf{Q} = (7.5, 7.5, 7.5)$ at T = 20 K.

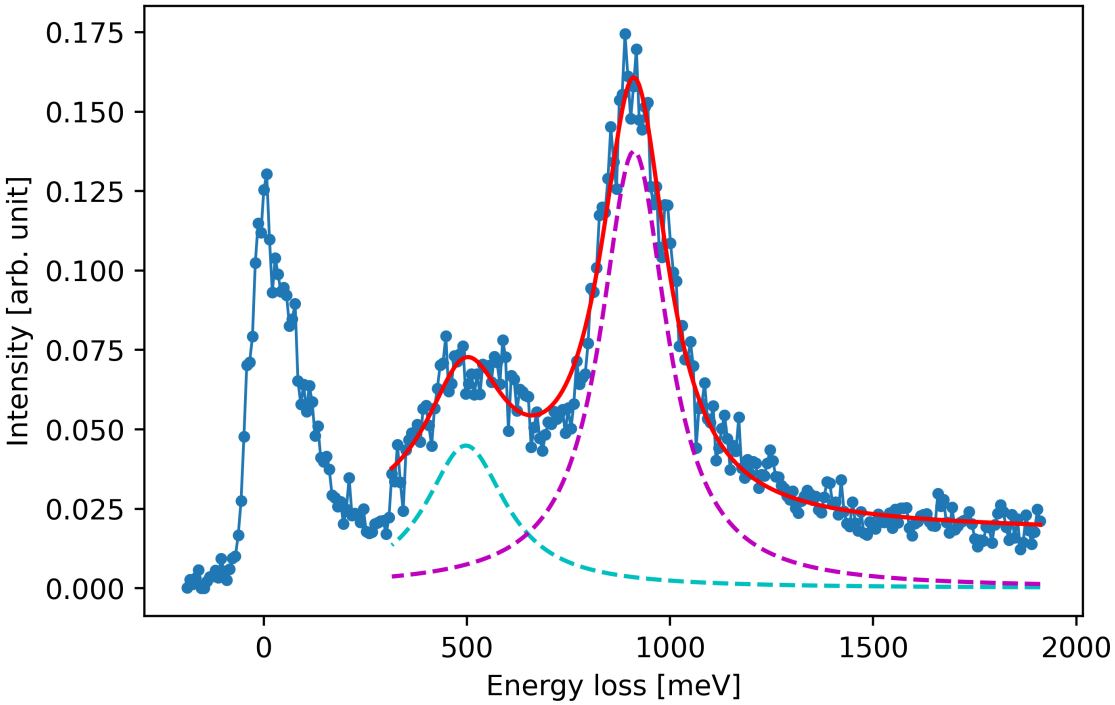

Figure 3.8: *RIXS spectrum at T = 20 K for an energy loss below 2 eV. At low energies a complex intensity profile is present. At higher energies two peaks are present. They have been fitted with two Lorentzian functions and their energies are 497 meV (blue fitting function) and 911 meV (purple fitting function). The red curve represents the fitting of the data in the energy range above $\sim$ 400 meV.*

A complex intensity profile is present at low energy transfer below $\sim$ 400 meV. Instead, two broad features can be clearly distinguished at higher energy loss. They correspond to the broad feature in the intensity map of Fig. 3.7 and from literature [82] they are attributed to intra-t_{2g} *dd* excitations. They are fitted with two Lorentzian functions (see Fig. 3.8). Their energies are 497 meV (light blue fitting function) and 911 meV (purple fitting function).
In chapter 1 it has been shown that for a perfect octahedral environment a $J_{\text{eff}} = 1/2$ state is realized. Four electrons place in the $J_{\text{eff}} = 3/2$ state and one in the $J_{\text{eff}} = 1/2$ level leaving a hole in the latter. Therefore, a single peak is expected in terms of intra-t_{2g} *dd* excitations.
However, a trigonal compression (along the [111] direction) of the octhaedra (see Fig. 3.9) is reported for many iridates [81, 82].

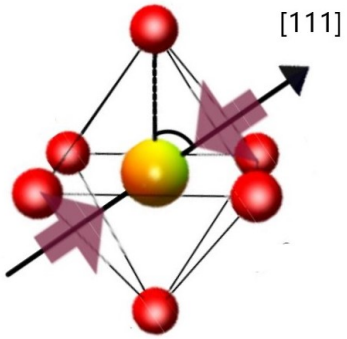

Figure 3.9: *Trigonal distortion of the octahedron around Ir ions. The octahedron is compressed along the [111] direction. The Ir-O-Ir angle decreases and the t_{2g} states are splitted into three doublets.*

The trigonal distortion changes the bonding angle Ir-O-Ir from the ideal one of $\sim$ 141°, while preserving the global cubic symmetry, and further splits the t_{2g} states. Thus, the $J_{\text{eff}} = 1/2$ picture is disrupted.
An empirical model [82, 83] which describes the splitting of the t_{2g} states due to the SOC coupling and trigonal field is the following:

$$H = \lambda \mathbf{l} \cdot \mathbf{s} - \Delta {l_z}^2 \tag{3.1}$$

where λ is the SOC constant, Δ the trigonal field splitting. The z axis corresponds to the [111] direction. The eigenvalues of this Hamiltonian are three doublets with energies:

$$E_{0,2} = \frac{\lambda}{4}(-1 + \delta \mp \sqrt{9 + 2\delta + \delta^2}), \quad E_1 = \frac{\lambda}{2} \tag{3.2}$$

where $\delta = 2\Delta/\lambda$ and E_0 is the ground state energy.
The energies of the two peaks found in the spectrum correspond to E_1-E_0 and E_2-E_0. Hozoi et al. [82] show the calculations to estimate the values of λ and Δ from the energies of the *dd* exitations. The values found here are: $\lambda = 0.399$ eV and $\Delta = 0.516$ eV.

In order to quantify magnetic interactions and get an insight on electronic correlations, we measured the dispersion of magnetic excitations and compared it with numerical simulations based on a localized description of the magnetic moments. If the experimental data follow precisely the simulation, the system can be considered in a strong correlation regime. On the contrary, if some discrepancies are found a more itinerant description, i.e weaker correlations, may be more adequate.

3.4.2. Magnetic excitations

Fig. 3.10 shows the RIXS spectra acquired at T = 10 K along the high-symmetry crystallographic directions: ΓX, ΓK, ΓL, XW and WL (see Fig. 1.15b).

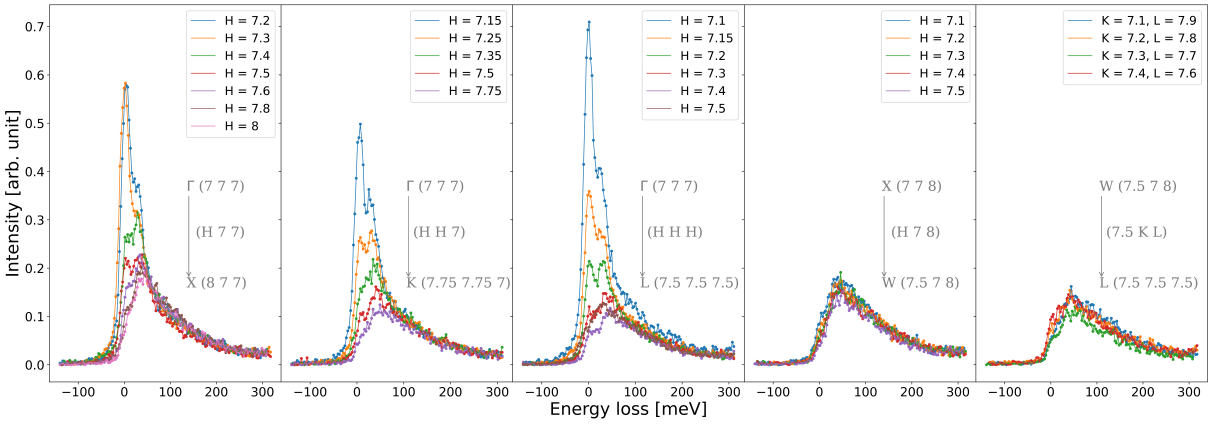

Figure 3.10: *RIXS spectra at 10 K along different crystallographic directions* ΓX, ΓK, ΓL, XW *and* WL.

They are very similar to the spectra found for single crystals of $Sm_2Ir_2O_7$ and $Eu_2Ir_2O_7$ [53, 54]. In both papers they identified three features in each spectra: the elastic peak at zero energy loss (feature A), while for a finite energy loss two features B and C are observed. The inelastic peak at lower energy transfer has been attributed to a magnetic excitation (feature B), indeed Chun et al. [53] show a temperature dependence of the latter. On the contrary, the origin of the other inelastic feature at higher energy (feature C) is still not clear. It has been suggested it could be related to a particle-hole continuum [53, 54]. Moreover, they show that it does not disperse as a function of momentum

transfer within the energy resolution and it is independent of temperature.
It is necessary to fit the spectra to determine precisely the energy of the magnetic excitations. We chose the fitting function as from literature [53, 54]:

$$I = I_A + I_B + I_C \tag{3.3}$$

$$I_A = A\frac{\gamma^{2m}}{[\gamma^2 + (2^{1/\mathrm{m}} - 1)(\omega - \omega_0)^2]^{\mathrm{m}}} \tag{3.4}$$

$$I_B, I_C = \frac{A}{1 - exp(-\omega/T)}\left(\frac{\gamma}{\gamma^2 + (\omega - \omega_0)^2} - \frac{\gamma}{\gamma^2 + (\omega + \omega_0)^2}\right) \tag{3.5}$$

I_A is the Pearson VII function: it is a symmetric function whose full width at half maximum (FWHM) is given by the parameter γ, its position by ω_0 and overall amplitude by A. I_B and I_C represent the damped harmonic oscillator function: it is an antisymmetric function whose width is related to the parameter γ, the position to ω_0 and the overall amplitude to A.

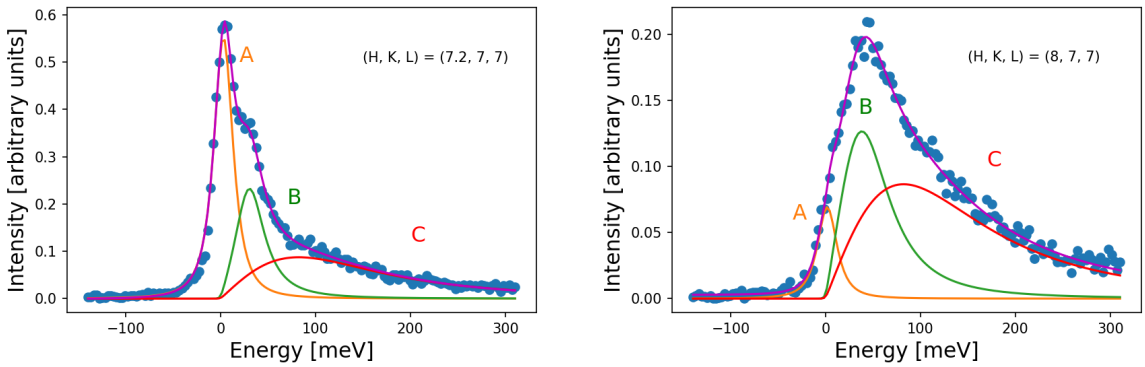

Figure 3.11: *RIXS spectrum at T = 10 K for $Tb_{2+x}Ir_{2-x}O_{7-y}$ $x \sim 0.4$ at (a) $\boldsymbol{Q}$ = (7.2, 7, 7) and (b) $\boldsymbol{Q}$ = (8, 7, 7). The blue dots are the experimental data, the purple curve the total fitting curve, the orange peak is the elastic contribution fitted by a Pearson VII function, the green feature represents the magnetic excitation fitted by a damped harmonic oscillator and the red feature is the C feature also fitted by a damped harmonic oscillator (see eq. 3.4, 3.5)*

Fig. 3.11a and Fig. 3.11b show the fit for **Q** = (7.2, 7, 7) and **Q** = (8, 7, 7) at T = 10 K. The data are represented by blue dots. The purple curve is the total fitting function given by the sum of three terms: the orange peak represents the elastic contribution and

it is a Pearson VII function, the green feature is the magnetic excitation fitted with a damped harmonic oscillator function and the red one represents the C feature, also fitted by a damped harmonic oscillator function. In Appendix A Fig. A.1 shows all the acquired spectra with their respective best least-square fits.

Fig. 3.12a and 3.12b represent respectively the fit of the magnetic excitations and C fea-

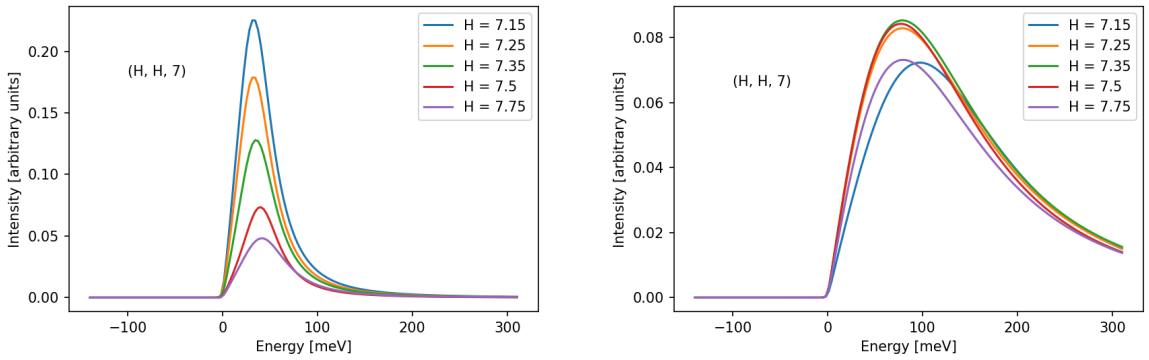

(a) (b)

Figure 3.12: *(a) Fit of the magnetic excitations in the spectra along the* $\Gamma(7,7,7)K(7.75,7.75,7)$ *direction. The magnon has been fitted with the damped harmonic oscillator function in equation 3.5. (b) C feature in the spectra along the* $\Gamma(7,7,7)K(7.75,7.75,7)$ *direction. It has been fitted with the damped harmonic oscillator function in equation 3.5.*

tures along the ΓK direction. One can notice that the intensity of the magnon decreases moving away from the Γ point and it disperses in energy. The C feature instead remains essentially unchanged for different points in the reciprocal space in agreement with what found in previous works (see Fig. 3.12b).

During all fits, the width of all the features was constrained to be greater than 25 meV to take into account the energy resolution. Fig. 3.13 shows the width of the magnon obtained from the fit (γ from equation 3.5) along the high-symmetry crystallographic directions. The error bars are extracted from the fit, providing the covariance matrix, whose diagonal contains the variance of the paramaters of the fit.

The magnon energy extracted from the fits are represented in Fig. 3.14 as black dots on top of the intensity map. The latter represents the intensity of the magnetic excitation (the intensity of the elastic peak and of the C feature have been subtracted for more clarity).

The spin gap is expected to be of the order of 100 meV and the dispersion width roughly 15 meV from RPA calculations [55]. We have found a band gap of roughly 27 meV and a

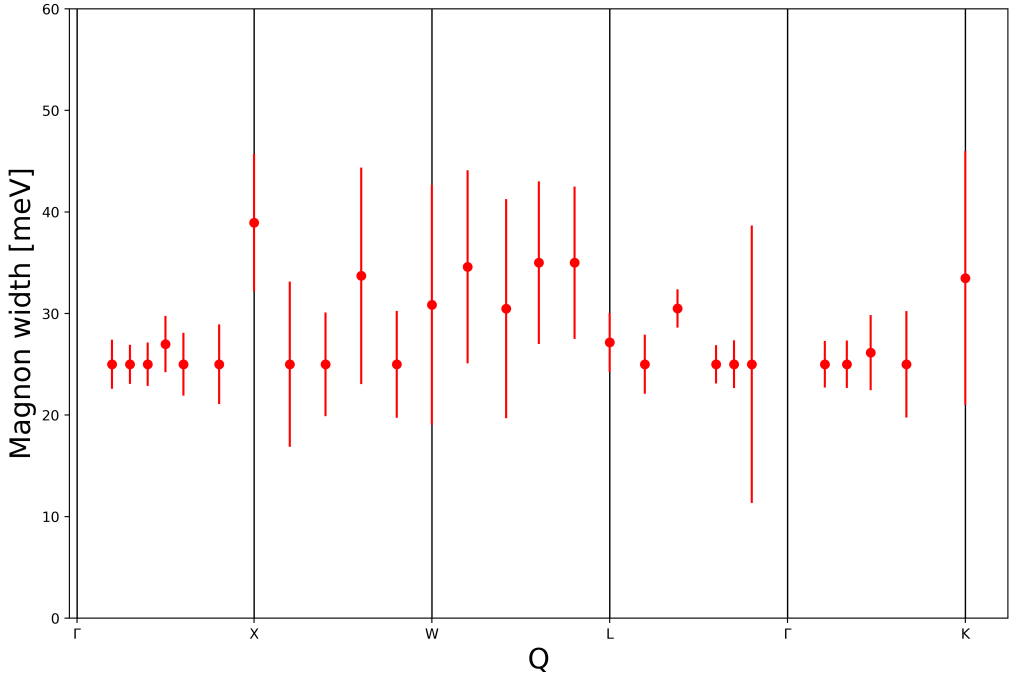

Figure 3.13: *Magnon width (γ in equation 3.5) from the fit of experimental data along the high-symmetry crystallographic directions. The magnon width is bounded in the range above 25 meV to take into account the energy resolution. The error bars are given by the fit.*

bandwidth of $\sim$ 12 meV from the RIXS measurements. A similar band gap but a larger bandwidth has been found for $Sm_2Ir_2O_7$ (gap of $\sim$ 25 meV and bandwidth of $\sim$ 20 meV) and $Eu_2Ir_2O_7$ (gap of $\sim$ 28 meV of and bandwidth of $\sim$ 20 meV) [53, 54].
Equivalent results in terms of energy and width have been obtained by fitting the magnetic excitation with a Lorentzian (symmetric) function.

3.4.3. Numerical simulations of magnetic excitations

We have simulated the dynamics of the system using the SpinW library on Matlab. The code is reported in Appendix B.
We have defined the Hamiltonian:

$$H = \sum_{ij} J\mathbf{S}_i \cdot \mathbf{S}_j + \mathbf{D}_{ij} \cdot (\mathbf{S}_i \times \mathbf{S}_j) \tag{3.6}$$

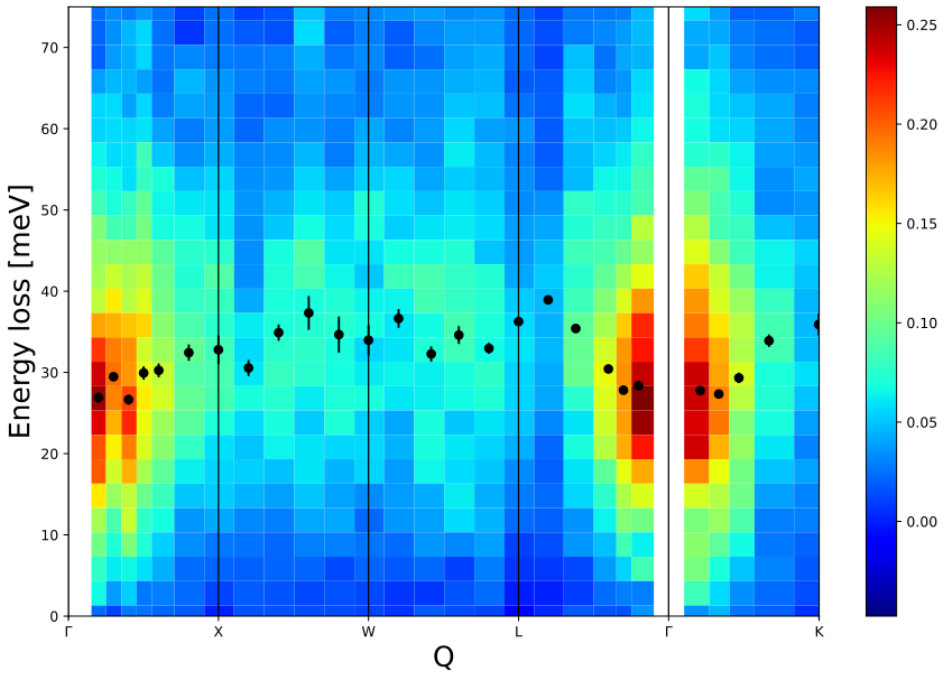

Figure 3.14: *Intensity map of the RIXS spectra for single crystal* $Tb_{2+x}Ir_{2-x}O_{7-y}$ $x \sim 0.4$. *The intensity of the elastic peak and of the C feature have been subtracted. The black dots on top of the intensity map are the magnetic excitations, whose position is extracted from the fit. The error bars are obtained from the fit.*

It is made up of the contributions of the Heisenberg interaction and of the Dzyaloshinskii–Moriya interaction. The same Hamiltonian has been used by Donnerer et al. [54] for $Sm_2Ir_2O_7$.

Fig. 3.15 shows the simulated magnetic structure of the iridium sublattice obtained with SpinW. The blue arrows represent the spins. The red segments between the ions represent the Heisenberg exchange and the red arrows the Dzyaloshinskii–Moriya interaction.

From the fit of the entire experimental map we have estimated the values of J and $D = |\mathbf{D}_{ij}|$. The values found are: $J = 18.09$ meV and $D = 6.6$ meV.

The simulated intensity map obtained with SpinW considering the parameters from the fit is shown in Fig. 3.16.

Fig. 3.17 shows the simulated dispersion relation with the experimental data on top of the experimental intensity map.

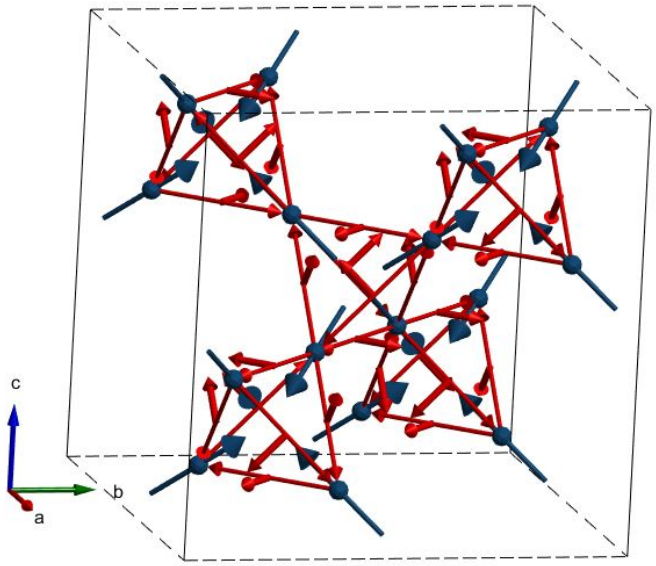

Figure 3.15: *Crystal structure of pyrochlore iridate single crystal simulated by SpinW. Only the iridium sublattice is shown. The blue arrows represent the AIAO magnetic structure at iridium sites. The red segments between the iridium ions represent the Heisenberg exchange. The red arrows represent the Dzyaloshinskii–Moriya interaction.*

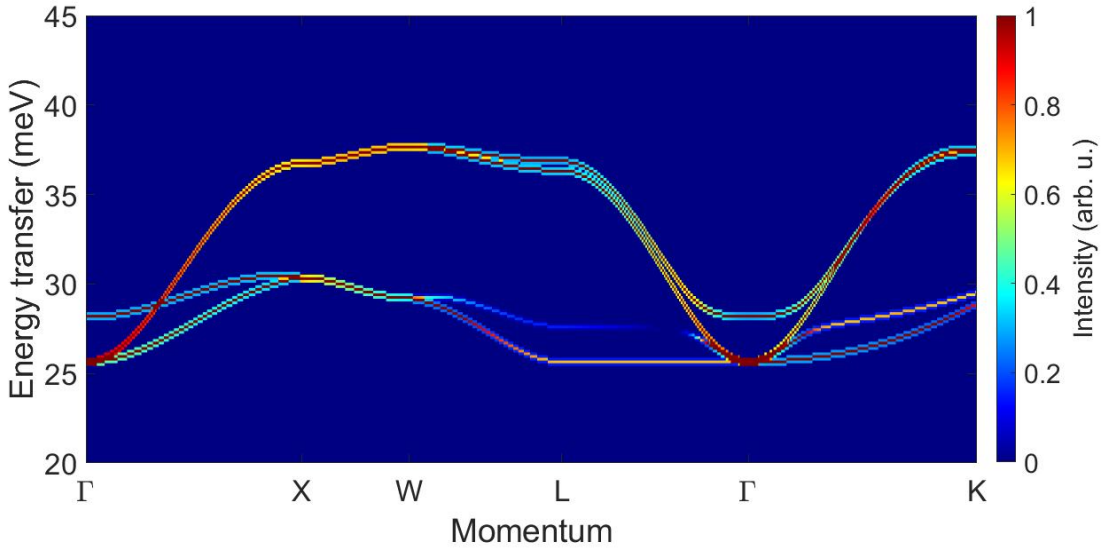

Figure 3.16: *Simulated intensity map for $Tb_2Ir_2O_7$ with $J = 18.09$ meV and $D = 6.6$ meV.*

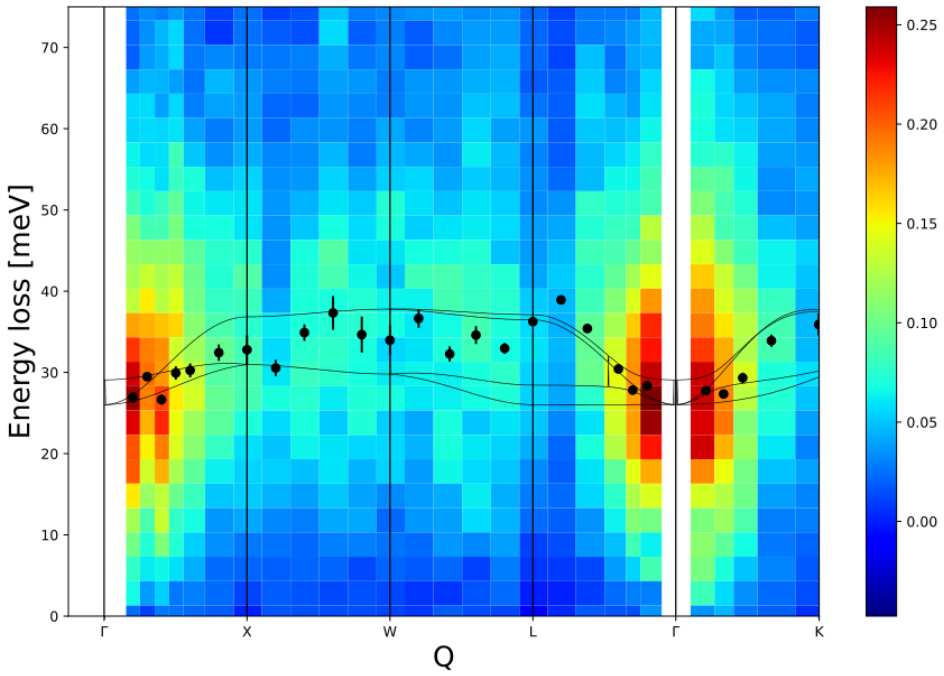

Figure 3.17: *Simulated dispersion relation of magnetic excitation for $Tb_2Ir_2O_7$ with J = 18.09 meV and D = 6.6 meV (continuous curves) and experimental data (black dots) on top of the experimental intensity map.*

3.4.4. Discussion

Important considerations can be deduced from the analysis of the experimental data. From the *dd* excitations we have calculated the values of the SOC constant and of the trigonal crystal field $\lambda = 0.399$ eV and $\Delta = 0.516$ eV. The results are in agreement with values found in literature for other pyrochlore iridates [82]. For $Y_2Ir_2O_7$ the values found are $\lambda = 0.43$ eV and $\Delta = 0.56$ eV and for $Eu_2Ir_2O_7$ $\lambda = 0.46$ eV and $\Delta = 0.46$ eV. The lower value of λ we found is probably due to the abundance of terbium which is characterized by a smaller SOC with respect to iridium.

From Fig. 3.14 one can observe that the magnon intensity clearly decreases when moving away from the Γ point. Moreover, the magnon width has been analyzed. An increase of the latter would be indicative of a damping of the magnetic excitation as it is expected in an itinerant picture due to the interaction with the Stoner continuum. However, the magnon width is resolution-limited throughout almost the whole Brillouin zone (widths smaller than 25 meV cannot be probed) as can be observed from Fig. 3.13. The magnon width seems to be larger in the WL direction with respect to the other directions, but

the error bars are too large to safely affirm it. Indeed, the entanglement with the other features (especially the broad C feature) makes the fitting challenging. Thus, further analysis on the width of magnetic excitations should be addressed.
The values of the magnetic interactions can be compared with what is found in the literature: Pesin et al. [84] predicted a ratio between D and J of $D/J \sim 0.63$ for an ideal $J_{\text{eff}} = 1/2$ state. We find $J = 18.09$ meV and $D = 6.6$ meV resulting in a smaller value of $D/J \sim 0.36$. Donnerer et al. [54] found for $Sm_2Ir_2O_7$ single crystal: $J = 27.3$ meV, $D = 4.9$ meV and $D/J \sim 0.18$.
Other significant information can be extrapolated from the comparison with numerical simulations. Fig. 3.16, which reports the simulated intensity map, shows a larger intensity of the higher modes with respect to the lower. The experimental data shown in Fig. 3.17 follow the higher energy modes along ΓL and ΓK. Also along XW and WL the highest energy modes seem to be probed even though many points fall in between the branches and the error bars are large. Along ΓX, the experimental magnon positions follow instead the lower dispersion branches. Experimental data for $Sm_2Ir_2O_7$ (see Fig. 1.21b) follow the highest modes of the simulated dispersion in the whole Brillouin zone.
These results can be compared to what obtained from RPA calculations. Fig. 1.22 shows that for small correlations the magnetic modes are damped especially along the crystallographic direction WL (see Fig. 1.22 with U = 5). This would be compatible with a large magnon width along this direction that may be suggested by the experimental data. Moreover, the highest energy modes along ΓX disappear and only the low ones can be probed, as the experimental data seem to prove.

4 | Conclusions and perspectives

We have studied a single crystal of $Tb_2Ir_2O_7$. We have characterized it at the Nèel Institute and we have performed RIXS experiments to study its low-energy dynamics on ID20 at the ESRF.

The sample under study shows a finite degree of stuffing and the real stoichiometry is $Tb_{2+x}Ir_{2-x}O_{7-y}$ with x $\sim$ 0.4. The sample is much more metallic than powder samples which retain the ideal composition. Magnetic measurements show a magnetic transition around 50 K, which has been attributed to the arising of the AIAO magnetic structure on the iridium sublattice. An experimental confirmation should be addressed, for example using resonant elastic X-ray scattering.

A trigonal distortion is found from RIXS spectra showing two peaks as intra-t_{2g} *dd* excitations. The trigonal crystal field and the SOC are estimated. The value of the SOC is smaller than what is found in the literature for other pyrochlore iridates: this has been associated to the abundance of terbium which is characterized by a lower SOC than iridium.

The magnetic interactions are quantified through the comparison of the RIXS data with numerical simulations taking into account the Heisenberg exchange and the Dzyaloshinskii-Moriya interaction. The experimental data show discrepancies with the simulations, which are based on a local-spin description. In the ΓX direction the experimental magnon positions do not follow the high energy modes as expected from simulations. Along the other directions the higher energy modes are probed but not as clearly as for $Sm_2Ir_2O_7$.

The low resistivity together with the differences between the experimental data and simulations may suggest that a local description is not suitable to describe the physics of the system. A more itinerant description might be more accurate as also suggested from the comparison with RPA calculations.

This conclusion is compatible with the realization of the Weyl semimetallic phase: the AIAO magnetic structure breaks the time reversal symmetry and the electronic correlations might be weak enough.

A further analysis on the magnon width could give more information about the damping and consequently on the correlations. This requires an improvement in energy resolution

to disentangle the features in the spectra. The research for a better energy resolution is still evolving, for example analyzer crystals of different materials, such as quartz, have been produced successfully for the first time [67]. Also, other spectrometer designs have been proposed and built [85].
Another solution could be the polarization analysis which would remove the non-magnetic contributions in the spectra. While the elastic contribution would be removed, the nature of the C feature is still unclear and the latter could still be present. Additionally, this has still not been realized for hard X-ray RIXS.
In conclusions, the results obtain may suggest the presence of a semimetallic phase and the stuffing could offer a route to realize topological phases by reducing the electronic correlations.

Bibliography

[1] J. Bednorz, M. Takashige, and K. Müller, "Susceptibility measurements support high-Tc superconductivity in the Ba-La-Cu-O system," *EPL (Europhysics Letters)*, vol. 3, no. 3, p. 379, 1987. https://iopscience.iop.org/article/10.1209/0295-5075/3/3/021.

[2] M. Imada, A. Fujimori, and Y. Tokura, "Metal-insulator transitions," *Rev. Mod. Phys.*, vol. 70, pp. 1039–1263, Oct 1998. https://link.aps.org/doi/10.1103/RevModPhys.70.1039.

[3] A. P. Ramirez, "Colossal magnetoresistance," *Journal of Physics: Condensed Matter*, vol. 9, pp. 8171–8199, sep 1997. https://doi.org/10.1088/0953-8984/9/39/005.

[4] S.-W. Cheong and M. Mostovoy, "Multiferroics: a magnetic twist for ferroelectricity," *Nature Materials*, vol. 6, pp. 13–20, Jan. 2007. https://pubmed.ncbi.nlm.nih.gov/17199121/.

[5] H. Wang and J. Wang, "Electron transport in Dirac and Weyl semimetals," *Chinese Physics B*, vol. 27, p. 107402, Oct 2018. http://dx.doi.org/10.1088/1674-1056/27/10/107402.

[6] C. Shekhar, A. K. Nayak, Y. Sun, M. Schmidt, M. Nicklas, I. Leermakers, U. Zeitler, Y. Skourski, J. Wosnitza, Z. Liu, Y. Chen, W. Schnelle, H. Borrmann, Y. Grin, C. Felser, and B. Yan, "Extremely large magnetoresistance and ultrahigh mobility in the topological Weyl semimetal candinote NbP," *Nature Physics*, vol. 11, p. 645–649, Jun 2015. http://dx.doi.org/10.1038/nphys3372.

[7] R. D. Y. Hills, A. Kusmartseva, and F. V. Kusmartsev, "Current-voltage characteristics of Weyl semimetal semiconducting devices, Veselago lenses, and hyperbolic Dirac phase," *Phys. Rev. B*, vol. 95, p. 214103, Jun 2017. https://link.aps.org/doi/10.1103/PhysRevB.95.214103.

[8] J. Vale, "The nature of the metal-insulator transition in 5d transition metal oxides," *Phd Thesis University College London*, 02 2017. https://discovery.ucl.ac.uk/id/eprint/1538695/.

[9] E. Lefraçois, "Synthesis and study of iridium oxide compounds for entagled spin-orbit physics," *Phd Thesis Université Grenoble Alpes*. https://www.ill.eu/fileadmin/user_upload/ILL/1_About_ILL/List_of_PhD_thesis-/These_Lefrancois_E.pdf.

[10] G. Cao, J. Bolivar, S. McCall, J. E. Crow, and R. P. Guertin, "Weak ferromagnetism, metal-to-nonmetal transition, and negative differential resistivity in single-crystal Sr_2IrO_4," *Phys. Rev. B*, vol. 57, pp. R11039–R11042, May 1998. https://link.aps.org/doi/10.1103/PhysRevB.57.R11039.

[11] W. Witczak-Krempa, G. Chen, Y. B. Kim, and L. Balents, "Correlated quantum phenomena in the strong spin-orbit regime," *Annual Review of Condensed Matter Physics*, vol. 5, p. 57–82, Mar 2014. http://dx.doi.org/10.1146/annurev-conmatphys-020911-125138.

[12] P. Narang, C. A. C. Garcia, and C. Felser, "The topology of electronic band structures," *Nature Materials*, vol. 20, pp. 293 – 300, 2020. https://www.nature.com/articles/s41563-020-00820-4.

[13] C. L. Kane and E. J. Mele, "Quantum spin hall effect in graphene," *Physical Review Letters*, vol. 95, Nov 2005. http://dx.doi.org/10.1103/PhysRevLett.95.226801.

[14] L. Fu, C. L. Kane, and E. J. Mele, "Topological insulators in three dimensions," *Physical Review Letters*, vol. 98, Mar 2007. http://dx.doi.org/10.1103/PhysRevLett.98.106803.

[15] M. Z. Hasan and C. L. Kane, "Colloquium: Topological insulators," *Reviews of Modern Physics*, vol. 82, p. 3045–3067, Nov 2010. http://dx.doi.org/10.1103/RevModPhys.82.3045.

[16] X.-L. Qi and S.-C. Zhang, "Topological insulators and superconductors," *Reviews of Modern Physics*, vol. 83, p. 1057–1110, Oct 2011. http://dx.doi.org/10.1103/RevModPhys.83.1057.

[17] B. Yan and C. Felser, "Topological materials: Weyl semimetals," *Annual Review of Condensed Matter Physics*, vol. 8, no. 1, pp. 337–354, 2017. https://doi.org/10.1146/annurev-conmatphys-031016-025458.

[18] B. A. Bernevig, T. L. Hughes, and S.-C. Zhang, "Quantum spin hall effect and topological phase transition in HgTe quantum wells," *Science*, vol. 314, p. 1757–1761, Dec 2006. http://dx.doi.org/10.1126/science.1133734.

[19] M. Konig, S. Wiedmann, C. Brune, A. Roth, H. Buhmann, L. W. Molenkamp, X.-L.

Qi, and S.-C. Zhang, "Quantum spin hall insulator state in HgTe quantum wells," *Science*, vol. 318, p. 766–770, Nov 2007. http://dx.doi.org/10.1126/science.1148047.

[20] H. Zhang, C.-X. Liu, X.-L. Qi, X. Dai, Z. Fang, and S.-C. Zhang, "Topological insulators in Bi_2Se_3, Bi_2Te_3 and Sb_2Te_3 with a single Dirac cone on the surface," *Nature Physics*, vol. 5, pp. 438–442, June 2009. https://www.nature.com/articles/nphys1270.

[21] Y. Xia *et al.*, "Observation of a large-gap topological-insulator class with a single Dirac cone on the surface," *Nature Phys.*, vol. 5, pp. 398–402, 2009. https://www.nature.com/articles/nphys1274.

[22] S.-Y. Xu, I. Belopolski, N. Alidoust, M. Neupane, G. Bian, C. Zhang, R. Sankar, G. Chang, Z. Yuan, C.-C. Lee, and et al., "Discovery of a Weyl fermion semimetal and topological Fermi arcs," *Science*, vol. 349, p. 613–617, Aug 2015. http://dx.doi.org/10.1126/science.aaa9297.

[23] S. Blundell, "Magnetism in condesed matter," *Oxford Master Series in Physics*. https://aapt.scitation.org/doi/abs/10.1119/1.1522704?journalCode=ajp.

[24] D. Pincini, "On the hierarchy of electronic and magnetic energy scales in novel 3d, 4d and 5d transition metal oxides probed by X-ray techniques," *PhD thesis, UCL (University College London)*, 2019. https://discovery.ucl.ac.uk/id/eprint/10063729/.

[25] B. J. Kim, H. Jin, S. J. Moon, J.-Y. Kim, B.-G. Park, C. S. Leem, J. Yu, T. W. Noh, C. Kim, S.-J. Oh, J.-H. Park, V. Durairaj, G. Cao, and E. Rotenberg, "Novel J_{eff}=1/2 Mott state induced by relativistic spin-orbit coupling in Sr_2IrO_4," *Phys. Rev. Lett.*, vol. 101, p. 076402, Aug 2008. https://link.aps.org/doi/10.1103/PhysRevLett.101.076402.

[26] G. Jackeli and G. Khaliullin, "Mott insulators in the strong spin-orbit coupling limit: from Heisenberg to a Quantum Compass and Kitaev Models," *Physical Review Letters*, vol. 102, Jan 2009. http://dx.doi.org/10.1103/PhysRevLett.102.017205.

[27] H. Takagi, T. Takayama, G. Jackeli, G. Khaliullin, and S. E. Nagler, "Concept and realization of Kitaev quantum spin liquids," *Nature Reviews Physics*, vol. 1, pp. 264–280, Mar. 2019. https://www.nature.com/articles/s42254-019-0038-2.

[28] S. K. Choi, R. Coldea, A. N. Kolmogorov, T. Lancaster, I. I. Mazin, S. J. Blundell, P. G. Radaelli, Y. Singh, P. Gegenwart, K. R. Choi, S.-W. Cheong, P. J. Baker, C. Stock, and J. Taylor, "Spin waves and revised crystal structure of

honeycomb iridate Na_2IrO_3," *Phys. Rev. Lett.*, vol. 108, p. 127204, Mar 2012. https://link.aps.org/doi/10.1103/PhysRevLett.108.127204.

[29] Y. Singh, S. Manni, J. Reuther, T. Berlijn, R. Thomale, W. Ku, S. Trebst, and P. Gegenwart, "Relevance of the Heisenberg-Kitaev model for the honeycomb lattice iridates A_2IrO_3," *Phys. Rev. Lett.*, vol. 108, p. 127203, Mar 2012. https://link.aps.org/doi/10.1103/PhysRevLett.108.127203.

[30] A. Banerjee, P. Lampen-Kelley, J. Knolle, C. Balz, A. A. Aczel, B. Winn, Y. Liu, D. Pajerowski, J. Yan, C. A. Bridges, and et al., "Excitations in the field-induced quantum spin liquid state of α-$RuCl_3$," *npj Quantum Materials*, vol. 3, Feb 2018. http://dx.doi.org/10.1038/s41535-018-0079-2.

[31] T. Moriya, "Anisotropic superexchange interaction and weak ferromagnetism," *Phys. Rev.*, vol. 120, pp. 91–98, Oct 1960. https://link.aps.org/doi/10.1103/PhysRev.120.91.

[32] M. Elhajal, B. Canals, R. Sunyer, and C. Lacroix, "Ordering in the pyrochlore antiferromagnet due to Dzyaloshinsky-Moriya interactions," *Phys. Rev. B*, vol. 71, p. 094420, Mar 2005. https://link.aps.org/doi/10.1103/PhysRevB.71.094420.

[33] M. J. Harris, S. T. Bramwell, D. F. McMorrow, T. Zeiske, and K. W. Godfrey, "Geometrical frustration in the ferromagnetic pyrochlore $Ho_2Ti_2O_7$," *Phys. Rev. Lett.*, vol. 79, pp. 2554–2557, Sep 1997. https://link.aps.org/doi/10.1103/PhysRevLett.79.2554.

[34] M. J. Harris, S. T. Bramwell, P. C. W. Holdsworth, and J. D. M. Champion, "Liquid-gas critical behavior in a frustrated pyrochlore ferromagnet," *Phys. Rev. Lett.*, vol. 81, pp. 4496–4499, Nov 1998. https://link.aps.org/doi/10.1103/PhysRevLett.81.4496.

[35] S. T. Bramwell and M. J. P. Gingras, "Spin ice state in frustrated magnetic pyrochlore materials," *Science*, vol. 294, no. 5546, pp. 1495–1501, 2001. https://www.science.org/doi/abs/10.1126/science.1064761.

[36] B. C. den Hertog and M. J. P. Gingras, "Dipolar interactions and origin of spin ice in ising pyrochlore magnets," *Physical Review Letters*, vol. 84, p. 3430–3433, Apr 2000. http://dx.doi.org/10.1103/PhysRevLett.84.3430.

[37] K. Matsuhira, M. Wakeshima, Y. Hinatsu, and S. Takagi, "Metal–insulator transitions in pyrochlore oxides $Ln_2Ir_2O_7$," *Journal of The Physical Society of Japan - J PHYS SOC JPN*, vol. 80, 09 2011. https://journals.jps.jp/doi/10.1143/JPSJ.80.094701.

[38] J. Greedan, M. Sato, X. Yan, and F. Razavi, "Spin-glass-like behavior in $Y_2Mo_2O_7$, a concentrated, crystalline system with negligible apparent disorder," *Solid State Communications*, vol. 59, no. 12, pp. 895–897, 1986. https://www.sciencedirect.com/science/article/pii/0038109886906526.

[39] J. S. Gardner, S. R. Dunsiger, B. D. Gaulin, M. J. P. Gingras, J. E. Greedan, R. F. Kiefl, M. D. Lumsden, W. A. MacFarlane, N. P. Raju, J. E. Sonier, I. Swainson, and Z. Tun, "Cooperative paramagnetism in the geometrically frustrated pyrochlore antiferromagnet $Tb_2Ti_2O_7$," *Phys. Rev. Lett.*, vol. 82, pp. 1012–1015, Feb 1999. https://link.aps.org/doi/10.1103/PhysRevLett.82.1012.

[40] A. V. X. Wan, A. Turner and S. Savrasov, "Topological semimetal and Fermi-arc surface states in the electronic structure of pyrochlore iridates," *Physical Review B*, vol. 99, pp. 403–422, 2011. https://doi.org/10.1103/PhysRevB.83.205101.

[41] H. Shinaoka, S. Hoshino, M. Troyer, and P. Werner, "Phase diagram of pyrochlore iridates: all-in–all-out magnetic ordering and non-Fermi-liquid properties," *Phys. Rev. Lett.*, vol. 115, p. 156401, Oct 2015. https://link.aps.org/doi/10.1103/PhysRevLett.115.156401.

[42] W. Witczak-Krempa and Y. B. Kim, "Topological and magnetic phases of interacting electrons in the pyrochlore iridates," *Phys. Rev. B*, vol. 85, p. 045124, Jan 2012. https://link.aps.org/doi/10.1103/PhysRevB.85.045124.

[43] H. Sagayama, D. Uematsu, T. Arima, K. Sugimoto, J. J. Ishikawa, E. O'Farrell, and S. Nakatsuji, "Determination of long-range all-in-all-out ordering of Ir^{4+} moments in a pyrochlore iridate $Eu_2Ir_2O_7$ by resonant X-ray diffraction," *Phys. Rev. B*, vol. 87, p. 100403, Mar 2013. https://link.aps.org/doi/10.1103/PhysRevB.87.100403.

[44] J. P. Clancy, H. Gretarsson, E. K. H. Lee, D. Tian, J. Kim, M. H. Upton, D. Casa, T. Gog, Z. Islam, B.-G. Jeon, K. H. Kim, S. Desgreniers, Y. B. Kim, S. J. Julian, and Y.-J. Kim, "X-ray scattering study of pyrochlore iridates: crystal structure, electronic, and magnetic excitations," *Phys. Rev. B*, vol. 94, p. 024408, Jul 2016. https://link.aps.org/doi/10.1103/PhysRevB.94.024408.

[45] S. Zhao, J. M. Mackie, D. E. MacLaughlin, O. O. Bernal, J. J. Ishikawa, Y. Ohta, and S. Nakatsuji, "Magnetic transition, long-range order, and moment fluctuations in the pyrochlore iridate $Eu_2Ir_2O_7$," *Phys. Rev. B*, vol. 83, p. 180402, May 2011. https://link.aps.org/doi/10.1103/PhysRevB.83.180402.

[46] S. M. Disseler, "Direct evidence for the all-in/all-out magnetic structure in the pyrochlore iridates from muon spin relax-

ation," *Physical Review B*, vol. 89, no. 14, p. 140413, 2014. https://journals.aps.org/prb/abstract/10.1103/PhysRevB.89.140413.

[47] K. Tomiyasu, K. Matsuhira, K. Iwasa, M. Watahiki, S. Takagi, M. Wakeshima, Y. Hinatsu, M. Yokoyama, K. Ohoyama, and K. Yamada, "Emergence of magnetic long-range order in frustrated pyrochlore $Nd_2Ir_2O_7$ with metal–insulator transition," *Journal of the Physical Society of Japan*, vol. 81, p. 034709, Mar 2012. http://dx.doi.org/10.1143/JPSJ.81.034709.

[48] E. Lefrançois, V. Simonet, R. Ballou, E. Lhotel, A. Hadj-Azzem, S. Kodjikian, P. Lejay, P. Manuel, D. Khalyavin, and L. C. Chapon, "Anisotropy-tuned magnetic order in pyrochlore iridates," *Phys. Rev. Lett.*, vol. 114, p. 247202, Jun 2015. https://link.aps.org/doi/10.1103/PhysRevLett.114.247202.

[49] H. Guo, C. Ritter, and A. C. Komarek, "Direct determination of the spin structure of $Nd_2Ir_2O_7$ by means of neutron diffraction," *Phys. Rev. B*, vol. 94, p. 161102, Oct 2016. https://link.aps.org/doi/10.1103/PhysRevB.94.161102.

[50] E. Lefrançois, L. Mangin-Thro, E. Lhotel, J. Robert, S. Petit, V. Cathelin, H. E. Fischer, C. V. Colin, F. Damay, J. Ollivier, P. Lejay, L. C. Chapon, V. Simonet, and R. Ballou, "Spin decoupling under a staggered field in the $Gd_2Ir_2O_7$ pyrochlore," *Phys. Rev. B*, vol. 99, p. 060401, Feb 2019. https://link.aps.org/doi/10.1103/PhysRevB.99.060401.

[51] H. Jacobsen, C. D. Dashwood, E. Lhotel, D. Khalyavin, P. Manuel, R. Stewart, D. Prabhakaran, D. F. McMorrow, and A. T. Boothroyd, "Strong quantum fluctuations from competition between magnetic phases in a pyrochlore iridate," *Phys. Rev. B*, vol. 101, p. 104404, Mar 2020. https://link.aps.org/doi/10.1103/PhysRevB.101.104404.

[52] K. Vlášková, R. Colman, and M. Klicpera, "Synthesis of $Er_2Ir_2O_7$ pyrochlore iridate by solid-state-reaction and CsCl flux method," *Materials Chemistry and Physics*, vol. 258, p. 123868, 2021. https://www.sciencedirect.com/science/article/pii/S025405842031227X.

[53] S. H. Chun, B. Yuan, D. Casa, J. Kim, C.-Y. Kim, Z. Tian, Y. Qiu, S. Nakatsuji, and Y.-J. Kim, "Magnetic excitations across the metal-insulator transition in the pyrochlore iridate $Eu_2Ir_2O_7$," *Phys. Rev. Lett.*, vol. 120, p. 177203, Apr 2018. https://link.aps.org/doi/10.1103/PhysRevLett.120.177203.

[54] C. Donnerer, M. Rahn, M. M. Sala, J. Vale, D. Pincini, J. Strempfer, M. Krisch, D. Prabhakaran, A. Boothroyd, and D. McMorrow, "All-in–all-out magnetic order

and propagating spin waves in $Sm_2Ir_2O_7$," *Physical Review Letters*, vol. 117, Jul 2016. http://dx.doi.org/10.1103/PhysRevLett.117.037201.

[55] E. K.-H. Lee, S. Bhattacharjee, and Y. B. Kim, "Magnetic excitation spectra in pyrochlore iridates," *Physical Review B*, vol. 87, Jun 2013. http://dx.doi.org/10.1103/PhysRevB.87.214416.

[56] R. W. Schoenlein, S. Boutet, M. P. Minitti, and A. Dunne, "The linac coherent light source: recent developments and future plans," *Applied Sciences*, vol. 7, no. 8, 2017. https://www.mdpi.com/2076-3417/7/8/850.

[57] J. Als-Nielsen and D. McMorrow, *Elements of modern X-ray physics*. John Wiley & Sons, 2011. https://books.google.fr/books/about/Elements_of_Modern_X_ray_Physics.html-?id=rlqlboWlTRMCredir_esc=y.

[58] F. R. Elder, A. M. Gurewitsch, R. V. Langmuir, and H. C. Pollock, "Radiation from electrons in a synchrotron," *Phys. Rev.*, vol. 71, pp. 829–830, Jun 1947. https://link.aps.org/doi/10.1103/PhysRev.71.829.5.

[59] European Synchrtron Radiation Facility (ESRF), "What is a synchrotron." https://www.esrf.fr/about/synchrotron-science/synchrotron.

[60] P. Raimondi, "Hybrid Multi Bend Achromat: from SuperB to EBS," in *8th International Particle Accelerator Conference*, (Copenhagen, Denmark), pp. 3670–3675, May 2017. https://hal.archives-ouvertes.fr/hal-01584616.

[61] P. Yang, Z. Bai, T. Zhang, D. Xu, and L. Wang, "Design of a hybrid ten-bend-achromat lattice for a diffraction-limited storage ring light source," *Nuclear Instruments and Methods in Physics Research Section A: Accelerators, Spectrometers, Detectors and Associated Equipment*, vol. 943, p. 162506, 2019. https://www.sciencedirect.com/science/article/pii/S0168900219310459.

[62] R. O. Hettel, "DLSR design and plans: an international overview.," *Journal of synchrotron radiation*, vol. 21 Pt 5, pp. 843–55, 2014. https://pubmed.ncbi.nlm.nih.gov/25177976/.

[63] L. J. Ament, M. Van Veenendaal, T. P. Devereaux, J. P. Hill, and J. Van Den Brink, "Resonant inelastic X-ray scattering studies of elementary excitations," *Reviews of Modern Physics*, vol. 83, no. 2, p. 705, 2011. https://doi.org/10.1103/RevModPhys.83.705.

[64] M. Blume, "Magnetic scattering of X-rays," *Journal of Applied Physics*, vol. 57, no. 8, pp. 3615–3618, 1985. https://aip.scitation.org/doi/10.1063/1.335023.

[65] M. Moretti Sala, C. Henriquet, L. Simonelli, R. Verbeni, and G. Monaco, "High energy-resolution set-up for Ir L3 edge RIXS experiments," *Journal of Electron Spectroscopy and Related Phenomena*. https://doi.org/10.1016/j.elspec.2012.08.002.

[66] M. Moretti Sala, K. Martel, C. Henriquet, A. Al Zein, L. Simonelli, C. J. Sahle, H. Gonzalez, M.-C. Lagier, C. Ponchut, S. Huotari, R. Verbeni, M. Krisch, and G. Monaco, "A high-energy-resolution resonant inelastic X-ray scattering spectrometer at ID20 of the European Synchrotron Radiation Facility," *Journal of Synchrotron Radiation*, vol. 25, pp. 580–591, Mar 2018. https://doi.org/10.1107/S1600577518001200.

[67] J. Kim, D. Casa, A. Said, R. Krakora, B. J. Kim, E. Kasman, X. Huang, and T. Gog, "Quartz-based flat-crystal resonant inelastic X-ray scattering spectrometer with sub-10 mev energy resolution," 2017. https://www.nature.com/articles/s41598-018-20396-z.

[68] W. R. Busing and H. A. Levy, "Angle calculations for 3- and 4-circle X-ray and neutron diffractometers," *Acta Crystallographica*, vol. 22, pp. 457–464, Apr 1967. https://doi.org/10.1107/S0365110X67000970.

[69] P. van der Linden, H. Vitoux, R. Steinmann, B. Vallone, and C. Ardiccioni, "An open flow helium cryostat for synchrotron X-ray diffraction experiments," *Journal of Physics: Conference Series*, vol. 425, p. 012015, mar 2013. https://doi.org/10.1088/1742-6596/425/1/012015.

[70] S. Huotari, F. Albergamo, G. Vankó, R. Verbeni, and G. Monaco, "Resonant inelastic hard X-ray scattering with diced analyzer crystals and position-sensitive detectors," *Review of Scientific Instruments*, vol. 77, p. 053102, 2006. https://aip.scitation.org/doi/10.1063/1.2198805.

[71] Wikipedia contributors, "EDX-scheme." https://commons.wikimedia.org/wiki/File:EDX-scheme.svg.

[72] T. G. Santos, "Characterization of FSP by electrical conductivity," in *Surface Modification by Solid State Processing*, pp. 153–176, Elsevier, 2014. https://www.sciencedirect.com/science/article/pii/B9780857094681500050?via

[73] K. Gramm, L. Lundgren, and O. Beckman, "Squid magnetometer for mange-

tization measurements," *Physica Scripta*, vol. 13, no. 2, p. 93, 1976. https://iopscience.iop.org/article/10.1088/0031-8949/13/2/004.

[74] R. L. Fagaly, "Superconducting quantum interference device instruments and applications," *Review of Scientific Instruments*, vol. 77, pp. 101101–101101–45, Oct. 2006.

[75] P. Marcon and K. Ostanina, "Overview of methods for magnetic susceptibility measurement," in *PIERS Proceedings*, 2012. https://www.agoenvironmental.com/sites/default/files/pdf/1P8_0420.pdf.

[76] Simon Ward, "SpinW." https://spinw.org/.

[77] J. N. Millican, R. T. Macaluso, S. Nakatsuji, Y. Machida, Y. Maeno, and J. Y. Chan, "Crystal growth and structure of $R_2Ir_2O_7$ (R = Pr, Eu) using molten KF," *Materials Research Bulletin*, vol. 42, no. 5, pp. 928–934, 2007. https://www.osti.gov/biblio/21000638-crystal-growth-structure-sub-ir-sub-sub-pr-eu-using-molten-kf.

[78] C. Donnerer, M. C. Rahn, E. Schierle, R. S. Perry, L. S. I. Veiga, G. Nisbet, S. P. Collins, D. Prabhakaran, A. T. Boothroyd, and D. F. McMorrow, "Selective probing of magnetic order on Tb and Ir sites in stuffed $Tb_2Ir_2O_7$ using resonant X-ray scattering," *Journal of Physics: Condensed Matter*, vol. 31, p. 344001, jun 2019. https://doi.org/10.1088/1361-648x/ab2217.

[79] H. Kumar and A. K. Pramanik, "Nonmagnetic substitution in pyrochlore iridate $Y_2(Ir_{1-x}Ti_x)_2O_7$: structure, magnetism, and electronic properties," *The Journal of Physical Chemistry C*, vol. 123, no. 20, pp. 13036–13046, 2019. https://doi.org/10.1021/acs.jpcc.9b02011.

[80] H. Kumar, R. S. Dhaka, and A. K. Pramanik, "Evolution of structure, magnetism, and electronic transport in the doped pyrochlore iridate $Y_2Ir_{2-x}Ru_xO_7$," *Phys. Rev. B*, vol. 95, p. 054415, Feb 2017. https://link.aps.org/doi/10.1103/PhysRevB.95.054415.

[81] C. Donnerer, "X-ray studies of magnetic and structural transitions in iridates," 2018. https://discovery.ucl.ac.uk/id/eprint/10047266/.

[82] L. Hozoi, H. Gretarsson, J. Clancy, B.-G. Jeon, B. Lee, K. Kim, V. Yushankhai, P. Fulde, D. Casa, T. Gog, *et al.*, "Longer-range lattice anisotropy strongly competing with spin-orbit interactions in pyrochlore iridates," *Physical Review B*.

[83] X. Liu, V. M. Katukuri, L. Hozoi, W.-G. Yin, M. P. M. Dean, M. H. Upton, J. Kim, D. Casa, A. Said, T. Gog, T. F. Qi, G. Cao, A. M. Tsvelik, J. van den Brink, and J. P.

Hill, "Testing the validity of the strong spin-orbit-coupling limit for octahedrally coordinated iridate compounds in a model system Sr_3CuIrO_6," *Phys. Rev. Lett.*, vol. 109, p. 157401, Oct 2012. https://link.aps.org/doi/10.1103/PhysRevLett.109.157401.

[84] D. Pesin and L. Balents, "Mott physics and band topology in materials with strong spin–orbit interaction," *Nature Physics*, vol. 6, p. 376–381, Mar 2010. http://dx.doi.org/10.1038/nphys1606.

[85] J. Bertinshaw, S. Mayer, F.-U. Dill, H. Suzuki, O. Leupold, A. Jafari, I. Sergueev, M. Spiwek, A. Said, E. Kasman, X. Huang, B. Keimer, and H. Gretarsson, "IRIXS Spectrograph: an ultra high-resolution spectrometer for tender RIXS," *Journal of Synchrotron Radiation*, vol. 28, pp. 1184–1192, Jul 2021. https://doi.org/10.1107/S1600577521003805.

A | Fitting the spectra

Fig.A.1 shows the fits of the RIXS spectra at T = 10 K.

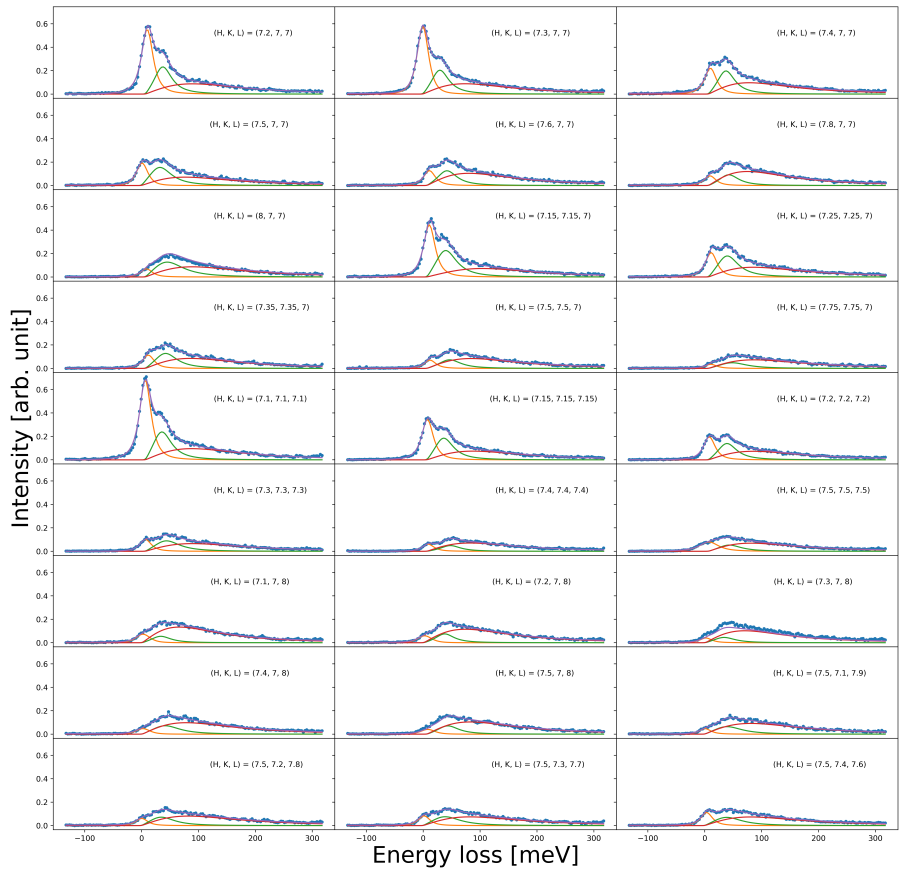

Figure A.1: *RIXS spectra at 10 K for different momentum trasfer and their fitting curves. The orange peak is a Pearson VII function representing the elastic feature, the green peak is a damped harmonic oscillator function representing the magnon and the red one is a damped harmonic oscillator function and it fits the C feature.*

The fits have been performed in Python Scipy with the function scipy.optimize.curvefit(). The latter uses a least-squares method to find the best parameter to fit the data.

B | SpinW details

```
%Import the Cif file for the crystal: it contains all the information about
%the crystal structure
crystal = spinw('D:/Documents/5_anno/tesi/SWMatlabsScripts/Tb2Ir2O7_struct.cif');
%Plot the crystal structure
hFig = plot(crystal);
%Define the unit cell, considering just the iridium site
crystal.unit_cell = crystal.unitcell(2);
hFig = plot(crystal,'atomLabel',true);

%Initialization of the parameters J and D
J1 = 18;
D = 4;

%Definition of the couplings
crystal.gencoupling('maxDistance', 4); %Defines the maximum distance at which the↙
interaction must be considered
crystal.table('bond', 1);
crystal.addmatrix('label','J1','value',J1, 'color','green');  %Definition of the↙
Heisenber interaction
crystal.addcoupling('mat','J1','bond',1); %Heisenber interaction just between nearest↙
neighbours
crystal.addmatrix('label','DM1','value',D,'color','red') %Definition of the↙
Dzyaloshinskii Moriya interaction
crystal.addcoupling('mat','DM1','bond',1) %The Dzyaloshinskii Moriya interaction just↙
between nearest neighbours
crystal.setmatrix('mat','DM1','pref',{[D D D]});
plot(crystal);
crystal.table('mat')

%Definition of the magnetic structure: this gives the AIAO magnetic
%structure
S = [1 -1 -1  1  1  1 -1 -1  1 -1  1 -1 -1  1 -1  1;...
     1 -1  1 -1  1 -1 -1  1  1  1 -1 -1 -1 -1  1  1;...
     1  1 -1 -1  1 -1  1 -1  1 -1 -1  1  1 -1 -1  1];
 crystal.genmagstr('mode','direct','k',[0 0 0],'S', S);

%Plot the magnetic structure
plot(crystal,'magCentered',true)

%Uploading of the experimental data that has to be fitted to extract the
%magnitude of the interactions
T = sw_readtable('data_correction.txt');
w1 = [T(:).EN1];

%Definition of Q
Q = [[T(:).QH];[T(:).QK];[T(:).QL]]';
%Definition of the points in the Brillouin zone
X  = [0 0 1];
G  = [0 0 0];
W = [0.5 0 1];
L  = [1/2 1/2 1/2];
K = [3/4 3/4 0];
Qlist = {[7.00001 7.000001 7.000001] [7.000001 7.00001 8.0001] [7.50000 7.000001↙
8.000001]...
    [7.500001 7.500001 7.500001] [7.000001 7.000001 7.000001] [7.7501 7.7501 7.000001]↙
```

```
300};
Qlab  = {'\Gamma' 'X' 'W' 'L' '\Gamma' 'K'};

%Calculation of the spin wave dispersion relation
%The spinwave function calculates the spin wave dispersion and spin-spin
%correlation function at the reciprocal space points given
spec = crystal.spinwave(Qlist);
%The sw_grid function converts spec into an intensity map
spec = sw_egrid(spec,'component','Sxx+Syy+Szz','Evect',linspace(0,150,1001));
%The function omegasum removes the degenerate modes from the dispersion
spec = sw_omegasum(spec,'zeroint',1e-5,'tol',1e-3);
%The function instrument convolutes spectrum with resolution function (dE is the FWHM↙
of a Gaussian)
spec = sw_instrument(spec,'dE',0.2);

%The dispersion is plotted: plotspec can plot dispersion or intensities as
%line plots or intensity map (it is defined by the different modes)
figure
sw_plotspec(spec,'qlabel',Qlab,'mode','disp','colormap',[0,0,0])
ylim([20 60])
legend('off')
title('')
figure
sw_plotspec(spec,'qlabel',Qlab,'mode',2,'colormap',[0,0,0])

figure
sw_plotspec(spec,'qlabel',Qlab,'mode','color','axLim',[0, 1.5])
sw_plotspec(spec,'qlabel',Qlab,'mode',3)
legend('off')
colormap(jet)
title('')
ylim([20 45])
caxis([0 1])

%Fitting
%The spinw.fitspec function fit experimental data in 'data_corrected.txt'
pref = swpref;
pref.tid = 0;
par_fit = struct;
par_fit.datapath = 'data_correction.txt';
par_fit.Evect    = linspace(20,70,71);
%The matparser function is used to parametrize the Hamiltonian: the
%parameters are the Heisenber exchange and the components of the
%Dzyaloshinskii Moriya vector D
par_fit.func     = @(obj,p)matparser(obj,'param',p,...
                    'mat',{'J1' 'DM1(2,1)' 'DM1(3,1)' 'DM1(1,2)' 'DM1(1,3)' 'DM1(2,3)'↙
'DM1(3,2)'},'init',true);

%Minimum values of the parameters of the Hamiltonian
par_fit.xmin      = [16 -8 -8 -8 -8 -8 -8];
%Maximum values of the parameters of the Hamiltonian
par_fit.xmax      = [20 8 8 8 8 8 8];
%Guess values of the parameters
par_fit.x0        = [18 -4 4 4 -4 4 -4];
par_fit.plot      = true;
```

```
par_fit.hermit    = false;
par_fit.optimizer = 'pso'; %(particle swarm optimization)
par_fit.MaxIter   = 20;
par_fit.optmem    = 1;
par_fit.nrun      = 5;

fitStr = crystal.fitspec(par_fit);

%After fitting, the best result is stored in the spinw object.

%Exporting of the results
Q = spec.hkl; %It contains the input Q values
Disp = spec.omega; %Calculated spin wave dispersion
H = Q(1,:);
K = Q(2,:);
L = Q(3,:);
m1 = Disp(1,:);
m2 = Disp(2,:);
m3 = Disp(3,:);
m4 = Disp(4,:);
I = spec.swInt; %Intensity
I1 = I(1,:);
I2 = I(2,:);
I3 = I(3,:);
I4 = I(4,:);

T = table(H', K', L', m1', m2', m3', m4',I1',I2',I3',I4'); %Write the table to export
writetable(T, 'tabledata6.txt');
```

Figure B.1: *Matlab code using SpinW library*

Fig.B.1 shows the Matlab code using the SpinW library.
The crystal structure from the *cif* file is defined and plotted. Just the iridium crystal structure is taken into account since in our experiments we are resonant to an iridium edge.
The Hamiltonian is defined introducing the interactions. The Heisenberg and Dzyaloshinskii–Moriya interactions between nearest neighbours are considered.
The magnetic structure is then defined by the definition of a spin vector assigning the components of the spin to the sixteen iridium ions in the cubic cell. The spin vector for the AIAO structure has been found in literature. The structure is shown in Fig.3.15.
Subsequently, the spin wave dispersion is calculated and plotted. The intensity map is shown in Fig.3.16.
The fit of the experimental data is performed with J and the components of the anisotropic tensor $J^{\mathrm{A}}{}_{\mathrm{ij}}$ as parameters. The latter is related to the Dzyaloshinskii Moriya vector $\mathbf{D}$. The Dzyaloshinskii Moriya interaction between two spins (labelled by i and j) can be written as:

$$H^{\mathrm{DMI}}{}_{ij} = \mathbf{S}_i{}^T \cdot J_{ij}^A \cdot \mathbf{S}_j = \mathbf{D} \cdot (\mathbf{S}_i \times \mathbf{S}_j) \tag{B.1}$$

The relation between the tensor ${J^{\mathrm{A}}}_{\mathrm{ij}}$ and the Dzyaloshinskii Moriya vector is:

$$ {J^{\mathrm{A}}}_{\mathrm{ij}} = \begin{pmatrix} 0 & D_{\mathrm{z}} & -D_{\mathrm{y}} \\ -D_{\mathrm{z}} & 0 & D_{\mathrm{x}} \\ D_{\mathrm{y}} & -D_{\mathrm{x}} & 0 \end{pmatrix} \tag{B.2} $$

An approximation is considered: the average of the components of the anisotropic tensor found from the fit is performed and the vector $\mathbf{D}$ is considered with all equal components. Finally, the four non-degenerate modes of the dispersion of spin waves with the fitted parameters is exported in a *txt* file.

List of Figures

Acknowledgements

Thanks to Politecnico di Milano for having given me the opportunity to carry out my master thesis to the ESRF, in particular I would like to thank Prof. Marco Moretti and Prof. Giacomo Ghiringhelli for the chance of getting in contact with this amazing reality. I would like to thank Christoph Sahle for always making me feel part of the team (also by trying to teach me how to ski) and being supportive. I would like to thank Quentin Faure for the incredible amounts of things he taught me during these months at ESRF. I am enormously grateful to him for being a patient teacher and a kind friend. Alessandro Longo has been the best office mate, I would like to thank him for all the coffee breaks we took and the philosophic discussions. Thanks to Emmanuelle De Clermont Gallerande for being a friend at ESRF since the first day and to Florent Gerbon for the efforts of trying to teach me french. I also would like to thank Blanka Detlefs for the technical supports during the experiments, Dr. Dharmalingam Prabhakaran for providing the samples, Dr. Jian-Rui SOH for performing resistivity measurements and Dr. Virginie Simonet and Dr. Elsa Lhotel for the help with SQUID measurements.

It wouldn't have been the same experience without my companions of adventures Ilaria, Camilla, Federico, Federico and Matteo: thank you for making these months in Grenoble incredible. Special thanks to Ilaria for all the time spent together, all the climbing sessions, the movies, the dinners, the talks and walks, but also for taking care of me when I took Covid.

I am extremely thankful to all my friends, the ones I know since years, the ones met at university, the ones who are close and those who live far. In particular, I would like to thank Giorgia, Gaia and Martina. Thank you for always being present, for the years of friendship, for the lightness in the soul you are able to give me. Thanks to Chiara, my second sister. I know that wherever we are going to be in the world I will always have you on my side. Thanks to Mery for making these university years light, for the ability of true listening without judging. Thanks to Audrey, Tiphaine, Davide and Isi for being my family abroad, I will always bring with me all the things I learned from you.

My biggest thanks are for my family. I don't have enough space and words to express all my gratitude and love. Thanks dad for teaching me how to look at the world with

curiosity, for always being my first supporter and for the hours you spent listening to me. Thanks mum for always trusting and believing in me, for all the small things we have in common and for always being sincere. Thanks for the free love you give. Thanks Marta for being my hero since day one. I know there's no person in the world I could count more on and no person in the world I am more similar to.
Last but not least, I would like to thank Stefano for all the love, support, for caring, listening and understanding me. You are my safe harbor and the best person I can imagine having on my side for the adventure that the future is.